



Development and Demonstration of a Computational Tool for the Analysis of Particle Vitiating Effects in Hypersonic Propulsion Test Facilities

Hugh Douglas Perkins
Glenn Research Center, Cleveland, Ohio

NASA STI Program . . . in Profile

Since its founding, NASA has been dedicated to the advancement of aeronautics and space science. The NASA Scientific and Technical Information (STI) program plays a key part in helping NASA maintain this important role.

The NASA STI Program operates under the auspices of the Agency Chief Information Officer. It collects, organizes, provides for archiving, and disseminates NASA's STI. The NASA STI program provides access to the NASA Aeronautics and Space Database and its public interface, the NASA Technical Reports Server, thus providing one of the largest collections of aeronautical and space science STI in the world. Results are published in both non-NASA channels and by NASA in the NASA STI Report Series, which includes the following report types:

- **TECHNICAL PUBLICATION.** Reports of completed research or a major significant phase of research that present the results of NASA programs and include extensive data or theoretical analysis. Includes compilations of significant scientific and technical data and information deemed to be of continuing reference value. NASA counterpart of peer-reviewed formal professional papers but has less stringent limitations on manuscript length and extent of graphic presentations.
- **TECHNICAL MEMORANDUM.** Scientific and technical findings that are preliminary or of specialized interest, e.g., quick release reports, working papers, and bibliographies that contain minimal annotation. Does not contain extensive analysis.
- **CONTRACTOR REPORT.** Scientific and technical findings by NASA-sponsored contractors and grantees.
- **CONFERENCE PUBLICATION.** Collected papers from scientific and technical conferences, symposia, seminars, or other meetings sponsored or cosponsored by NASA.
- **SPECIAL PUBLICATION.** Scientific, technical, or historical information from NASA programs, projects, and missions, often concerned with subjects having substantial public interest.
- **TECHNICAL TRANSLATION.** English-language translations of foreign scientific and technical material pertinent to NASA's mission.

Specialized services also include creating custom thesauri, building customized databases, organizing and publishing research results.

For more information about the NASA STI program, see the following:

- Access the NASA STI program home page at <http://www.sti.nasa.gov>
- E-mail your question via the Internet to help@sti.nasa.gov
- Fax your question to the NASA STI Help Desk at 443-757-5803
- Telephone the NASA STI Help Desk at 443-757-5802
- Write to:
NASA Center for AeroSpace Information (CASI)
7115 Standard Drive
Hanover, MD 21076-1320



Development and Demonstration of a Computational Tool for the Analysis of Particle Vitiating Effects in Hypersonic Propulsion Test Facilities

Hugh Douglas Perkins
Glenn Research Center, Cleveland, Ohio

National Aeronautics and
Space Administration

Glenn Research Center
Cleveland, Ohio 44135

Acknowledgments

I would like to express my appreciation for the ongoing support, counsel and patience of my graduate advisor, Dr. Chih-Jen Sung, in the preparation of this work. I would also like to thank my colleagues Dr. Dan Paxson and Mr. Scott Thomas for their detailed review of this dissertation. Lastly, I would like to thank the NASA Glenn Research Center for its ongoing support of this research and of my overall graduate program.

This work was sponsored by the Fundamental Aeronautics Program
at the NASA Glenn Research Center.

Level of Review: This material has been technically reviewed by technical management.

Available from

NASA Center for Aerospace Information
7115 Standard Drive
Hanover, MD 21076-1320

National Technical Information Service
5301 Shawnee Road
Alexandria, VA 22312

Available electronically at <http://gltrs.grc.nasa.gov>

Contents

Abstract.....	1
1.0 Introduction	1
2.0 Code Description.....	6
2.1 General Approach.....	6
2.2 Gas Phase Governing Equations.....	6
2.3 Thermodynamic Properties.....	7
2.4 Transport Properties.....	8
2.5 Finite-Rate Kinetics	10
2.6 Solid Phase Governing Equations and Numerical Solution Method	11
2.7 Gas Phase Numerical Solution Method	20
3.0 Validation.....	23
3.1 Gas Phase Flow and Chemical Kinetics Validation.....	23
3.2 Particle Drag and Heat Transfer Models and Gas-Solid Momentum and Heat Exchange Models Validation.....	30
3.3 Particle Internal Heat Transfer, Heat Release and Supersonic Drag/Convection Validation ..	34
4.0 Generation of Graphite Kinetic Constants	37
5.0 Model Facility and Scramjet Simulation Geometry and Flow Conditions	39
5.1 Test Facility Components	39
5.2 Scramjet Inlet and Isolator Sections.....	40
5.3 Modeling Approach	44
5.4 Grid Descriptions	45
6.0 Results	45
6.1 Inert Particle Calculations.....	45
6.2 Single Graphite Particle Calculations	57
6.3 One Percent Mass Fraction Graphite Particle Simulations	67
6.4 Ignition Calculations	78
7.0 Conclusions	80
8.0 Recommendations for Future Work	81
8.1 Modeling Improvements	81
8.2 Input Data Improvements	82
8.3 Additional Modeling	82
Appendix A.—Symbols List.....	83
Appendix B.—Gas Phase Kinetic Mechanism	87
References.....	89

List of Tables

Table 1.—Mixer Section Inflow Total Pressure, Total Temperature and dynamic pressure for Mach 5, 6 and 7 Simulated Flight Conditions.....	40
Table 2.—Summary of Model Scramjet Inlet/Isolator Geometry at Mach 7 Design Point	41
Table 3.—Summary of Flow Field Conditions for Model Scramjet	42
Table 4.—Test Article Configuration for Mach 5, 6 and 7 Test Conditions	44
Table 5.—Flow Conditions Along the Pre-Compression Plate for Mach 5, 6, and 7 Test Conditions	44
Table 6.—Gas Temperatures (K) at the Exit of the Isolator Section	78
Table 7.—Species Mass Fractions at the Exit of the Isolator Section	79
Table 8.—Particle Surface Temperature, Velocity, and Porosity for Surviving Graphite Particles at the Exit of the Isolator Section	79
Table 9.—Ignition Delay Time in Microseconds with Vitiates	80

Table 10.—Ignition Delay Time in Microseconds without Vitiates	80
Table B.1.—Gas-Phase Kinetic Mechanism ^c	87
Table B.2.—Third Body Efficiencies	88

List of Figures

Figure 1.—GASL Leg IV diagram	4
Figure 2.—HTF diagram	5
Figure 3.—Particle heat transfer and reaction model.....	13
Figure 4.—Effectiveness factor as a function of temperature.....	17
Figure 5.—Detonation case geometry.	24
Figure 6.—Detonation calculation reference frames.	24
Figure 7.—Detonation wave speed convergence.....	25
Figure 8.—Comparison of pressure profiles between Q1D and ZND codes.....	26
Figure 9.—Comparison of temperature profiles between Q1D and ZND codes.....	26
Figure 10.—Comparison of velocity profiles between Q1D and ZND codes.	27
Figure 11.—Comparison of H ₂ O mole fraction profiles between Q1D and ZND codes.....	27
Figure 12.—Comparison of detonation OH mole fraction profiles between Q1D and ZND codes.	28
Figure 13.—Comparison of detonation CO ₂ mole fraction profiles between Q1D and ZND codes.	28
Figure 14.—Comparison of detonation NO mole fraction profiles between Q1D and ZND codes.	29
Figure 15.—Comparison of detonation NO ₂ mole fraction profiles between Q1D and ZND codes.	29
Figure 16.—Gas temperature profile from Q1D calculation from point of particle insertion compared to gas temperature profile from Maxwell/Seasholtz analysis.....	32
Figure 17.—Gas velocity profile from Q1D calculation from point of particle insertion compared to gas velocity profile from Maxwell/Seasholtz analysis.....	32
Figure 18.—Particle temperature profile from Q1D calculation from point of particle insertion compared to particle temperature profile from Maxwell/Seasholtz analysis.	33
Figure 19.—Particle velocity profile from Q1D calculation from point of particle insertion compared to particle velocity profile from Maxwell/Seasholtz analysis.	33
Figure 20.—A comparison of the post-shock gas-particle relative Mach number profiles between the Q1D and Baek codes.	35
Figure 21.—Internal temperature profiles at 2 μ sec intervals of particle heating up to ignition from Baek code.	35
Figure 22.—Internal temperature profiles at 2 μ sec intervals of particle heating up to ignition from Q1D code.	36
Figure 23.—PGX graphite thermal conductivity.....	38
Figure 24.—PGX graphite heat capacity.....	38
Figure 25.—Q1D kinetic constant fit to Froberg data.	39
Figure 26.—Scaled axisymmetric geometry for facility settling chamber/mixer and nozzle.....	40
Figure 27.—Scramjet geometric design parameters.	41
Figure 28.—Scaled inlet/isolator at Mach 7 design point.....	41
Figure 29.—Scaled inlet/isolator with shock locations corresponding to Mach 6 operation.....	42
Figure 30.—Scaled inlet/isolator with shock locations corresponding to Mach 5 operation.....	42
Figure 31.—(a) Truncated configuration for wind tunnel testing with forebody simulation (precompression) plate and (b) truncated configuration with forebody simulation plate shown schematically with facility mixer and nozzle indicating computational domain.	43
Figure 32.—Nozzle area distribution where X = 0 indicates the beginning of the convergent section of the nozzle.	45
Figure 33.—Tabular alumina heat capacity.....	46
Figure 34.—Tabular alumina thermal conductivity.....	46

Figure 35.—Comparison of gas and single particle surface temperature profiles for various particle sizes for the Mach 5 total temperature flow condition.....	48
Figure 36.—Comparison of gas and single particle velocity profiles for various particle sizes for the Mach 5 total temperature flow condition.....	48
Figure 37.—Comparison of gas and single particle surface temperature profiles for various particle sizes for the Mach 6 total temperature flow condition.....	49
Figure 38.—Comparison of gas and single particle velocity profiles for various particle sizes for the Mach 6 total temperature flow condition.....	49
Figure 39.—Comparison of gas and 10 μm particle surface temperature profiles for Mach 5 and 6 total temperature flow conditions.....	50
Figure 40.—Comparison of gas and 100 μm particle surface temperature profiles for Mach 5 and 6 total temperature flow conditions.....	50
Figure 41.—Comparison of gas and 1000 μm particle surface temperature profiles for Mach 5 and 6 total temperature flow conditions.....	51
Figure 42.—Comparison of gas and 10 μm particle velocity profiles for Mach 5 and 6 total temperature flow conditions.....	51
Figure 43.—Comparison of gas and 100 μm particle velocity profiles for Mach 5 and 6 total temperature flow conditions.....	52
Figure 44.—Comparison of gas and 1000 μm particle velocity profiles for Mach 5 and 6 total temperature flow conditions.....	52
Figure 45.—Radial temperature profiles of 100 μm particles for the Mach 5 and 6 conditions at the exit planes of the mixer/nozzle (MN) and the isolator (IS).....	53
Figure 46.—Radial temperature profiles of 1000 μm particles for the Mach 5 and 6 conditions at the exit planes of the mixer/nozzle (MN) and the isolator (IS).....	54
Figure 47.—Comparison of gas and particle temperature profiles for the Mach 6 total temperature flow condition for a single 10 μm particle and for a 1 percent 10 μm particle mass fraction.....	54
Figure 48.—Comparison of gas temperature profiles for the Mach 6 total temperature flow condition for a single 10 μm particle and for a 1 percent particle mass fraction of 10 μm particles over the last 1.0 m of the nozzle, the precompression plate, the final external compression ramp, and the isolator.....	55
Figure 49.—Comparison of particle temperature profiles for the Mach 6 total temperature flow condition for a single 10 μm particle and for a 1 percent particle mass fraction of 10 μm particles over the last 1.0 m of the nozzle, the precompression plate, the final external compression ramp, and the isolator.....	55
Figure 50.—Comparison of gas and particle velocity profiles for the Mach 6 condition for a single 10 μm particle and for a 1 percent 10 μm particle mass fraction.....	56
Figure 51.—Comparison of gas velocity profiles for the Mach 6 total temperature flow condition for a single 10 μm particle and for a 1 percent particle mass fraction of 10 μm particles over the last 1.0 m of the nozzle, the precompression plate, the final external compression ramp, and the isolator.....	56
Figure 52.—Comparison of particle velocity profiles for the Mach 6 total temperature flow condition for a single 10 μm particle and for a 1 percent particle mass fraction of 10 μm particles over the last 1.0 m of the nozzle, the precompression plate, the final external compression ramp, and the isolator.....	57
Figure 53.—Mass fractions of minor species from Mach 7 total temperature reacting flow simulation.....	58
Figure 54.—Comparison of mass fractions of major species from Mach 7 total temperature simulations with and without finite-rate chemistry.....	58
Figure 55.—Comparison of static temperature profiles from Mach 7 total temperature simulations with and without finite-rate chemistry.....	59

Figure 56.—Mach 5 graphite versus alumina surface temperature comparison.....	60
Figure 57.—Mach 6 graphite versus alumina surface temperature comparison.....	60
Figure 58.—Mach 7 surface temperature results.....	61
Figure 59.—Radial temperature profiles of the 1000 μm particle for the Mach 5, 6 and 7 conditions at the exit planes of the mixer/nozzle (MN) and the isolator (IS).....	62
Figure 60.—Mach 5 graphite versus alumina velocity comparison.....	62
Figure 61.—Mach 6 graphite versus alumina velocity comparison.....	63
Figure 62.—Mach 7 velocity results.....	63
Figure 63.—Graphite particle porosity.....	64
Figure 64.—Mach 5 gas-particle relative mach number.....	65
Figure 65.—Heat flows for 10 μm graphite particle at Mach 5 total temperature condition.....	66
Figure 66.—Heat flows for 100 μm graphite particle at Mach 5 total temperature condition.....	66
Figure 67.—Heat flows for 1000 μm graphite particle outer shell at Mach 5 total temperature condition.....	67
Figure 68.—Comparison of particle temperature and velocity profiles between a single 10 μm graphite particle and a 1 percent mass fraction of 10 μm graphite particles at the Mach 5 total temperature flow condition.....	68
Figure 69.—Comparison of particle temperature and velocity profiles between a single 10 μm graphite particle and a 1 percent mass fraction of 10 μm graphite particles at the Mach 6 total temperature flow condition.....	69
Figure 70.—Comparison of particle temperature and velocity profiles between a single 10 μm graphite particle and a 1 percent mass fraction of 10 μm graphite particles at the Mach 7 total temperature flow condition.....	69
Figure 71.—Comparison of particle temperature and velocity profiles between a single 100 μm graphite particle and a 1 percent mass fraction of 100 μm graphite particles at the Mach 5 total temperature flow condition.....	70
Figure 72.—Comparison of particle temperature and velocity profiles between a single 100 μm graphite particle and a 1 percent mass fraction of 100 μm graphite particles at the Mach 6 total temperature flow condition.....	71
Figure 73.—Comparison of particle temperature and velocity profiles between a single 100 μm graphite particle and a 1 percent mass fraction of 100 μm graphite particles at the Mach 7 total temperature flow condition.....	71
Figure 74.—Comparison of particle temperature and velocity profiles between a single 1000 μm graphite particle and a 1 percent mass fraction of 1000 μm graphite particles at the Mach 5 total temperature flow condition.....	72
Figure 75.—Comparison of particle temperature and velocity profiles between a single 1000 μm graphite particle and a 1 percent mass fraction of 1000 μm graphite particles at the Mach 6 total temperature flow condition.....	72
Figure 76.—Comparison of particle temperature and velocity profiles between a single 1000 μm graphite particle and a 1 percent mass fraction of 1000 μm graphite particles at the Mach 7 total temperature flow condition.....	73
Figure 77.—Comparison of particle porosity profiles between single graphite particles and a 1 percent mass fraction of graphite particles at the Mach 5 total temperature flow condition.....	73
Figure 78.—Comparison of particle porosity profiles between single graphite particles and a 1 percent mass fraction of graphite particles at the Mach 6 total temperature flow condition.....	74
Figure 79.—Comparison of particle porosity profiles between single graphite particles and a 1 percent mass fraction of graphite particles at the Mach 7 total temperature flow condition.....	74
Figure 80.—Comparison of NO mass fraction profiles between no graphite particles and a 1 percent mass fraction of graphite particles.....	75

Figure 81.—Comparison of NO ₂ mass fraction profiles between no graphite particles and a 1 percent mass fraction of graphite particles.....	76
Figure 82.—Comparison of O mass fraction profiles between no graphite particles and a 1 percent mass fraction of graphite particles.....	76
Figure 83.—Comparison of CO ₂ mass fraction profiles between 1 percent graphite particle mass fraction cases.....	77
Figure 84.—Comparison of CO mass fraction profiles between 1 percent graphite particle mass fraction cases.....	78
Figure 85.—Example of ignition point for a H ₂ /vitiated air/particle mixture from the Mach 6 total temperature simulation with a 1 percent mass fraction of 1000 μm graphite particles.....	79

Development and Demonstration of a Computational Tool for the Analysis of Particle Vitiation Effects in Hypersonic Propulsion Test Facilities

Hugh Douglas Perkins
National Aeronautics and Space Administration
Glenn Research Center
Cleveland, Ohio 44135

Abstract

In order to improve the understanding of particle vitiation effects in hypersonic propulsion test facilities, a quasi-one dimensional numerical tool was developed to efficiently model reacting particle-gas flows over a wide range of conditions. Features of this code include gas-phase finite-rate kinetics, a global porous-particle combustion model, mass, momentum and energy interactions between phases, and subsonic and supersonic particle drag and heat transfer models. The basic capabilities of this tool were validated against available data or other validated codes.

To demonstrate the capabilities of the code, and to provide initial insight into the effects of various particle laden flows on ignition, a series of computations were performed for a model hypersonic propulsion test facility and scramjet. Parameters studied were simulated flight Mach number (Mach 5, 6, and 7), particle size (10, 100, and 1000 μm diameters), particle mass fraction (single particle and 1 percent) and particle material (alumina and graphite). For the alumina particles, it was found that the presence of particles up to 1 percent mass fraction had very little effect on the gas phase, even though only the 10 μm particles closely followed the gas flow velocity and temperature. With the graphite particles, the 10 μm particles were either quickly quenched, or were quickly consumed, depending on the gas temperature. As the particle size was increased to 100 μm , the particles did not quench, but were still typically consumed within the model test facility. For the 1000 μm particles, combustion was diffusion limited, so particle and gas temperature had little effect on the combustion rate. When the particle mass fraction was increased to 1 percent, the main change was the addition of significant heat release. In those cases where low graphite reaction rates were observed for single particles, the increase to 1 percent mass fraction had very little impact.

Hydrogen/vitiated air ignition delay calculations for the 1 percent mass fraction of graphite particles cases showed significant decreases in ignition delay in cases where higher graphite combustion rates were observed. Further calculations showed that this was due primarily to increased combustor inlet temperature, not the gaseous or solid vitiate species present in the flow.

1.0 Introduction

The principle challenge associated with ground testing of hypersonic airbreathing propulsion systems is the requirement to heat the air supply to temperatures in excess of 1300 K prior to expansion through the facility nozzle. Over the last 40 years, several different methods have been employed to accomplish this heat addition. The most commonly used method is combustion heating, wherein fuel is burned in the air stream to bring the flow temperature up to the required stagnation temperature, and then makeup oxygen is added to bring the flow composition back to the normal 21 percent oxygen mole fraction. Several facilities have been built which utilize an electric arc to heat the air in a stilling chamber to very high temperatures. This flow is then mixed with additional high pressure air to create an air flow at the desired stagnation temperature which is then supplied to the facility nozzle. Lastly, heat sink storage heaters have also been built for several additional facilities. In these facilities, a large mass of a refractory material in the form of pebbles or drilled blocks is heated to a temperature significantly above the desired

air stagnation temperature prior to the propulsion system test. The test air then flows through the refractory material which heats the air to a temperature slightly above the required stagnation temperature. Additional high pressure air is then added to the heated air to achieve the test stagnation temperature set point. It should be noted that heat exchangers and electrical resistance heaters that are typically used for lower Mach number propulsion test facilities cannot be used at the significantly higher temperatures required for hypersonic propulsion testing due to structural and heat flux limitations. Detailed descriptions of the operational procedures and limitations of each type of hypersonic propulsion test facility can be found in the JANNAF Scramjet Testing Recommended Practices and Guidelines (Weber, 2002).

Each of the heating methods described above introduces contamination into the facility air flow, typically referred to as vitiation. This flow vitiation results in some level of departure of the ground test results from that which would be seen in free flight. For the combustion heated facility, the products of combustion remain in the air flow. If hydrogen is used as the heater fuel, the product is primarily water. If a hydrocarbon fuel is used, carbon dioxide would also be present. If the fuel/air mixing scheme is not adequate or if the heater combustion length is insufficient for the given test condition, unburned fuel may also be present in the flow. As the simulated Mach number is increased, the higher temperature of the mixture results in an increasing mole fraction of combustion radicals, such as H, O, and OH, as well as NO and NO₂, exiting the heater and entering the nozzle, in addition to the increasing fraction of water vapor and carbon dioxide. If a hydrocarbon fuel is used, the fraction of carbon monoxide present in the air stream also increases with increasing simulated Mach number. The rapid expansion of the heater outflow through the facility nozzle freezes the composition at a point downstream of the nozzle throat, so that the mixture is not allowed to equilibrate. Under some circumstances, water droplets may form as the water vapor becomes supercooled due to the expansion to high altitude flight conditions. This condensation is rarely seen at the test point, in practice.

As the combustion heated air enters the engine inlet, the changes in the ratio of specific heats, γ , and the gas molecular weight alter the shock structure from what would be seen in clean air. A variety of other physical characteristics of the flow are also altered due to the flow vitiation, such as heat transfer rates, vibrational energy relaxation rates, turbulence, and inlet flow distortion, among others. As the flow enters the combustor and fuel is added, the combustion kinetics can be significantly altered, effecting both ignition and flame holding in ways that can be hard to predict, due to a variety of competing mechanisms. Lastly, nozzle expansion is also effected by the flow composition. As can be seen by the list above, combustion heater vitiation adds a large amount of uncertainty to the test results. Additional detail on these effects can be found in the summary papers of Powell and Stallings (1998), Pellett, et al. (2002) and Fry (2004). Additional difficulty is incurred with combustion heated facilities in terms of determining which primary variables should be matched during the testing. The changes in gas properties makes it impossible to match both total temperature and total enthalpy, both Mach number and velocity, or both total pressure and static pressure, for instance. The experimentalist must evaluate which properties are key(s) for each test, a subject of much debate in the hypersonic engine testing community through the years.

If an arc heater is used, high levels of NOx are formed in the vicinity of the arc, which can persist in the mixed flow entering the nozzle at mole fractions above 3 percent. These compounds have little effect on the shock structure or other aerodynamic features, but can significantly catalyze the ignition process (Slack and Grillo, 1977).

Lastly, a storage heater generally represents the lowest level of chemical vitiation. Like the arc heater, a storage heater can generate some NOx, but not to the same level. At most, an equilibrium concentration of NOx might be generated, depending on the residence time of the air mixture at high temperature. As the thermal generation of NOx is fairly slow, it is possible that NOx levels below equilibrium might be present in some facilities, depending on the specifics of the facility configuration.

The above discussion gives a brief overview of the gas-phase vitiation issues for hypersonic airbreathing propulsion ground test facilities. However, each of these facility types can produce particulate vitiation as well. For the combustion heated facility, the particulate source is most likely soot

formed during the combustion process due to the existence of fuel rich regions in the hydrocarbon fuel/air mixing zone. Additional particulates may be present due to piping corrosion caused by hot water vapor. In an arc heated facility, electrode erosion releases a small amount of metallic particulates into the air stream. In a storage heater facility, eroded particles from the refractory material, a ceramic or graphite, are found in the air stream. While the quantities and size distributions of these particulates have generally not been characterized, it can be assumed that the level of particulate vitiation is highest with storage heaters due to the extremely large surface area of non-surface abrasion resistant material exposed to the flow. While the most recent surveys of the state of the art regarding the effects of vitiation (Fry, 2004; Pellett, et al., 2002) acknowledge the importance of particulate vitiation, only a single study has ever been conducted of the potential effects of particulates (Mitani, 1995). In contrast, the surveys of Fry (2004) and of Pellett, et al. (2002), reference dozens of past studies addressing various aspects of gas-phase vitiation, reflected in the summary of effects described above.

Mitani (1995) performed a series of theoretical analyses to determine the effect of low micron-sized inert particles, assumed to be in thermal equilibrium with the carrier gas, on scramjet combustor ignition and flameholding. Mitani concluded that a mass fraction above 0.1 percent can inhibit ignition through the mechanism of radical termination on the particle surface. This mechanism is only valid for particles smaller than 3 μm in diameter. For the particles to have a thermal heat sink effect, the study concluded that a mass fraction in excess of 10 percent would be required.

In order to look at the effects of larger particles that are not in equilibrium with the carrier gas, as well as reacting particles, throughout the test facility flow path, a numerical analysis is necessary. However, up to this time, no numerical modeling has ever been done to examine the potential effects of particle vitiation in hypersonic propulsion ground test facilities. Reasons for this include:

1. The effects of particles have been conveniently assumed to be of secondary importance compared to the effects of gas phase vitiation.
2. The numerical analysis tools typically used for hypersonics flows do not contain particle flow models. The existing tools are multi-dimensional codes with finite-rate chemistry capability characterized by long run times, and so the addition of particle flow models is not attractive as it would tend to require even longer computational turn-around times.
3. Particle-gas flow interaction models that cover the broad range of conditions experienced in a hypersonic propulsion test facility are not readily available.
4. The mass loading and size distribution of particle vitiates has not been determined, so key inputs for model formulation are not available.

While the first assumption, that particle vitiation effects are of secondary importance compared to gas-phase vitiation effects, may well be valid for combustion heated facilities, and perhaps arc-heated facilities as well, it is not a good assumption for storage heater-based facilities. In storage heater-based facilities, the amount of particle vitiation is likely to be substantially higher than in other types of facilities, and the amount of gas-phase vitiation is significantly lower. The final three reasons given above can be addressed, all or in part, through the development of appropriate particle-gas flow models and applying them to a quick turn-around numerical tool. By integrating the typically computationally demanding particle flow analysis into a more rapid analysis tool, parametric studies of particles of various sizes and other pertinent characteristics can be performed in a timely manner to understand under what conditions particle vitiation may be of concern.

In this work, a quasi-one-dimensional (Q1D) numerical modeling tool and associated sub-models are developed that allow for a relatively rapid exploration of the effects of particle vitiation throughout the operating envelope of a storage-heated hypersonic propulsion test facility. A wide range of particle sizes are considered for both chemically inert particles (alumina) and reacting particles (graphite). In order to appropriately define the ranges of the parameters to be modeled, both a test facility and a scramjet engine model (up through the combustor) are laid out as part of this study. The test facility model is a compromise between the geometry and flow characteristics of the two large scale storage heater scramjet

test facilities found in the United States. This same model facility and model scramjet will then be used to demonstrate the use of the Q1D code for simulating hypersonic propulsion test flows with both inert and reacting particles.

The first storage heater based hypersonic propulsion test facility is the GASL Leg IV facility. The facility consists of an alumina matrix storage heater followed by hydrogen fueled booster heater. The storage heater can heat dry air to a total temperature of 1390 K, simulating approximately Mach 5, with the booster heater then adding thermal energy up to a Mach 7 condition (Roffe, et al., 1997). The basic configuration is shown in Figure 1.

The second configuration to be studied is the NASA Glenn Research Center Hypersonic Tunnel Facility (HTF) located at the NASA Plumbrook Station in Sandusky, Ohio. This facility consists of a drilled-core graphite block heater capable of heating gaseous nitrogen to 2500 K. The heated nitrogen is then mixed with ambient temperature gaseous oxygen to provide simulated air to the facility nozzle at a total temperature up to 2170 K (Perkins, et al., 1998). This basic configuration is shown in Figure 2.

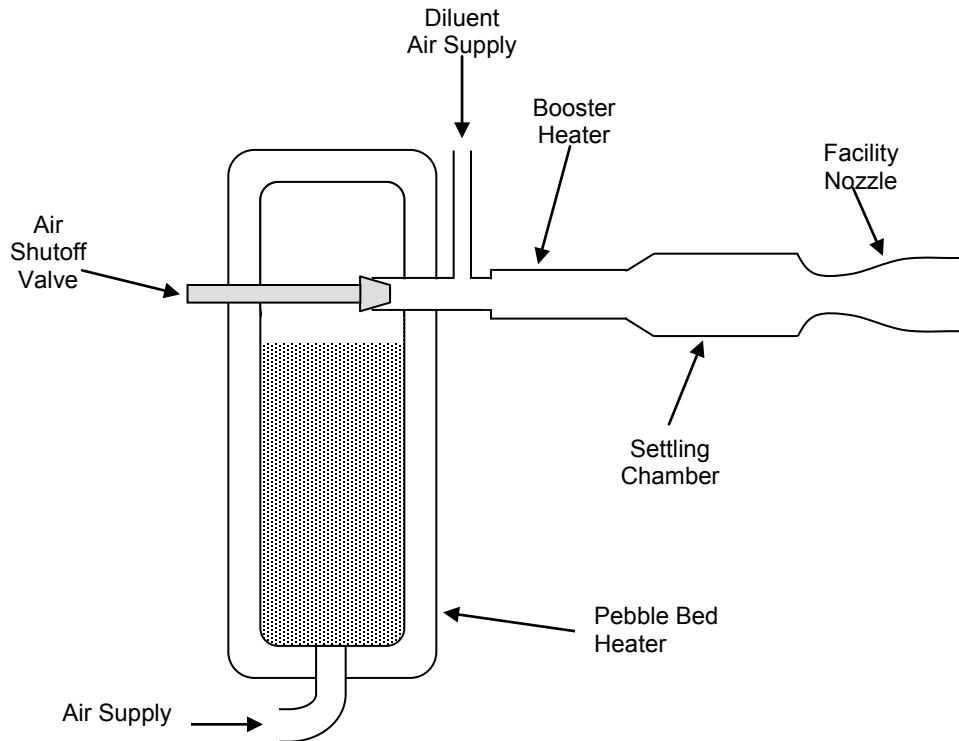


Figure 1.—GASL Leg IV diagram.

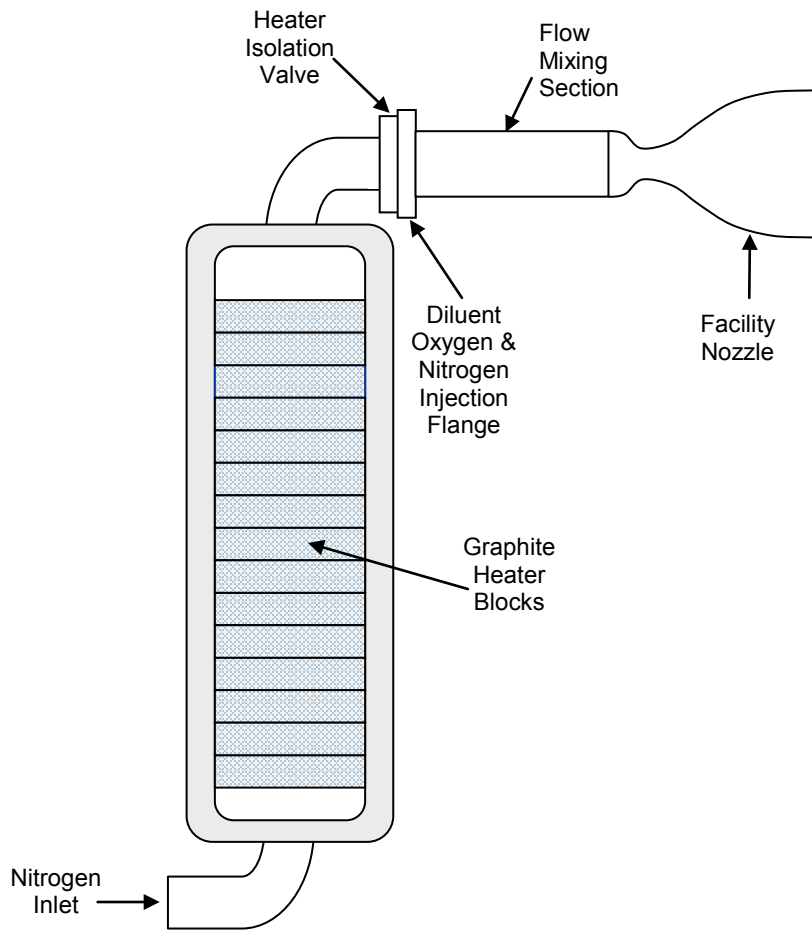


Figure 2.—HTF diagram.

While the GASL Leg IV facility is vitiated above Mach 5, the model facility will assume non-vitiated flow for both the inert and the reacting particles at all test Mach numbers, as vitiated flow for the inert particle case would significantly affect the nozzle flow and inlet shock structure, making comparisons difficult between the different particle types.

Neither GASL Leg IV nor HTF have ever been characterized as far as particle size and concentration as a function of test condition. Therefore, these particle properties will be dealt with parametrically when the code is exercised through a range of test conditions. There is no reason to assume that particle size is limited to a few microns diameter, as assumed by Mitani (1995). In the case of the HTF facility, particles on the order of 1 mm have been observed adhering to the heater graphite blocks during facility maintenance. Therefore, particle diameters in the range of 10 μm to 1 mm will be considered. Neither inert nor reacting particles with diameters less than 10 μm were used in this analysis as such small particles would be expected to track the gas flow very closely (Maxwell and Seasholtz, 1974) and, as will be shown in the following analysis, the 10 μm graphite particles almost immediately quench or are consumed, so a smaller particle would not be expected to show any different behavior. A particle mass fraction of 1 percent of the total test flow will be used as an upper bound, since a higher mass fraction would represent such a significant mass loss from the storage heater that heater refurbishment would likely be required after each test program. Such heater degradation has never been reported. While the results of this parametric study will not conclusively determine whether or not particle vitiation is of concern at any particular test point for a particular test facility, it will provide insight into what particle concentrations and sizes may be of concern for future research test programs.

In the following sections, the Q1D code and its sub-models will be described and the results of a series of validation cases based on the above range of conditions will be given. The code is then exercised through a parametric study of particle and gas flow combinations appropriate to the model test facility and model scramjet. Results are presented and conclusions are drawn as to the potential effects of particle vitiates. Finally, recommendations for further study are presented.

2.0 Code Description

2.1 General Approach

The need to model a large number of facility and test hardware components over a wide range of parameter space, as well as the need to consider two phase flow with mass, momentum and energy interactions between the phases and finite rate combustion kinetics, limits the number of dimensions that can be practically used for the analysis. For this reason, a quasi-one-dimensional (Q1D) analysis approach was selected for the underlying gas-phase code. No existing code was available with the requisite characteristics for this study. A custom Eulerian (fixed grid), gas-phase, multispecies, time-accurate, Q1D computational fluid dynamics (CFD) code with finite rate kinetics was therefore written and validated. To this code was then added a Lagrangian particle tracking scheme with a global particle reaction model. Since larger particles are considered, an internal one-dimensional grid is generated for each particle being tracked which is solved at each time step for the particle internal temperature gradient and the heat transfer to the gas phase. If the particles are sufficiently small such that the Biot number is expected to remain less than 0.1 (based on the particle radius as the characteristic dimension, (Incropera and Dewitt, 2002) throughout the simulation, the particle is treated as isothermal. This is easily accomplished within the code by setting the number of internal particle grid points to two, as the number of shells within the particle is equal to one less than the number of internal grid points. Mass, momentum, energy and species source terms are included in the gas-phase governing equations to provide feedback from the particle drag, heat transfer, and reaction models. For inert particles, the particle reaction model is simply turned off. When the particle mass fraction is high enough that the number of particles being tracked would be too high for efficient and timely computation, each particle tracked is defined as being a representative particle for a larger number of particles at that same location. The number of particles represented by each tracked particle is provided as a user input. The mass, momentum and energy contributions from each tracked particle are then multiplied by the number of particles in each set to get the gas-phase source terms.

This modeling approach allows for a large number of computations to be performed, but with certain drawbacks. Boundary layer related effects cannot be captured, nor can oblique shocks. Perhaps the biggest drawback for this problem is that the lateral diffusion of the particles when passing through a divergent section at high flow velocity is not captured. Previous studies have shown that when two-phase flow passes through a convergent-divergent nozzle, the particle stream will “separate” from the wall, creating a particle-free zone near the wall (Chang, 1980; Ishii, et al., 1987). The concentration of particles therefore increases in the rest of the flow. This effect is more pronounced as particle size is increased. However, since this study is parametric in nature, this effect can be accounted for when the results are applied to a specific configuration by correcting the particle concentration based on the nozzle flow conditions and the particle size under consideration.

2.2 Gas Phase Governing Equations

The gas phase governing equations were adapted from Kuo (1986), re-derived to include area variation. Viscous dissipation and diffusion terms determined to be unimportant for these simulations are omitted. The ϕ term represents the local volume fraction of gas in the gas-solid mixture. The source terms, S_m , S_p , S_e , come from the solid phase relations, while the species source terms, $S_{m,i}$, are a summation of both the gas phase and solid phase reactions.

Continuity:

$$\frac{\partial}{\partial t}(\rho_g A \phi) = -\frac{\partial}{\partial x}(\rho_g u_g A \phi) + \phi A S_m \quad (1)$$

Momentum:

$$\frac{\partial}{\partial t}(\rho_g A \phi u_g) = -\frac{\partial}{\partial x}(\rho_g A \phi u_g^2 + p A \phi) + \phi A S_p + p \phi \frac{\partial A}{\partial x} \quad (2)$$

Energy:

$$\frac{\partial}{\partial t}(\rho_g A \phi e_g) = -\frac{\partial}{\partial x}(\rho_g A \phi u_g e_g + p A \phi u_g + q_c A \phi) + \phi A S_e - q_w \sqrt{4 A \pi} \quad (3)$$

where

$$q_c = -k_g \frac{\partial T_g}{\partial x} \quad (4)$$

and

$$e_g = h_g - R T_g \quad (5)$$

Species Continuity:

$$\frac{\partial}{\partial t}(\rho_g Y_i A \phi) = -\frac{\partial}{\partial x}(\rho_g Y_i (u_g + v_i) A \phi) + \phi A S_{m,i} \quad (6)$$

where

$$v_i = -\frac{D_i}{Y_i} \frac{\partial Y_i}{\partial x} \quad (7)$$

The q_w wall heat transfer term is currently a user input that can be used to “tune” the computational results to match available experimental data. If data are unavailable, an approach based on the Reynolds-Colburn analogy relating wall friction to heat transfer has been shown to be effective for Q1D calculations (Paxson, 1993) and could be readily incorporated.

2.3 Thermodynamic Properties

The basic thermodynamic properties for each species, enthalpy ($h_{g,i}$), enthalpy of formation ($h_{o,i}$), specific heat ($c_{p,i}$), Gibbs energy of formation ($g_{f,i}^\circ$) and molecular weight (M_i), were all taken from the JANNAF Thermochemical Tables (Chase, et al., 1986). The temperature dependent properties were piece-wise curve fit over four temperature ranges using third-order polynomials. The four temperature ranges were 0 to 300 K, 300 to 600 K, 600 to 1100 K, and 1100 to 3000 K. The use of four temperature ranges provided high accuracy over the entire temperature range, typically within 0.1 percent of the original JANNAF data. From this data, along with the mass fractions of each species, the mixture properties can be defined, as follows.

$$h_g = \sum_{i=1}^{ns} Y_i (h_{g,i} + h_{to,i}) \quad (8)$$

$$C_p = \sum_{i=1}^{ns} Y_i C_{p,i} \quad (9)$$

$$g_f^o = \sum_{i=1}^{ns} Y_i g_{f,i}^o \quad (10)$$

For some of the calculations, the mole fractions of the chemical species are needed instead of mass fractions, which can be easily calculated as follows.

$$X_i = \frac{Y_i / M_i}{\sum_{i=1}^{ns} Y_i / M_i} \quad (11)$$

Once the mole fractions are calculated, the mixture molecular weight can be obtained.

$$M = \sum_{i=1}^{ns} X_i M_i \quad (12)$$

This leads to the simple relation for the mixture gas constant, given the universal gas constant,

$$R = \frac{R_u}{M}, \quad (13)$$

and the ratio of specific heats can then be defined as

$$\gamma = \frac{C_p}{C_p - R}. \quad (14)$$

2.4 Transport Properties

Species effective collision diameter (σ_i) and effective temperature ($T_{e,i}$) data, taken from Svehla (1962) and Hirschfelder, Curtiss, and Bird (1964), were combined with the Prandtl number (0.706) to generate the transport properties used in the calculations. Following the methodology found in White (1991), the binary diffusion coefficients are first calculated.

$$D_{i,j} = \frac{0.001858 T_g^{3/2} \left[\frac{M_i + M_j}{M_i M_j} \right]^{1/2}}{P \sigma_{i,j}^2 \Omega_{D_{i,j}}} \quad (15)$$

Where the collision integral is defined as

$$\Omega_{D_{i,j}} = T_g^*_{i,j}^{-0.145} + (T_g^*_{i,j} + 0.5)^{-2} \quad (16)$$

and where

$$T_g^*_{i,j} = \frac{T_g}{T_{\varepsilon_{i,j}}} \quad (17)$$

$$T_{\varepsilon_{i,j}} = \sqrt{T_{\varepsilon_i} T_{\varepsilon_j}} \quad (18)$$

and

$$\sigma_{i,j} = \frac{1}{2}(\sigma_i + \sigma_j). \quad (19)$$

Once the binary diffusion coefficients have been calculated, an “average” diffusion coefficient for each species diffusing into the rest of the mixture can be calculated, using the following relation from Warnatz, et al. (1999).

$$D_i = \frac{1 - Y_i}{\sum_{j=1, j \neq i}^{ns} \frac{X_j}{D_{i,j}}} \quad (20)$$

While the use of an average diffusion coefficient is somewhat less accurate than using a full multispecies diffusion model, it is much less computationally demanding and was deemed sufficiently accurate (~10 percent) for the purposes of this study.

To calculate the individual species viscosity, the method described in Hirschfelder, Curtiss, and Bird (1964) is adopted.

$$\mu_i = \frac{26.993(M_i T_g)^{1/2}}{\Omega_{2,2} \sigma_i^2} \quad (21)$$

where the collision integral, $\Omega_{2,2}$, is represented by the curve fit

$$\Omega_{2,2} = 0.5015 + 2.5715(e^{-2.1448T^*_{2,2}}) + 0.6391(e^{-0.3856T^*_{2,2}}) + 0.3546(e^{-0.0161T^*_{2,2}}) \quad (22)$$

and

$$T^*_{2,2} = \frac{T_g}{T_{\varepsilon_i}} \quad (23)$$

The mixture viscosity is then calculated using Wilke’s law, as given by Drummond (1990).

$$\mu = \frac{\sum_1^{ns} \frac{\mu_i}{1 + \frac{1}{X_i} \sum_{j=1, j \neq i}^{ns} X_j \varphi_{ij}}}{\sum_1^{ns} \frac{\mu_i}{1 + \frac{1}{X_i} \sum_{j=1, j \neq i}^{ns} X_j \varphi_{ij}}} \quad (24)$$

where

$$\varphi_{ij} = \frac{\left[1 + \left(\frac{\mu_i}{\mu_j} \frac{\rho_i}{\rho_j} \right)^{0.5} \left(\frac{M_i}{M_j} \right)^{0.25} \right]^2}{\frac{4}{\sqrt{2}} \left(1 + \frac{M_i}{M_j} \right)^{0.5}} \quad (25)$$

Lastly, the mixture thermal conductivity is simply calculated by the standard expression

$$k_g = \frac{C_p \mu}{\text{Pr}}. \quad (26)$$

All of the above expressions assume laminar flow.

2.5 Finite-Rate Kinetics

Each of the N chemical reactions used in the gas-phase reaction mechanism, shown symbolically in Equation (27), is modeled using the standard Arrhenius expression for the forward reaction rate, Equation (28).



$$k_f = A_f T_g^n e^{\frac{-E_a}{R_u T_g}} \quad (28)$$

The reverse reaction rate can be found from the relation

$$k_b = \frac{k_f}{K_{eq}} \quad (29)$$

where the equilibrium constant, K_{eq} , is calculated from the Gibbs energy of formation for each species and the reaction coefficients from Equation (27), following the procedure found in Kuo (1986).

For this study, it was necessary to assemble a chemical kinetic mechanism that included H, O, N, and C compounds in order to capture the basic hydrogen combustion process for a scramjet combustor as well as the effects of the flow vitiates of interest. Based on a review of the available literature on gas-phase vitiation, as outlined in the introduction, the H-O species H₂, O₂, H₂O, OH, H, O, HO₂, and H₂O₂ were selected. The nitrogen species N, HNO, NO and NO₂ were added to the basic diluent N₂ to capture dissociation and vitiation effects. Lastly, CO, CO₂, and HCO were included as gas-phase products from the combustion of the carbon particles under study. The mechanism developed by Davis, et al. (2005), for H₂-CO combustion was adopted for the bulk of the mechanism used for this study. The nitrogen chemistry was added from the GRI 3.0 mechanism (Smith, et al. 2005). The details of the combined mechanism are given in Appendix B.

Once obtained, the forward and reverse reaction rate constants are used in the standard law of mass action expression to obtain the change in moles of each species for each reaction. These molar changes are then summed across all of the reactions, and then utilized as source terms within the governing equations.

2.6 Solid Phase Governing Equations and Numerical Solution Method

There are two fundamental approaches that can be taken when formulating the governing equations for the solid phase in a two-phase computation. The first is to assume that the particles form a continuum that can be treated in the same manner as the gas phase. A parallel set of conservation equations to the gas phase equations can then be set up for the solid phase, simply exchanging $(1-\phi)$ for ϕ as the volume fraction occupied by the flow, and making the source terms of opposite sign in Equations (1) through (3). This is the approach, referred to as Eulerian, taken by Kuo (1986), Ludwig and Roth (1997), and Di Giacinto et al. (1982), among many others, and is typical of computations of fluidized beds.

Alternately, each particle can be tracked individually in a Lagrangian frame of reference. In this formulation, position, velocity, mass, and temperature of each particle are updated at each time step based on mass, momentum and energy interactions with the gas phase and any surface reactions that may occur. This approach is typically used for very dilute particle concentrations with relatively small computational domains where the computational load is not unreasonable. This method was adopted by Egolfopoulos and Campbell (1999), and Zhou et al. (2002) in order to capture physical phenomena that could not be easily examined using the more traditional Eulerian approach.

For this study, the Lagrangian formulation was adopted as the mass loading of particles was expected to be relatively low, and the consideration of larger particles made the continuum assumption required for the Eulerian approach appear questionable. Since these calculations are Quasi-1D, the calculations are additionally simplified by the lack of radial variation. This allows a single particle to be used computationally to represent all the particles at a given axial position, significantly reducing the number of particles that need to be analyzed at each time step. Particles are therefore inserted into the computational domain at the inflow boundary as sets of particles, with the number of particles in a set determined by the particle size and mass loading, for which only a single particle calculation must be performed per time step. The gas-particle interaction terms in the governing equations are then the results of the single particle calculation for a particle set at a given axial location multiplied by the number of particles in that particular set. This is particularly helpful for very small particles, where the number of particles can become very large even at small mass loadings. Once the gas-particle interaction terms have been calculated for a given set of particles, these values are linearly interpolated onto the gas-phase fixed grid for use in the gas-phase solution process.

After a particle (or set of particles, hereafter referred to as though it were a single particle) is injected into the gas-phase flow with an initial mass, position, velocity, and temperature, a series of relations for spherical particles are used to determine the particle drag, heat transfer, and surface reaction rate that is to be applied to the particle.

The first gas-particle interaction is aerodynamic drag. For laminar flow, White (1991) provides the following drag relation for a sphere.

$$F_p = \frac{1}{2} C_D \rho_g |u_g - u_p| (u_g - u_p) \pi r_p^2 \quad (30)$$

Many empirical relations have been proposed for the drag coefficient of a sphere. Carlson and Hoglund (1964) and Crowe (1967) developed correlations, based on the data available at the time, which have been used frequently for particle flow simulations. More current efforts, such as that of Igra and Takayama (1993) have provided more accurate expressions over a specific flow properties range based on detailed shock tube data. The drag coefficient used for this study is taken from Henderson (1976). This expression covers a very broad range of Reynolds number and Mach number with reasonable accuracy. As the relative velocity between the flow and the particles in this study could range from supersonic to near zero, and the static pressure from 80 atmospheres down to 0.1 atmospheres or less, it is important to cover the broadest possible range of the relative Mach and Reynolds numbers. The Henderson drag coefficient expression was developed from the extensive experimental data base compiled by Bailey and Hiatt (1971) through a series of ballistic range experiments and is accurate to within 16 percent across the

entire range considered. The expression is divided into three elements to cover the entire relative Mach number range. For a subsonic relative Mach number,

$$C_D = 24 \left[\text{Re}_{rel} + \text{MSR} \left\{ 4.33 + \left(\frac{3.65 - 1.53 \frac{T_p}{T_g}}{1 + 0.353 \frac{T_p}{T_g}} \right) e^{\left(-0.247 \frac{\text{Re}_{rel}}{\text{MSR}} \right)} \right\}^{-1} \right. \\ \left. + e^{\left(\frac{-0.5 M_{rel}}{\sqrt{\text{Re}_{rel}}} \right)} \left[\frac{4.5 + 0.38(0.03 \text{Re}_{rel} + 0.48 \sqrt{\text{Re}_{rel}})}{1 + 0.03 \text{Re}_{rel} + 0.48 \sqrt{\text{Re}_{rel}}} + 0.1 M_{rel}^2 + 0.2 M_{rel}^8 \right] \right. \\ \left. + \left[1 - e^{\left(\frac{-M_{rel}}{\text{Re}_{rel}} \right)} \right] 0.6 \text{MSR} \right] \quad (31)$$

where the molecular speed ratio is defined as

$$\text{MSR} = M_{rel} \sqrt{\frac{\gamma}{2}} \quad (32)$$

For a supersonic relative Mach number greater than 1.75,

$$C_D = \frac{0.9 + \frac{0.34}{M_{rel}^2} + 1.86 \left(\frac{M_{rel}}{\text{Re}_{rel}} \right)^{\frac{1}{2}} \left[2 + \frac{2}{\text{MSR}^2} + \frac{1.058}{\text{MSR}} \left(\frac{T_p}{T_g} \right)^{\frac{1}{2}} - \frac{1}{\text{MSR}^4} \right]}{1 + 1.86 \left(\frac{M_{rel}}{\text{Re}_{rel}} \right)^{\frac{1}{2}}} \quad (33)$$

In both the subsonic and supersonic equations, the relative Mach and Reynolds numbers are evaluated at free stream conditions. If the relative Mach number lies between 1.0 and 1.75, then the drag coefficient is taken as a linear interpolation between the value calculated using the subsonic Equation (31) with a Mach number of 1.0 and the value calculated using the supersonic Equation (33) with a Mach number of 1.75, expressed as,

$$C_D(M_{rel}, \text{Re}_{rel}) = C_D(1.0, \text{Re}_{rel}) + \frac{4}{3}(M_{rel} - 1.0)(C_D(1.75, \text{Re}_{rel}) - C_D(1.0, \text{Re}_{rel})) \quad (34)$$

The relative Reynolds number is evaluated at the actual free stream conditions for use in Equation (34). The gas-phase properties used in these equations are evaluated at the particle location, linearly interpolated between the nearest adjacent grid points.

Once the force on the particle is calculated, the particle position and velocity can be updated by the simple relations,

$$x_p^{i+1} = x_p^i + u_p^i \Delta t \quad (35)$$

and

$$u_p^{i+1} = u_p^i + \frac{F_p^i}{m_p^i} \Delta t . \quad (36)$$

Performing the energy balance on a large reacting particle in a convective flow has a number of complexities that need to be considered. Since the particle can be relatively large, a uniform particle temperature cannot be assumed, and an internal grid must be used to capture the temperature gradient within the particle. Since significant velocity slip is expected between the particle and the gas, convection must be modeled. Radiation losses must also be modeled since the gas surrounding the very hot, high emissivity particles is expected to be optically thin, and the test facility walls are water cooled. And, of course, since the particles are reacting, a large amount of heat is input to this system via combustion.

If a thin shell at the outer surface of the particle is considered, as shown in Figure 3, an energy conservation Equation (37) can be written for that shell that encompasses each of the heat flows described above, and which allows for the accumulation or depletion of heat energy in the outer shell.

$$q_{\text{accum}} = q_{\text{comb}} - q_{\text{rad}} - q_{\text{conv}} - q_{\text{cond}} \quad (37)$$

Heat energy will then be conducted into or out of the particle interior over time at a rate controlled by the thermal diffusivity of the particle material. For the conduction, convection, and radiation terms, simple textbook relations are used, such as those found in Incropera and DeWitt (2002).

$$q_{\text{cond}} = -k_S 4\pi r_p^2 \left(\frac{dT}{dr} \right)_s \quad (38)$$

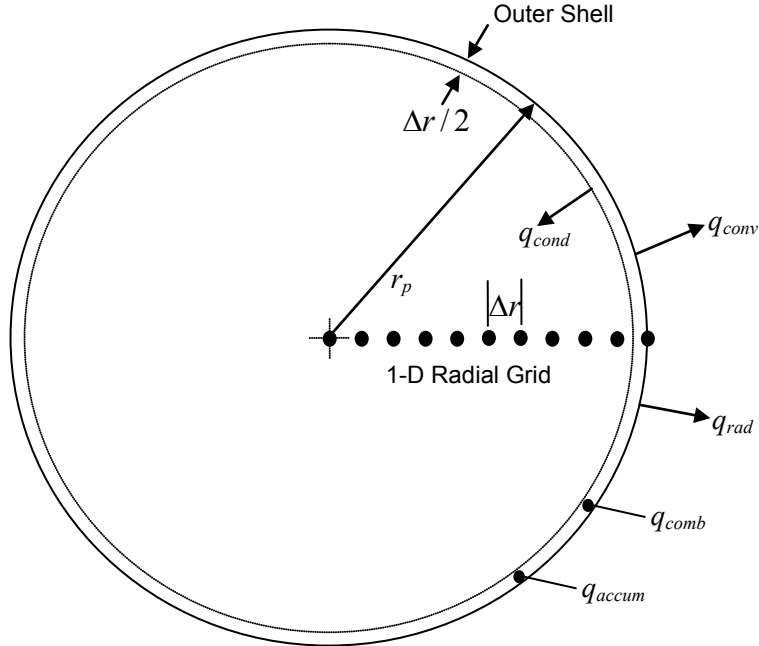


Figure 3.—Particle heat transfer and reaction model.

$$q_{rad} = -\varepsilon_{rad} \sigma_{S-B} 4\pi r_p^2 (T_p^4 - T_{wall}^4) \quad (39)$$

$$q_{conv} = -h_p 4\pi r_p^2 (T_g - T_p) \quad (40)$$

where

$$h_p = \frac{\text{Nu}_d k_g}{2r_p} \quad (41)$$

As with the drag coefficient, a number of empirical expressions for the Nusselt number have been developed for spheres over a variety of flow conditions, characterized by the Mach number and the Reynolds number. Once again, an expression that covers a wide range of these parameters is necessary for this study, including the case of supersonic relative velocity. In the case of supersonic relative velocity, the effect of the shock wave in front of the particle needs to be considered. Drake and Backer (1952) determined that it is best to correlate the Nusselt number with the conditions immediately behind the shock wave in line with the direction of travel. Since this is essentially a standing normal shock, simple textbook relations, such as those found in Saad (1985), can be used to calculate the pressure, temperature, and density behind the shock wave. After adjusting the thermodynamic and transport properties to the post-shock conditions, the post-shock Mach and Reynolds numbers can be calculated, and an appropriate correlation, such as that proposed by Fox, et al.(1977), given below, can be used.

$$\text{Nu}_d = 2 \left[\frac{e^{-M_{rel}}}{1 + 17 \frac{M_{rel}}{\text{Re}_{rel}}} \right] + 0.459 \text{Pr}^{0.33} \text{Re}_{rel}^{0.55} \left[\frac{1 + 0.5e^{\frac{-17M_{rel}}{\text{Re}_{rel}}}}{1.5} \right] \quad (42)$$

For high speed flows, it is also necessary to calculate what is commonly referred to as the recovery temperature (White, 1988), given below for laminar flow.

$$T_{rec} = T_{gas} \left(1 + \text{Pr}^{0.5} \left(\frac{\gamma - 1}{2} \right) M_{rel}^2 \right) \quad (43)$$

This value is then substituted into the convection heat transfer Equation (40), in place of the free stream gas temperature, to determine the convective heat transfer term.

$$q_{conv} = -h_p 4\pi r_p^2 (T_{rec} - T_p) \quad (44)$$

The recovery temperature is a modified form of the total temperature which approximates the temperature in the boundary layer surrounding the particle. This temperature is based on the free stream temperature and free stream relative Mach number, even in the case of a supersonic relative Mach number.

The calculation of the combustion heat addition term, q_{comb} , is not nearly so straight forward. A number of carbon particle combustion models have been developed, such as those of Blake (2002); Hurt, et al. (1998); Lee, et al. (1995); Makino and Law (1986); and Libby (1980). These models were typically developed to examine the oxidation of coal char. In addition to simplifications such as zero gas-particle velocity slip and uniform particle temperature, each of these studies was limited to combustion at lower pressures; typically atmospheric pressure. However, for the problem under consideration in this study, a large range of pressures must be considered. Only two studies were found that looked at carbon

combustion at pressures considerably above atmospheric pressure in a convective flow, those of Moors (1998) and Hong (2000). The methodology of Hong was adopted for this study.

Calculation of the combustion rate for solid carbon is somewhat complicated by the fact that the products of reaction shift as a function of the reaction temperature. As the carbon surface temperature increases, the reaction shifts from



to



Hong provides the following Arrhenius-type relation, taken from Hurt and Mitchell (1992), for the mole ratio of CO to CO₂.

$$MR = \frac{\text{moles}_{CO}}{\text{moles}_{CO_2}} = 40000e^{\frac{-30000}{1.987T_s}} \quad (47)$$

For convenience, this relation can be recast to give the ratio of moles of CO₂ produced by the surface reaction to the total moles produced.

$$\psi = \frac{1}{1 + MR} \quad (48)$$

Two other convenient parameters can be defined at this point that will be useful for simplifying the particle combustion equations. These are the stoichiometric coefficient of oxygen consumed for each mole of carbon consumed, v₀, and an intermediate variable, ξ.

$$v_0 = 0.5(1 + \psi) \quad (49)$$

$$\xi = \frac{\psi - 1}{\psi + 1} \quad (50)$$

Calculation of the combustion rate for a solid carbon particle is also complicated by the structure of the particle itself. For a typical carbon particle, the majority of the reactive surface area is made up of a labyrinth of micron to nanometer diameter pores internal to the particle. Oxygen must diffuse from the surface into the particle pore structure for significant reaction to take place. This process must be included in order to develop an accurate reaction rate model. This internal diffusion effect is captured through the use of an effectiveness factor, η, defined by Hong as the ratio of the actual observed reaction rate including intra-particle diffusion effects to what the reaction rate would be if the oxygen concentration at the particle surface persisted throughout the interior pore structure of the particle. The effectiveness factor is calculated as follows.

$$\eta = f_c \frac{1}{M_T} \left[\frac{1}{\tanh(3M_T)} - \frac{1}{3M_T} \right] \quad (51)$$

where

$$f_c = \left(1 + \frac{\sqrt{1/2}}{\frac{1}{2M_T^2} + 2M_T^2} \right)^{\frac{1}{2}(1-m_{obs})^2} \quad (52)$$

The Thiele Modulus, M_T , is defined as

$$M_T = \frac{r_p}{3} \left[\frac{v_0 k_{1p} R_u \left(T_g / D_e \right)}{2K_p P_{O_2,s} + \frac{1}{1 + K_p P_{O_2,s}}} \right]^{\frac{1}{2}} \quad (53)$$

and the observed reaction order, m_{obs} , is

$$m_{obs} = \frac{1}{1 + K_p P_{O_2,s}} \quad (54)$$

The above expressions contain two kinetic rates for which Hong gives the following Arrhenius-type relations for non-porous graphite flakes, based on the experimental data of Ranish and Walker (1993).

$$k_{1p} = 6.29 \times 10^8 e^{\frac{-51000}{R_u T_{p,i}}} \quad (55)$$

$$K_p = 13.4 e^{\frac{-10100}{R_u T_{p,i}}} \quad (56)$$

The constants contained in these kinetic rate expressions must be re-derived from experimental data for each individual type of graphite or coal char, as they are dependent upon the physical structure of the particles as well as their chemical composition.

The Thiele Modulus expression also requires a value for the effective diffusion coefficient, D_e . The effective diffusion coefficient is a function of the particle porosity, ϵ (1.0 minus the ratio of the actual particle density to the density of a non-porous solid of the same material), the molecular diffusion coefficient of oxygen into the gas mixture at the local gas conditions, $D_{O_2,M}$, and the Knudsen diffusion coefficient, D_k (for diffusion in small pores where wall collisions dominate over inter-molecular collisions). Hong gives the following relation for the combination,

$$D_e = \frac{\epsilon^2}{\frac{1}{D_{O_2,M}} + \frac{1}{D_k}} \quad (57)$$

where

$$D_k = 9700 r_p \left(\frac{T_{p,i}}{M_{O_2}} \right)^{\frac{1}{2}} \quad (58)$$

in units of cm^2/s , as taken from Smith (1981). The value of $D_{O_2,M}$ is available from the gas-phase portion of the Q1D code.

In the formulation of Hong, a uniform particle temperature was assumed, so a single value of the effectiveness factor was used. In this study, it was necessary to use an approach that accounted for an internal particle temperature distribution in what is otherwise a global reaction model. The use of a mass averaged value of the effectiveness factor, equivalent to an internal surface area averaged value, was selected as an appropriate modeling approach. While no data was available to validate this modeling choice, this commonly used approach provides reasonable approximate values and reduces to the approach of Hong in the case of uniform particle temperature. The general behavior of the effectiveness factor as a function of temperature is shown in Figure 4, using the kinetic parameters for graphite flakes given above.

In order to solve this complex system for the carbon burning rate, it is necessary to know both the overall particle oxygen consumption rate and the particle temperature profile. However, these values are inter-dependent, therefore requiring that the carbon burning rate be solved iteratively. Since the other heat flow terms from Equations (38), (39), and (44) depend on the particle surface temperature, and therefore the particle temperature profile, the energy balance given in Equation (37) must also be solved iteratively. This is done by running an inner iterative loop that corrects the particle surface partial pressure of oxygen (at the particle surface temperature supplied from an outer iterative loop) by comparing the O_2 diffusion rate from the free stream and the total carbon consumption rate of the particle based on the graphite kinetics, taking into account the temperature dependent stoichiometric coefficients described above (Eqs. (45) to (47)). An outer iterative loop is run that corrects the particle surface temperature by comparing the outer shell carbon consumption rate calculated by an energy balance on the outer shell to the same rate calculated using the carbon consumption kinetic expression using the updated particle surface partial pressure of oxygen from the inner loop.

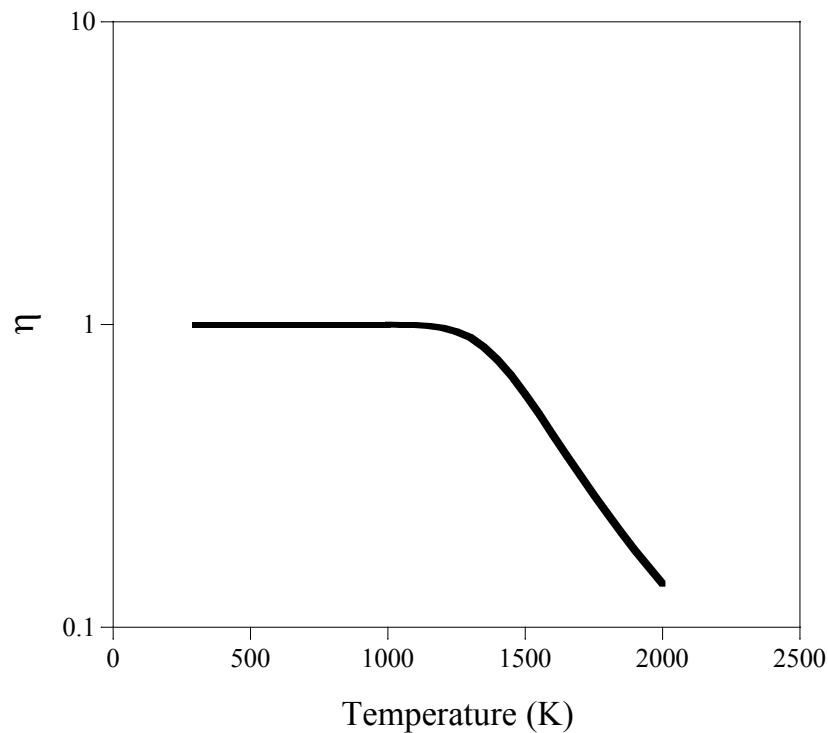


Figure 4.—Effectiveness factor as a function of temperature.

The procedure for this solution is as follows

1. Assume a value for the particle surface temperature. This is typically selected as the value from the previous time step.
2. Assume a value for the oxygen concentration at the particle surface. A value of 90 percent of the free stream oxygen concentration is used to start each iterative cycle.
3. Calculate the global kinetic carbon consumption rate, r_k , for the given values of the particle surface temperature, the particle interior temperature distribution, and the surface oxygen concentration. An intrinsic Langmuir expression is used to calculate the local volumetric consumption rate within each shell of the particle. This expression, adapted from Hong, is valid over a wide range pressures, temperatures and porosities.

$$r_{k,i} = \left\{ \eta_{avg} + \frac{S_{ext}}{S_{int}} \right\} \frac{S_{int}}{S_{tot}} \frac{k_{1p,i} P_{O_2,S} M_c}{1 + K_{p,i} P_{O_2,S}} \quad (59)$$

The natural units for this expression is g/cm³-s, based on the particle volume, but it is typically given in terms of the particle external surface area, g/cm²-s. This transformation is easily done by multiplying the rate by the particle volume and then dividing by the external surface area. In either case, the units of k_{1p} and K_p are mole/cm³-atm-s and 1/atm, respectively. The kinetic rates in Equation (59), k_{1p} and K_p , are the same terms used in the Thiele Modulus expression. The interior, exterior, and total particle surface areas, S_{int} , S_{ext} , and S_{tot} , are used in the expression to proportion the amount of reaction that takes place on the particle exterior, and is therefore not affected by internal pore diffusion, versus that which occurs in the particle interior. It should be noted that the external surface area, S_{ext} , is typically taken as the particle's geometric external area multiplied by a roughness factor to account for surface irregularities. Hong suggests a value of 5 be used for the roughness factor. Using available data for porosity and pore diameter, and assuming a monodisperse pore size distribution within the particle, the particle interior surface area is readily calculated.

$$S_{int} = \frac{16\pi\epsilon r_p^3}{d_{pore}} \quad (60)$$

The local carbon consumption rate for each particle shell volume is calculated by multiplying $r_{k,i}$ by the volume of the particle shell being evaluated. The global carbon consumption rate is then obtained by summing the individual shell rates. This value is then normalized by the particle's geometric external surface area, so as to be comparable to the other rates used in the iterative procedure, which are expressed per unit external surface area.

4. Next, the rate of carbon consumption based on diffusion of O₂ from the free stream to the particle surface must be calculated. The mass transfer coefficient for O₂ diffusing to the surface, recast in terms of carbon consumption, can be expressed as,

$$K_D = \frac{M_C D_{O_2,m} Sh}{2r_p R_u T_{film} v_o} \quad (61)$$

where

$$T_{film} = 0.5(T_p + T_g) \quad (62)$$

and where Sh is the Sherwood number, which is calculated from Equation (42) by substituting the Schmidt number for Prandtl number. A Schmidt number of 0.74 is used for this study. Then the rate of carbon consumption based on oxygen diffusion to the surface is given by,

$$r_{OX} = \frac{K_D P}{\xi} \ln \left\{ \frac{1 - \xi \frac{P_{O_2,s}}{P}}{1 - \xi \frac{P_{O_2,f_s}}{P}} \right\} \quad (\xi \neq 0) \quad (63)$$

or

$$r_{OX} = K_D (P_{O_2,f_s} - P_{O_2,s}) \quad (\xi = 0) \quad (64)$$

with the pressure terms in the above expressions given in atmospheres.

Assuming that the reaction and diffusion processes are in a quasi-steady state, the carbon consumption rate from Equation (63) or (64) and the rate of carbon consumption calculated from the kinetic expressions above should be equal. If they are not initially equal, the surface partial pressure of O₂, $P_{O_2,s}$, is iterated upon to bring these two rates into equilibrium.

5. The carbon consumption-based O₂ diffusion and O₂ consumption rates are now in equilibrium at the particle surface temperature assumed in step 1. An energy balance of the particle shell using the terms shown in Figure 3 is then used to adjust the particle surface temperature as follows. First, (37) is rearranged to solve for q_{comb} .

$$q_{comb} = q_{accum} + q_{rad} + q_{conv} + q_{cond} \quad (65)$$

where

$$q_{accum} = \frac{4\pi\rho_s}{3} \left(r_p^3 - \left(r_p - \frac{\Delta r}{2} \right)^3 \right) C_s (T_p^{i+1} - T_p^i). \quad (66)$$

Then we can write a carbon consumption rate expression for the outer shell based on the rate that would be required to produce q_{comb} .

$$r_e = \frac{q_{comb}}{(1-\psi)\Delta H_{CO} + \psi\Delta H_{CO_2}} \quad (67)$$

If r_e is not equal to the kinetic rate for the outer shell calculated using Equation (59) within a given convergence criteria, T_p is adjusted upward or downward, as appropriate, and the procedure is repeated starting at step 2 until convergence is achieved.

Now that the carbon consumption rate and particle outer shell energy balance have been calculated, the next step is to update the particle mass to account for the mass lost due to the interior and exterior surface reactions. Mass can be lost from both the exterior surface of the particle, reducing the particle diameter, and from the pore surfaces internal to the particle, increasing the diameter of the pores. To simplify the analysis for this study, it was decided to adjust the particle mass by increasing the pore diameter within the particle. This approach was selected because of the high porosity of the graphite material being studied and the difficulty in establishing a proper mass decrease to diameter decrease ratio.

According to Hong, the relationship between mass decrease and particle diameter is generally determined experimentally, and this ratio changes during the combustion history of a particle and with ambient conditions. By changing the pore diameter only, a computational efficiency is obtained in that the particle grid does not have to be adjusted after each iteration.

Once this has been done, the source terms for overall mass, momentum (including the momentum associated with the mass lost by the particle), energy, and species (CO , CO_2 , and O_2) are calculated for use in Equations (1), (2), (3), and (6). These source terms are multiplied by the number of particles in each particle set, and then linearly interpolated onto the two adjacent grid points for use in the gas phase governing equations.

Lastly, the internal particle temperature profile is updated using the transient, 1-D conduction equation in radial coordinates.

$$\frac{1}{r^2} \frac{\partial}{\partial r} \left(K_s r^2 \frac{\partial T}{\partial r} \right) = \rho_s C_s \frac{\partial T}{\partial t} \quad (68)$$

The simple, 2nd-order accurate Crank-Nicolson semi-implicit method (Tannehill, et al., 1997) is used to solve the conduction equation. This method was selected because it is unconditionally stable and does not limit the time step used in the overall calculation.

2.7 Gas Phase Numerical Solution Method

The gas-phase governing equations (Eqs. (1), (2), (3), and (6)) are cast in the following form for solution

$$\frac{\partial U}{\partial t} = -\frac{\partial F}{\partial x} + J \quad (69)$$

where

$$U = \begin{Bmatrix} \rho_g A\phi \\ \rho_g A\phi u_g \\ \rho_g A\phi e_g \\ \rho_g A\phi Y_i \end{Bmatrix} \quad (70)$$

$$F = \begin{Bmatrix} \rho_g A\phi u_g \\ PA\phi + \rho_g A\phi u_g^2 \\ q_c A\phi + Pu_g A\phi + \rho_g A\phi u_g e_g \\ \rho_g A\phi(u_g + v_i) Y_i \end{Bmatrix} \quad (71)$$

and

$$J = \begin{Bmatrix} A\phi D_m \\ A\phi D_p + P\phi \left(\frac{\partial A}{\partial x} \right) \\ A\phi D_e - q_w \sqrt{4A\pi} \\ A\phi D_{m,i} \end{Bmatrix} \quad (72)$$

Two different schemes are available in the code for solving this set of equations. The first scheme is the standard MacCormack predictor-corrector scheme, as described in Anderson (1995). This solution method is 2nd order accurate in space and time, and follows the following steps.

Predictor Step

1. The values in the F and J arrays are first calculated from the values contained in the U array from the previous time step.
2. Equation (69) is then used to obtain the time derivative of the U array using a forward difference in x .
3. The U array is then updated to an interim value by the equation,

$$\bar{U} = U^j + \left(\frac{\partial U}{\partial t} \right) \Delta t + \chi \quad (73)$$

where j refers to the time step and χ is a Total Variation Diminishing (TVD) artificial viscosity term that will be discussed later.

Corrector Step

1. The values in the F and J arrays are updated from values contained in the \bar{U} array.
2. Equation (69) is again used to obtain the time derivative of the \bar{U} vector using a backward difference in x .
3. An average of the two time derivatives is calculated as follows,

$$\left(\frac{\partial U}{\partial t} \right)_{avg} = \frac{1}{2} \left[\left(\frac{\partial U}{\partial t} \right) + \left(\frac{\partial \bar{U}}{\partial t} \right) \right] \quad (74)$$

4. Lastly, the U array is updated to the next time step by the following expression,

$$U^{j+1} = U^j + \left(\frac{\partial U}{\partial t} \right)_{avg} \Delta t + \bar{\chi} \quad (75)$$

This scheme can be easily improved to 4th order accuracy in space by making the following substitutions (Georgiadis 2000), with k representing the spatial grid coordinate.

1. Calculate the time derivative of U from predictor step 2 by the expression,

$$\frac{\partial U}{\partial t} = -\frac{1}{6\Delta x} (-7F_k + 8F_{k+1} - F_{k+2}) + J \quad (76)$$

2. Calculate the time derivative of \bar{U} from corrector step 2 by the expression,

$$\frac{\partial \bar{U}}{\partial t} = -\frac{1}{6\Delta x} (7\bar{F}_k - 8\bar{F}_{k-1} + \bar{F}_{k-2}) + \bar{J} \quad (77)$$

The user can select either scheme within the code.

Numerical viscosity, χ , which is generally required when using a MacCormack type scheme (Anderson 1995), is combined with a TVD routine in an easily implemented method developed by Davis (1987). The basic form of the TVD artificial viscosity term is

$$\begin{aligned}\chi = & \left[K^+_{k+\frac{1}{2}} \left(r^+_{k+\frac{1}{2}} \right) + K^-_{k-\frac{1}{2}} \left(r^-_{k-\frac{1}{2}} \right) \right] \left(U_{k+1} - U_k \right) - \\ & \left[K^+_{k-\frac{1}{2}} \left(r^+_{k-\frac{1}{2}} \right) + K^-_{k+\frac{1}{2}} \left(r^-_{k+\frac{1}{2}} \right) \right] \left(U_k - U_{k-1} \right)\end{aligned}\quad (78)$$

where

$$K^\pm(r^\pm) = 0.5C(v_c) \{ 1 - \theta(r^\pm) \} \quad (79)$$

The leading variable in this expression is defined as

$$C(v_c) = \begin{cases} v_c(1-v_c) & \text{if } v_c \leq 0.5 \\ 0.25 & \text{if } v_c > 0.5 \end{cases} \quad (80)$$

where the Courant number, v_c , is defined by

$$v_c = \max |\lambda_k| \frac{\Delta t}{\Delta x} \quad (81)$$

and the eigenvalue at each point is defined as

$$\lambda_k = \sqrt{|u_{g,k} + a_k|} \quad (82)$$

The expression for the flux limiter $\theta(r^\pm)$ is given by

$$\theta(r^\pm) = \begin{cases} \min(2r^\pm, 1) & \text{if } r^\pm > 0 \\ 0 & \text{if } r^\pm < 0 \end{cases} \quad (83)$$

where r^+ and r^- are defined by the following inner products,

$$r_i^+ = \frac{\left(\Delta U_{k-\frac{1}{2}}, \Delta U_{k+\frac{1}{2}} \right)}{\left(\Delta U_{k+\frac{1}{2}}, \Delta U_{k+\frac{1}{2}} \right)} \quad (84)$$

$$r_i^- = \frac{\left(\Delta U_{k-\frac{1}{2}}, \Delta U_{k-\frac{1}{2}} \right)}{\left(\Delta U_{k-\frac{1}{2}}, \Delta U_{k-\frac{1}{2}} \right)} \quad (85)$$

and ΔU represents a backward difference in x .

The gas-phase solution method also requires boundary conditions. These boundary condition may need to represent subsonic, choked, or supersonic flows, depending on the simulation. For supersonic and choked inflow conditions, the velocity or Mach number is set along with either the static or total pressure

and temperature. For supersonic and choked outflow conditions, simple extrapolated boundary conditions are used. Subsonic boundary conditions are inherently more challenging, since information can travel both upstream and downstream. The methodology of characteristic boundary conditions of Poinsot and Lele (1992), valid for both the Euler equations as well as the Navier-Stokes equations, has been adopted for these conditions. The boundary condition can be pre-defined, or can be selected by the code as a function of the flow conditions as the calculation progresses.

The computational grid used for these calculations is generally uniform in the axial coordinate x , with grid spacings ranging from approximately 4 mm down to 1 mm. Since the calculations are quasi-1D, the number of grid points required for any given calculation is typically reasonable, from 300 up to 4000. Departures from a uniform grid are pointed out where they occur.

The time step used in these calculations was allowed to vary during the course of the computation to the largest value that did not exceed any of three limits put in place to ensure stability and accuracy of the solution. The first limit is the standard Courant, Friedrichs, and Lewy (CFL) stability limit for explicit numerical methods (Tannehill, et al., 1997). A time step limit of 50 percent of the maximum time step allowed by the CFL criterion was used to ensure stability. A gas-phase chemical reaction rate limit to the time step was also found to be necessary to prevent a chemical heat release “runaway” under some conditions. A limit of 1 percent change to any species mass fraction at any grid point was typically used. Lastly, it was found during validation testing of the code that a time step limit based on the rate of change of the outer shell temperature of the particles was necessary to maintain accuracy. This limit was typically set to 0.02 K temperature change in the outer shell of any particle. The smallest of these three limits is selected at each time step as the value to be used for the succeeding time step.

3.0 Validation

For the purposes of validating the above described Q1D 2-phase code, no single representative test case of known solution was found. Instead, different aspects of the code were validated individually using available solutions. Individual physical process validations were performed in addition to the higher-level validations included in these sections. These physical process validations included chemical equilibrium calculations, shock tube calculations, individual particle fixed outer temperature boundary condition calculations, individual particle constant heat flux calculations, rocket performance calculations, steady state nozzle flow calculations, and various carbon combustion calculations. Additionally, many test cases were run to determine maximum acceptable time steps and grid sizes and to determine appropriate convergence criteria for a wide range of problems.

3.1 Gas Phase Flow and Chemical Kinetics Validation

As a first step, the gas-phase reacting flow capability was validated using a 1-D detonation simulation. The full kinetic mechanism was exercised by using a reactant mixture of 10 percent CO, 3 percent H₂, 32 percent O₂ and 55 percent N₂ by mass. As shown in Figure 5, the detonation was initiated by a small region of high pressure, high temperature H₂ at the closed end of a tube filled with reactants at 300 K and 100 kPa. The ignition region is initially at 3000 K and 4 MPa. The detonation wave stabilized after traversing the first 7 mm of the computational domain, so the calculation was terminated at that point. A time step of approximately 1.5×10^{-10} s was used.

These results were then compared to a calculation obtained from the 1-dimensional ZND code developed by Shepherd (1986). To run the ZND code, the desired kinetic mechanism is first input into the CHEMKIN code, described by Kee et al. (1993), that provides the kinetic and thermodynamic properties required. Next, the Gordon and McBride (1994) CEA code, or any other equilibrium detonation code, is used to determine the detonation (Chapman-Jouguet) velocity. With these inputs, ZND calculates the 1-D detonation structure by first assuming a normal shock based on the detonation velocity and quiescent reactant conditions and then reacts the mixture via the kinetic mechanism and gas properties from CHEMKIN using the post-shock conditions as the reaction initial conditions. ZND performs these

calculations in the reference frame fixed to the detonation wave, shown in Figure 6, so the velocity must be transformed back to the stationary reference frame by adding the detonation wave velocity. All of the static properties are unaffected by the change in reference frames.

Figure 7 shows the convergence of the detonation wave speed upon the equilibrium value calculated using the CEA code. The wave speed at the termination of the calculation is approximately 1 percent below the CEA value, which was judged to be sufficiently converged for the purposes of this validation.

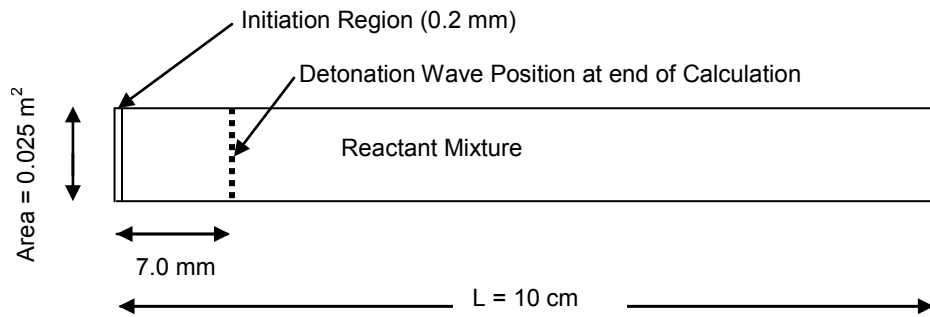


Figure 5.—Detonation case geometry.

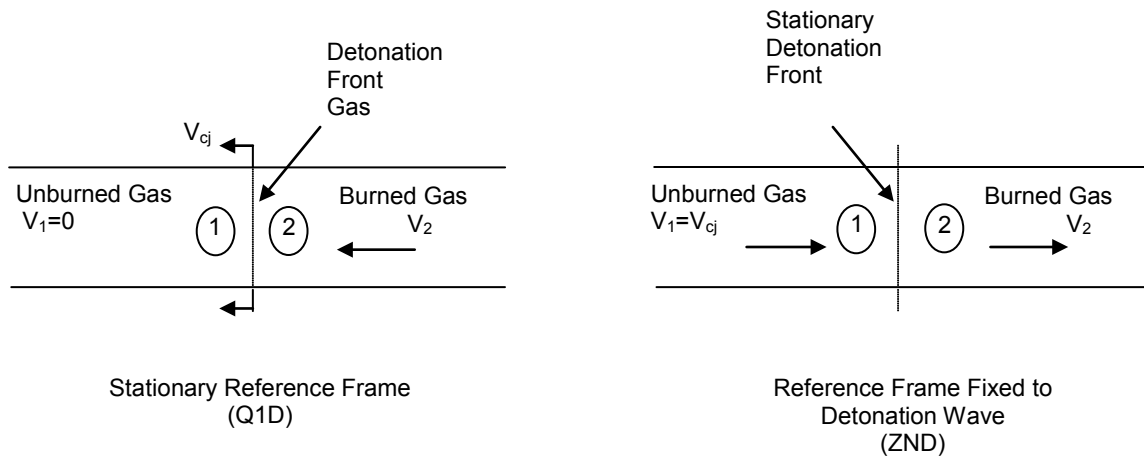


Figure 6.—Detonation calculation reference frames.

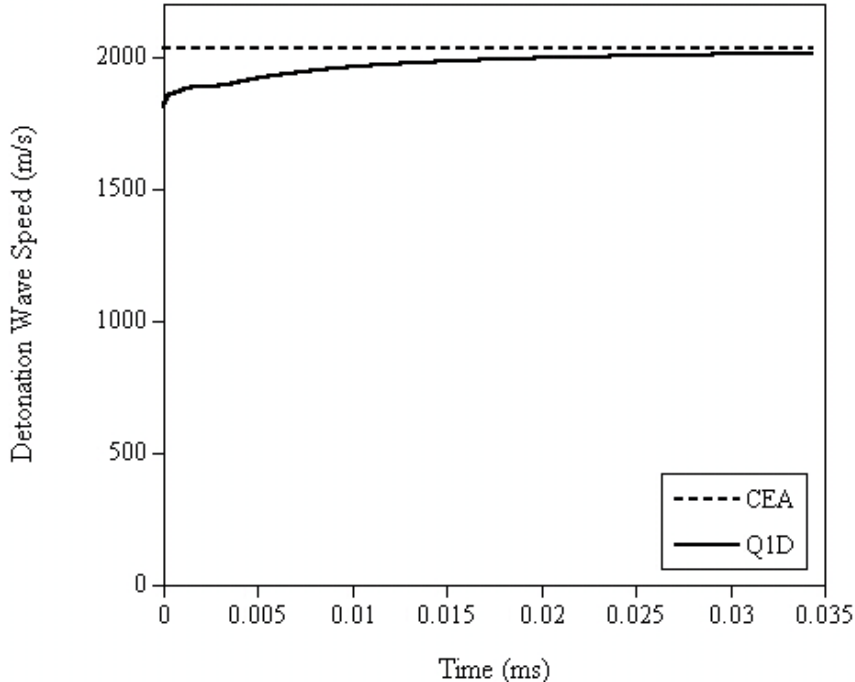


Figure 7.—Detonation wave speed convergence.

Figures 8 to 15 show the values of pressure, temperature, velocity, and H₂O, OH, CO₂, NO, and NO₂ mass fractions calculated by Q1D at the end of the computation against those calculated by ZND using the same kinetic mechanism given in Appendix B. Since the results from ZND begin after the leading shock wave of the detonation front and therefore do not include part of the induction zone, leading to a difference in total induction time between the two codes, the two sets of results were aligned by matching the midpoints of the initial temperature rise region of the temperature profiles shown in Figure 9. Once the results were thus synchronized, the ZND and Q1D results generally agree quite well. The largest differences are observed in the region of the shock, particularly noticeable in the pressure and velocity profiles. This is caused by the chemical reactions and consequent heat release initiating within the shock wave in the Q1D model, whereas in the ZND model, it is assumed that the chemical induction time starts after the passing of the shock wave, as mentioned above. This difference in the time at which reactions start is evident in the H₂O, OH, and CO₂ profiles. The nitrogen reactions are somewhat slower, and therefore do not reflect this difference as significantly. The quicker rise in NO concentration shown in Figure 14 for the Q1D code is most likely due to differences in the thermodynamic and transport property data sets used by the two codes. Overall, the good agreement between these two results for the detonation case indicates that the gas phase fluid dynamic and kinetic models and solvers within the Q1D code are working properly.

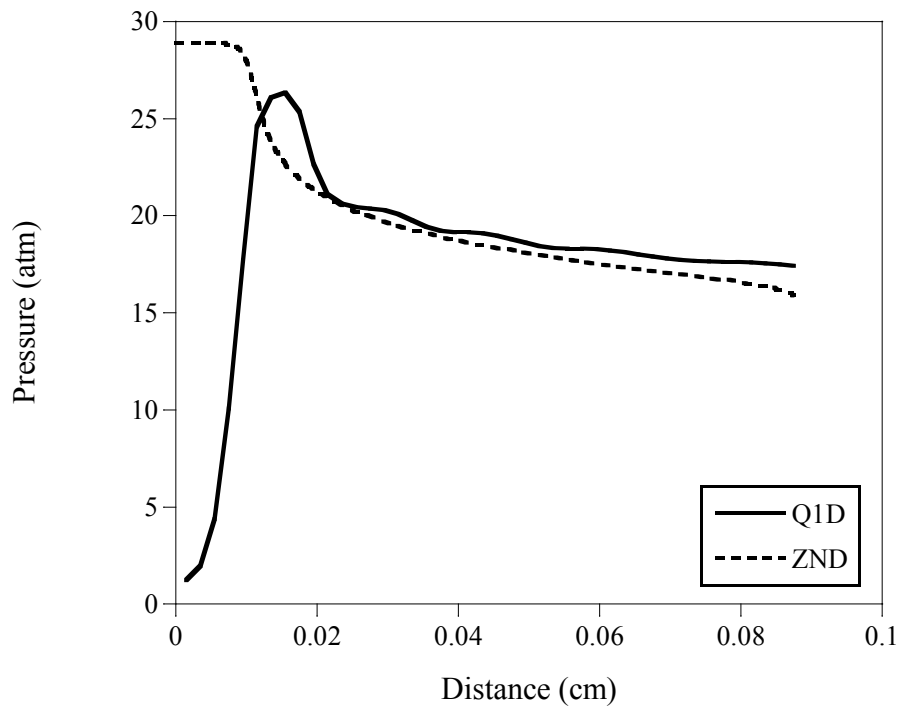


Figure 8.—Comparison of pressure profiles between Q1D and ZND codes.

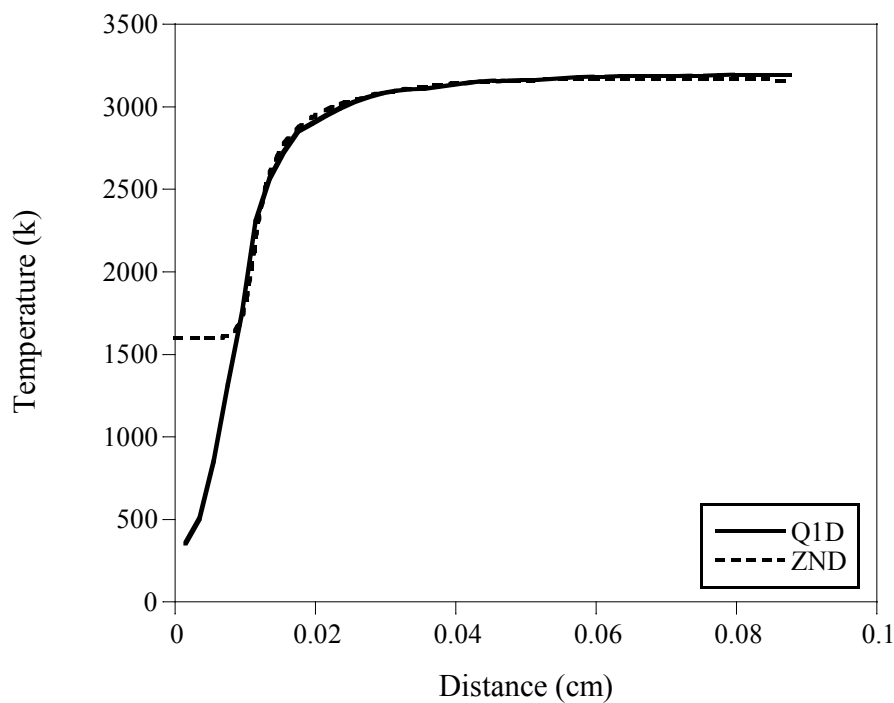


Figure 9.—Comparison of temperature profiles between Q1D and ZND codes.

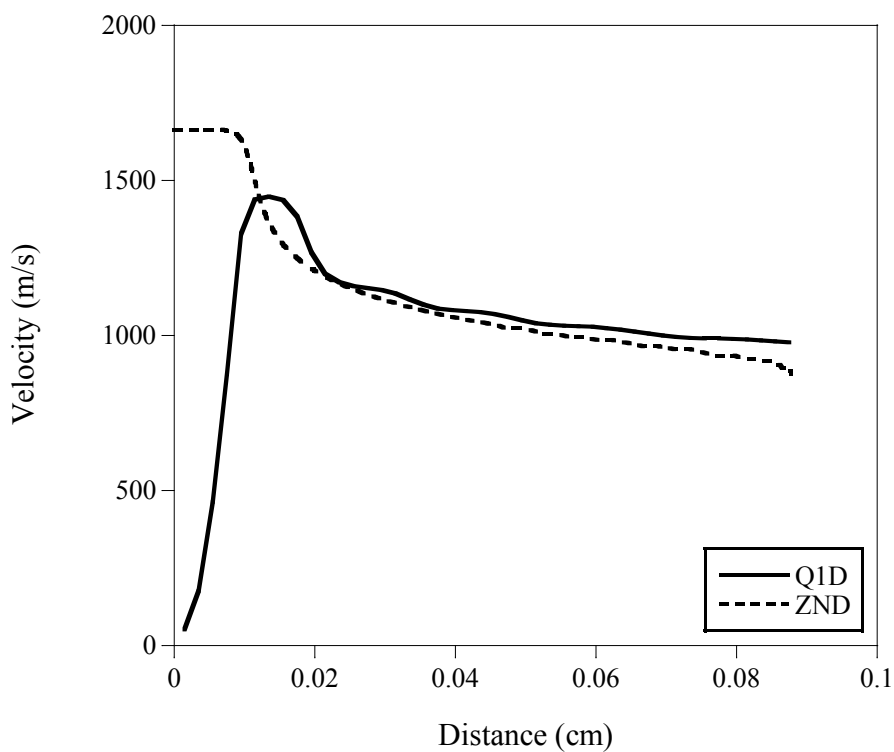


Figure 10.—Comparison of velocity profiles between Q1D and ZND codes.

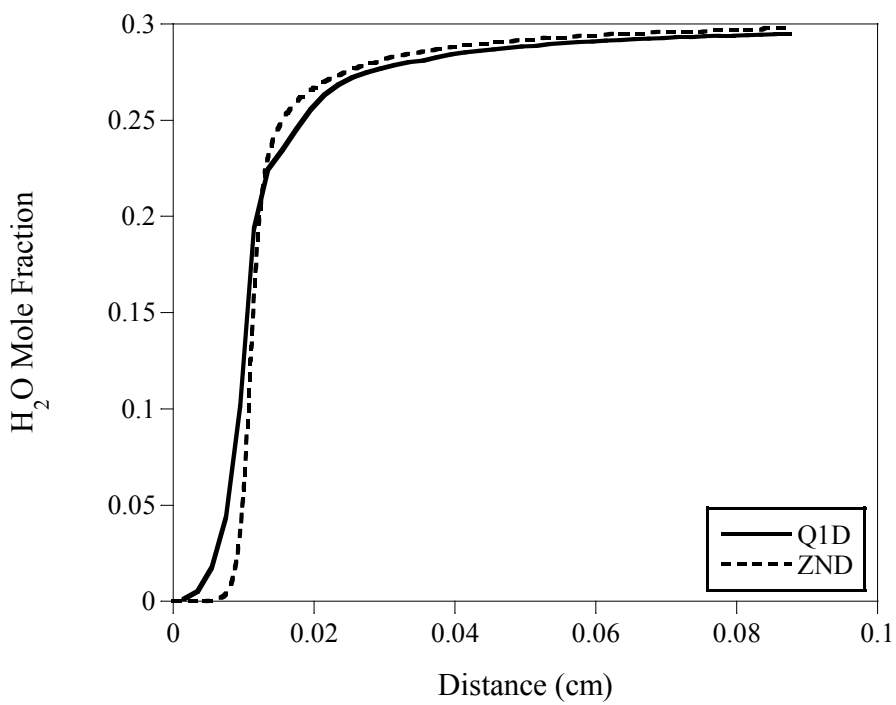


Figure 11.—Comparison of H₂O mole fraction profiles between Q1D and ZND codes.

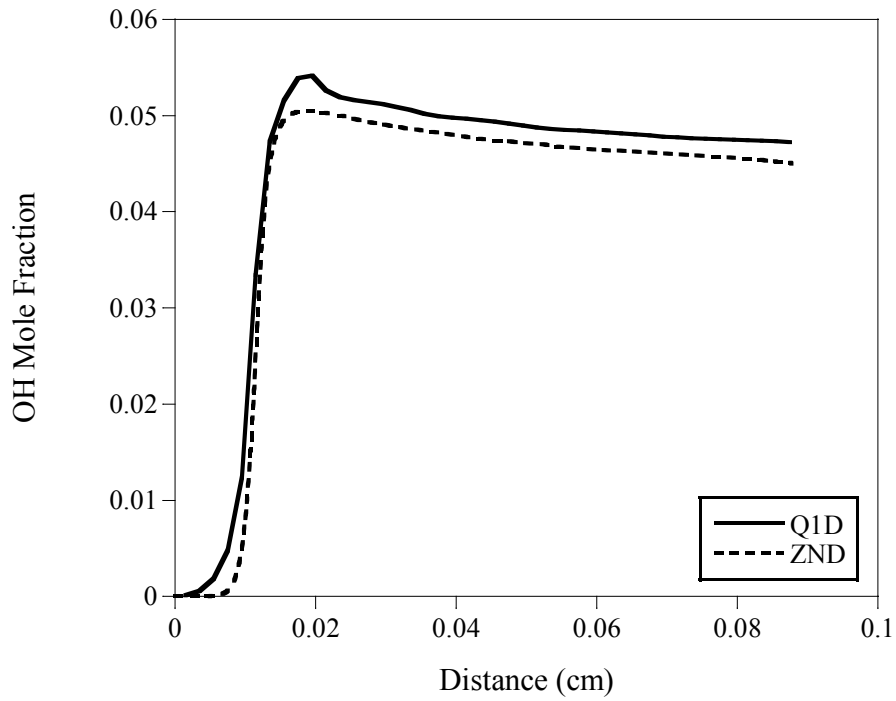


Figure 12.—Comparison of detonation OH mole fraction profiles between Q1D and ZND codes.

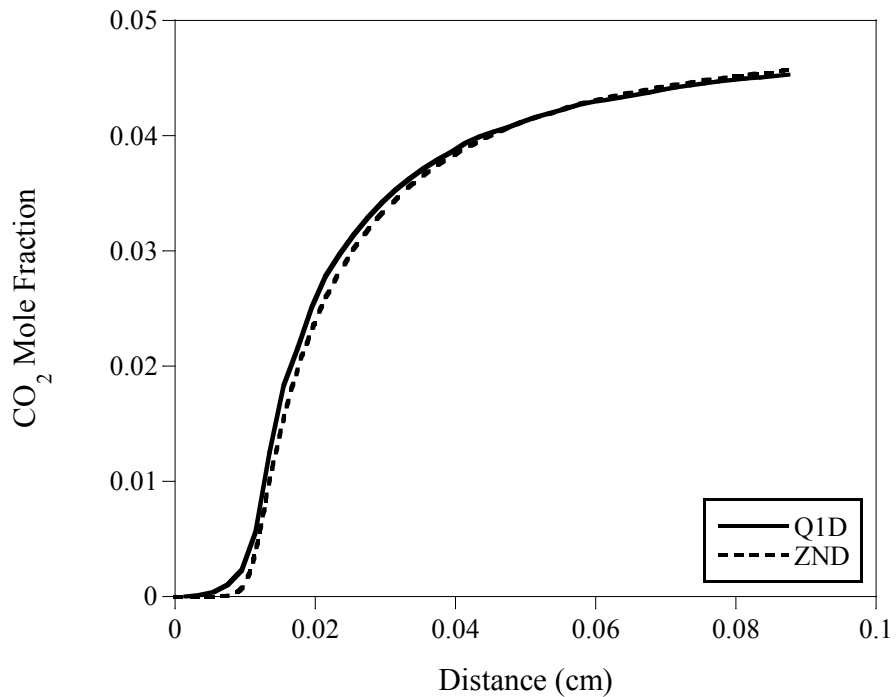


Figure 13.—Comparison of detonation CO₂ mole fraction profiles between Q1D and ZND codes.

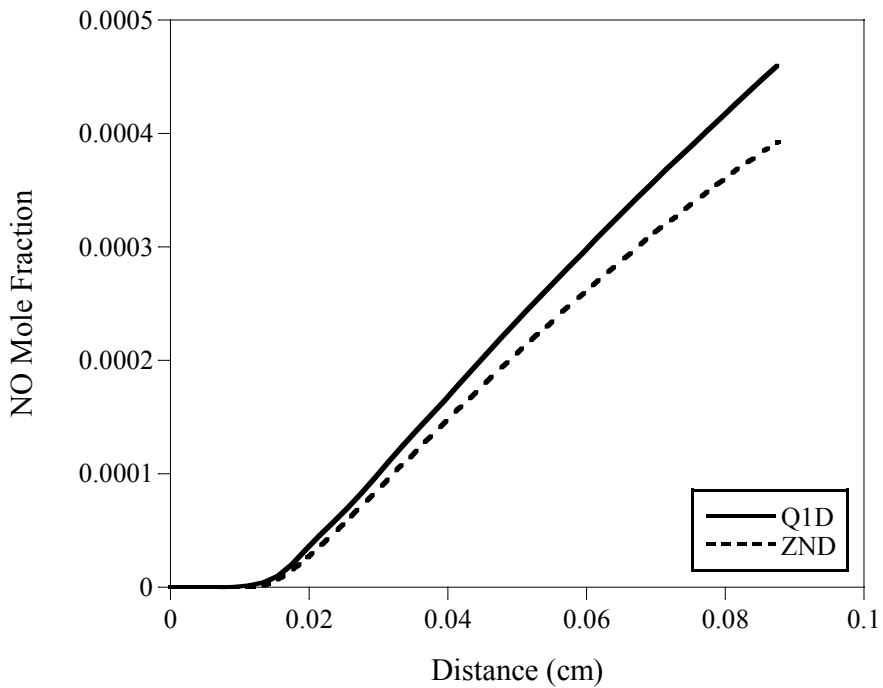


Figure 14.—Comparison of detonation NO mole fraction profiles between Q1D and ZND codes.

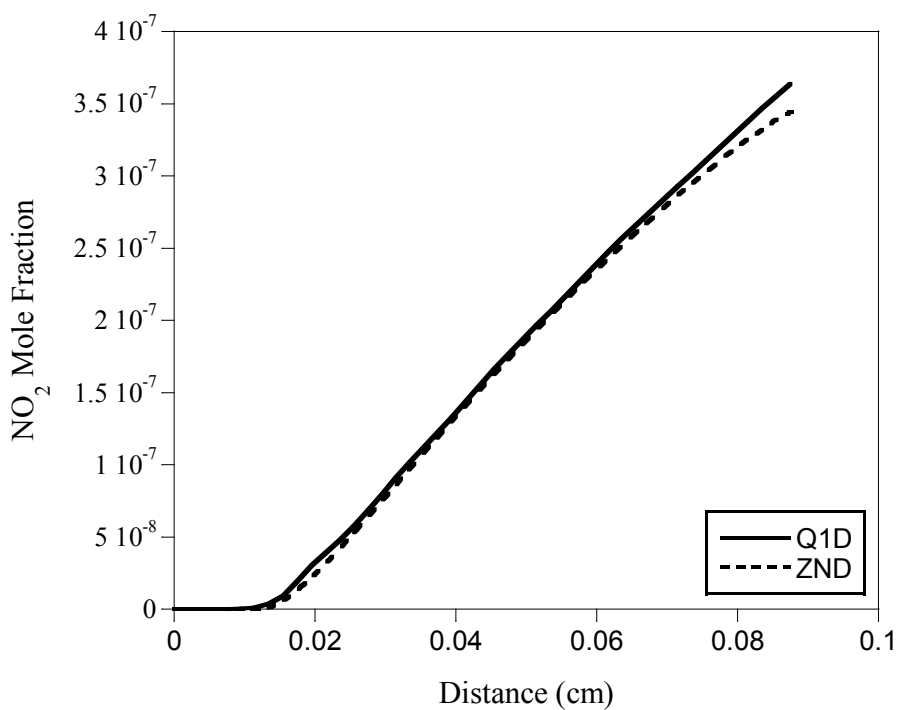


Figure 15.—Comparison of detonation NO₂ mole fraction profiles between Q1D and ZND codes.

3.2 Particle Drag and Heat Transfer Models and Gas-Solid Momentum and Heat Exchange Models Validation

The next step in validating the Q1D code is to verify that the particle momentum exchange and convective heat transfer models are working properly. This can be accomplished by studying a gas flow interaction with chemically inert particles. Maxwell and Seasholtz (1974) examined the behavior of micron-size inert particles passing through a Mach 1.6 normal shock wave for the purposes of determining the tracking behavior of these particles used in Laser Doppler Velocimetry (LDV). The physical situation modeled in the study was that of a constant area duct with a supersonic, 289 K static temperature, 1 atmosphere static pressure, particle laden inlet air flow and a standing normal shock wave interior to the duct. The particles were assumed to be at the gas static temperature and velocity up to the shock wave, and to occupy negligible volume. For the analysis, the post-shock conditions, as calculated using the standard Hugoniot relations, were used as the initial conditions for the gas, while the pre-shock temperature and velocity were used as the initial conditions for the particles. Since only small particles, less than 5 μm diameter, were considered for this study, uniform particle temperature was assumed throughout. Variations in particle diameter, particle density, gas and particle inflow velocity, particle specific heat and particle/gas mass loading ratio were examined. Constant thermodynamic and transport properties were assumed for the air and the particles, but the exact values were not given. Because of this, the calculations had to be replicated using the following equations adapted from Maxwell and Seasholtz (1974), as the values assigned for the thermodynamic and transport properties can significantly affect the results.

A force balance on an individual particle yields the following relation,

$$\frac{\partial u_p}{\partial x} = \frac{3}{8} \left(\frac{C_D}{r_p u_p} \right) \left(\frac{\rho_g}{\rho_p} \right) |u_g - u_p| (u_g - u_p) \quad (86)$$

where the absolute value of the gas-particle velocity difference is used as shown to maintain the correct sign for the particle velocity spatial derivative. Likewise, an energy balance on an individual particle yields the following equation,

$$\frac{\partial T_p}{\partial x} = \frac{3}{2} \frac{k_g \text{Nu}}{u_p C_s \rho_p r_p^2} (T_g - T_p) \quad (87)$$

Equating the momentum and energy transfers between the two phases, with α defined as the ratio of the particle to gas mass flows, yields the following two conservation equations.

$$\frac{\partial u_g}{\partial x} = \frac{[\alpha \gamma u_g - \alpha(\gamma-1)u_p] \frac{\partial u_p}{\partial x} - \alpha(\gamma-1)C_s \frac{\partial T_p}{\partial x}}{\frac{c_p T_g}{u_g} (\gamma-1) - u_g} \quad (88)$$

$$\frac{\partial T_g}{\partial x} = \left(\frac{T_g}{u_g} - \frac{u_g}{R} \right) \frac{\partial u_g}{\partial x} - \frac{\alpha u_g}{R} \frac{\partial u_p}{\partial x} \quad (89)$$

In order to solve this system of differential equations, it is also necessary to use the following relation for the rate of change of pressure, generated by taking the spatial derivative of the ideal gas law and transforming the density term into a velocity term through the expression for continuity in a constant area duct.

$$\frac{\partial P}{\partial x} = \frac{P}{T_g} \left(\frac{\partial T_g}{\partial x} - \frac{T_g}{V_g} \frac{\partial V_g}{\partial x} \right) \quad (90)$$

The particle drag coefficient and Nusselt number correlations used in the above equations are taken from Maxwell and Seasholtz, and differ only slightly in value from the expressions used in the Q1D code in this flow regime. These equations were then solved using a simple explicit space-marching routine, with a step size of 1×10^{-6} m.

In order to fully validate the two-phase capability of the Q1D code, a particle/gas mass ratio, α , of 0.2 was selected for comparison with a solution using the analysis method of Maxwell and Seasholtz. At this mass ratio, both the particles and the gas respond significantly to the presence of the other phase. A particle diameter of 2 μm and a particle/gas specific heat ratio of 1.125 was used in both analyses. The Q1D simulation was run by first establishing a steady, subsonic gas flow in the constant area duct that approximated the post-shock conditions, as determined from the standard Hugoniot relations. A total pressure, total temperature subsonic characteristic inflow boundary condition and a fixed static pressure subsonic characteristic outflow boundary condition, both based on the methodology of Poinsot and Lele (1992), were used to establish this initial solution. The particles were then introduced into the flow at the desired mass fraction from a fixed position in the computational domain as the solution continued to run. Each set of particles was inserted at the pre-shock static temperature and flow velocity. The solution was then allowed to run out to a new steady state solution. As the gas-solid interactions caused the gas mass flow to shift from the initial result, the particle mass flow rate was continuously adjusted to maintain a particle/gas mass ratio of 0.2. The gas phase inlet velocity, static temperature, and static pressure also shifted from the initial gas-phase solution due to the interaction with the particles. These new static/total ratios were then characteristic of a slightly different shock Mach number. Therefore, the analytical solution was run at the gas flow inlet conditions of the converged numerical solution for comparison.

Figures 16 and 17 show excellent agreement between the Q1D simulation and the Maxwell/Seasholtz analysis gas temperature and gas velocity from the point of particle introduction to the end of the computational domain. Figures 18 and 19 show the corresponding results for the particle “stream”, also with excellent agreement between the two methods.

These results are consistent with the expected behavior of the two phases as given by Maxwell and Seasholtz. The slight differences between the results of the two methods observed in Figures 16 to 19 are due to a combination of the different particle drag coefficient and Nusselt number correlations used in the different calculations, and the use of varying thermodynamic and transport properties in the Q1D code versus the fixed values used in the Maxwell/Seasholtz analysis.

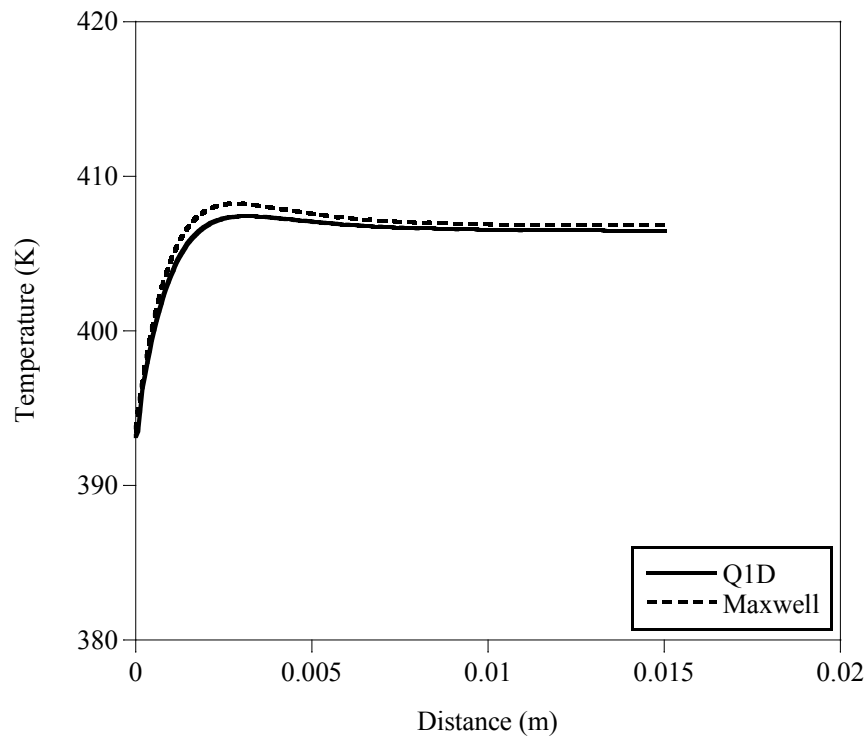


Figure 16.—Gas temperature profile from Q1D calculation from point of particle insertion compared to gas temperature profile from Maxwell/Seasholtz analysis.

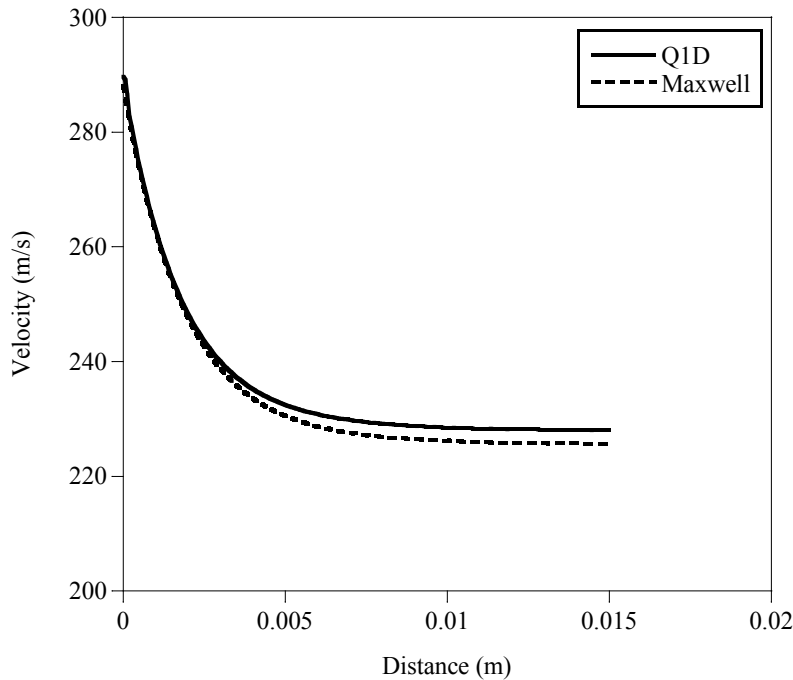


Figure 17.—Gas velocity profile from Q1D calculation from point of particle insertion compared to gas velocity profile from Maxwell/Seasholtz analysis.

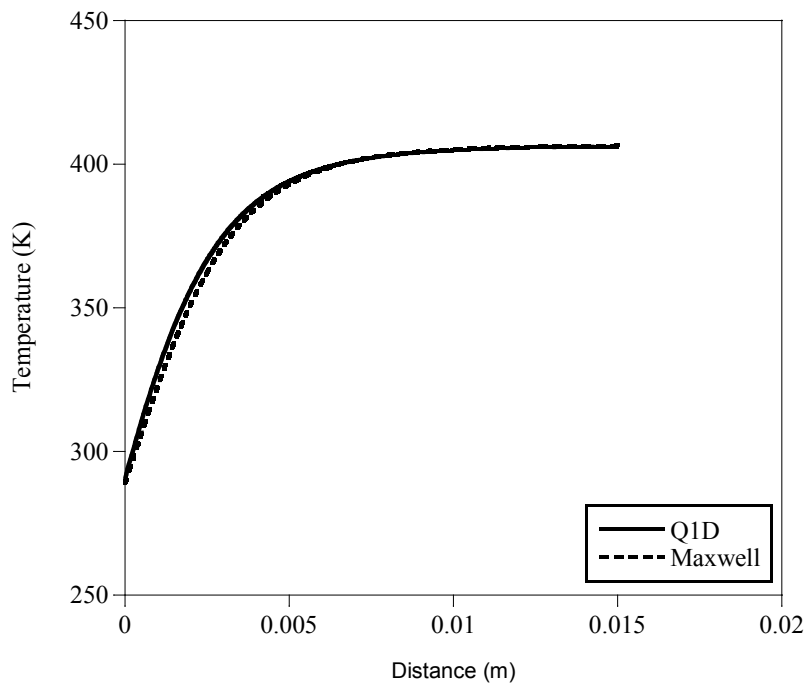


Figure 18.—Particle temperature profile from Q1D calculation from point of particle insertion compared to particle temperature profile from Maxwell/Seasholtz analysis.

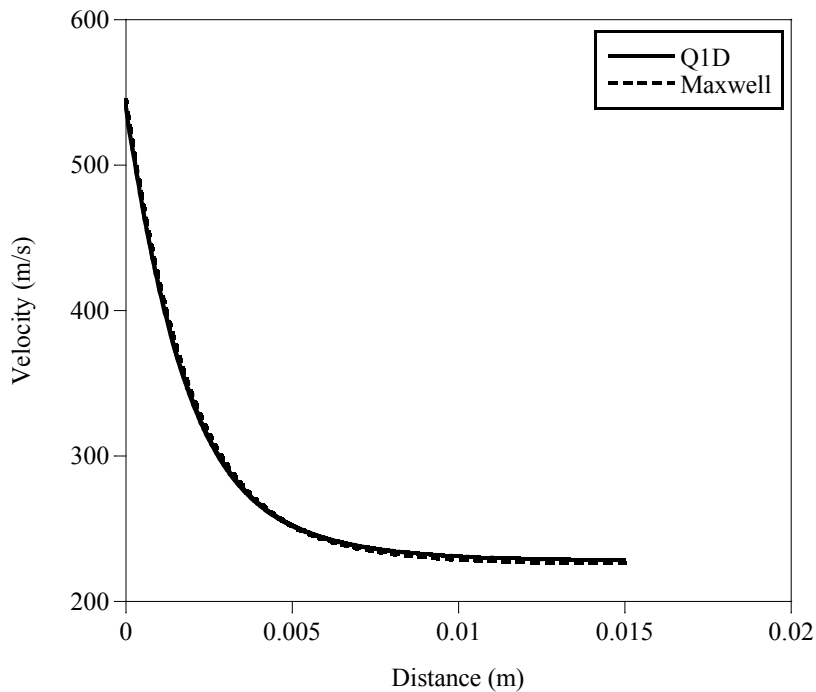


Figure 19.—Particle velocity profile from Q1D calculation from point of particle insertion compared to particle velocity profile from Maxwell/Seasholtz analysis.

3.3 Particle Internal Heat Transfer, Heat Release and Supersonic Drag/Convection Validation

Next, the results of Baek (1985), summarized also in Sichel, et al. (1985), were used to validate the particle internal heat transfer/heat release modeling in the Q1D code, as well as the supersonic relative Mach number drag and convective heat transfer correlations. Baek performed a series of experiments examining the shock ignition of various types and sizes of particles, which he then also examined using a computational model and asymptotic analysis. The most comprehensive set of results reported by Baek were obtained using 53 μm coal particles subjected to a Mach 4.8 traveling shock wave. The particles were injected into a shock tube containing pure oxygen at 1/3 of an atmosphere pressure and 295 K in the driven section. The mass of the particles was very small compared to the mass of gas present, so the particles were assumed to have no effect on the gas flow. The particles were also assumed to be of uniform size and spherical. The coal particles were characterized as having the following physical properties.

Density:	1200 Kg/m^3
Thermal Conductivity:	0.887 J/m-s-K
Heat Capacity:	987.4 J/Kg-K
Heat of Combustion:	35812 KJ/Kg
Internal Surface Area:	426000 m^2/Kg

Under the conditions tested, the particle consumption rate, in $\text{g/cm}^2\text{-s}$ (based on the particle external surface area), was assumed to follow a simple Arrhenius expression of the same form as shown in Equation (91), with an activation energy of 35,700 cal/g-mole and a pre-exponential factor of 87,100 $\text{Kg/m}^2\text{-s-atm}$. Baek's numerical single-particle combustion model was found to match the experimental data well over a range of shock Mach numbers and particle sizes.

In the Q1D code, this scenario was modeled by looking at a single 53 μm coal particle, with the physical properties listed above, injected at zero velocity into a steady flow at the post-shock conditions as calculated from a standard ideal shock tube calculation, such as that found in Saad (1985). A particle porosity of 0.32 with 2 nm diameter pores was found to give the required internal surface area. The two Arrhenius rate expressions required for the Hong particle combustion kinetic rate, Equation (59) (restated below), were defined as shown in Equations (91) and (92) to match the behavior of the simple kinetic expression of Baek. The Q1D code was then run until ignition occurred.

$$r_{k,i} = \left\{ n_{avg} + \frac{S_{ext}}{S_{int}} \right\} \frac{S_{int}}{S_{tot}} \frac{k_{1p,i} P_{O_2,S} M_c}{1 + K_{p,i} P_{O_2,S}} \quad (59)$$

$$k_{1p} = 3.09 \times 10^9 e^{\frac{-35700}{R_u T_{p,i}}} \quad (91)$$

$$K_p = 13.4 e^{\frac{-30300}{R_u T_{p,i}}} \quad (92)$$

The results from the Q1D code are compared to the results from Baek (1985) in Figures 20 to 22. The Baek results were recalculated using Baek's original code, a listing of which was included in the report. Figure 20 shows the gas-particle relative Mach number from just after particle insertion up until the time at which the particle ignited in the Baek calculation. The small difference in relative Mach number reflects differences in the thermodynamic properties between the two codes, resulting in a slightly different sound speed in the gas. Other than this slight offset, the Mach number decay is nearly identical, which is to be expected, as Baek also used the Henderson (1976) particle drag correlations, given in Equations (31) to (34).

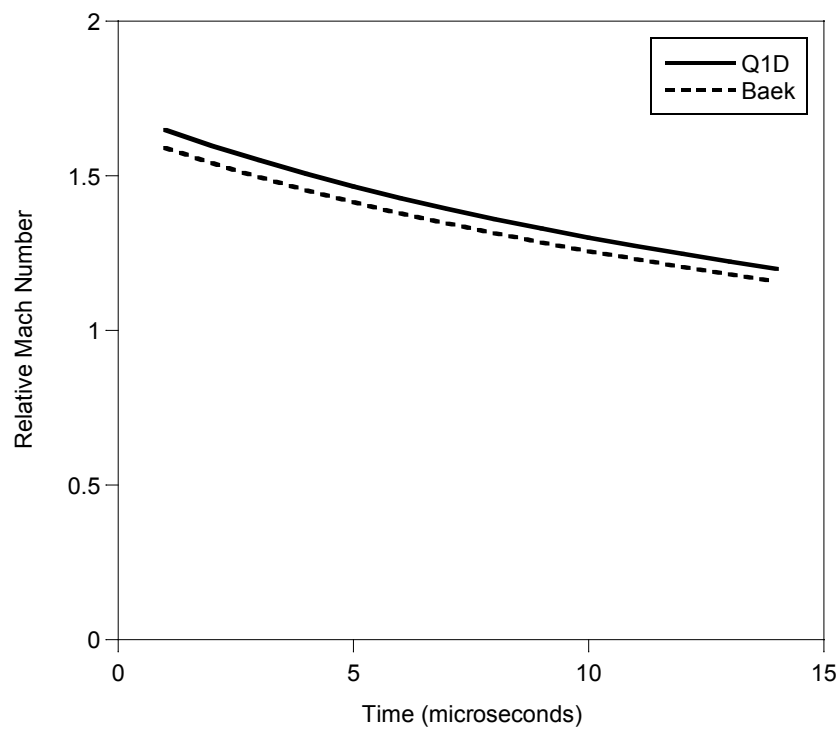


Figure 20.—A comparison of the post-shock gas-particle relative Mach number profiles between the Q1D and Baek codes.

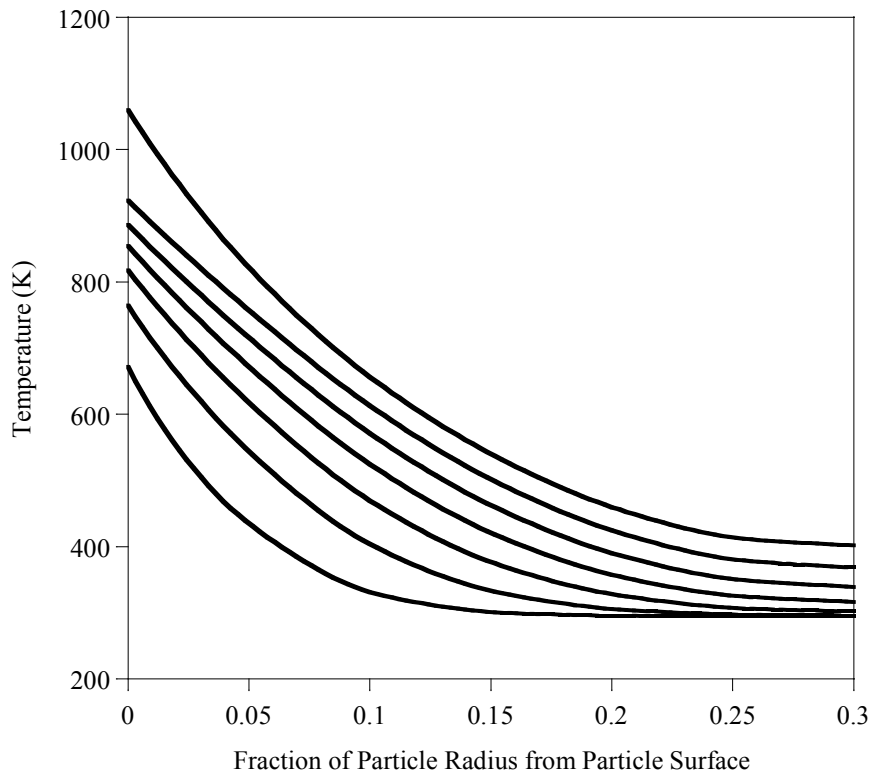


Figure 21.—Internal temperature profiles at 2 μ sec intervals of particle heating up to ignition from Baek code.

Figure 21 shows a time series of particle internal temperature profiles as calculated using Baek's code. The particle surface temperature is at the left hand side of the plot, with the temperature falling off with distance into the particle. The lowest temperature profile corresponds to 2 μ sec after the passage of the shock wave, and each succeeding temperature profile represents the passage of another 2 μ sec of time. Ignition occurs just prior to the 14 μ sec (uppermost) profile.

Figure 22 shows a similar plot of results from the Q1D code. The overall ignition process took approximately 4 μ sec longer in this simulation, due to a combination of small differences in the thermodynamic properties, transport properties, and heat transfer relations used in the different codes. While this approximately 25 percent increase in ignition time seems significant, it actually represents a very small difference in particle heating rate. The continual decrease in the convective heating rate of the particle due to the decrease in the relative velocity between the gas and the particle and the decreasing temperature difference leads to the particle surface approaching the ignition temperature asymptotically. This behavior translates to a high sensitivity of the ignition time to the heating rate, since it could take a significant portion of the ignition time to heat the last few percent of the required temperature rise.

Even with this longer ignition time, the Q1D result is within the scatter of the experimental data for ignition delay given by Baek for this condition. Taking this into consideration, the Q1D code results compare quite favorably with the analysis and experimental results of Baek.

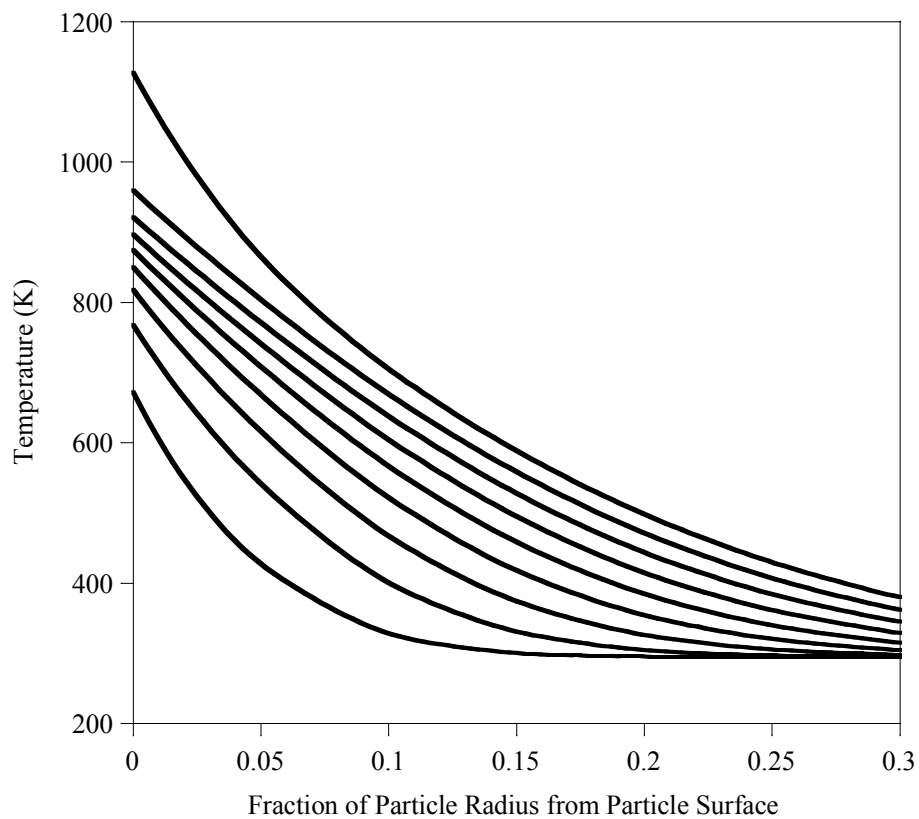


Figure 22.—Internal temperature profiles at 2 μ sec intervals of particle heating up to ignition from Q1D code.

4.0 Generation of Graphite Kinetic Constants

The graphite combustion rate expression, Equation (59), repeated below, requires that the constants in the kinetic rate expressions, Equations (55) and (56), also repeated below, be derived from experimental data for the given material and particle shape.

$$r_{k,i} = \left\{ \eta_{avg} + \frac{S_{ext}}{S_{int}} \right\} \frac{S_{int}}{S_{tot}} \frac{k_{1p,i} P_{O_2,S} M_c}{1 + K_{p,i} P_{O_2,S}} \quad (59)$$

$$k_{1p} = 6.29 \times 10^8 e^{\frac{-51000}{R_u T_{p,i}}} \quad (55)$$

$$K_p = 13.4 e^{\frac{-10100}{R_u T_{p,i}}} \quad (56)$$

The above expressions contain the two sets of kinetic rate constants given by Hong (2000) for non-porous graphite flakes, based on the experimental data of Ranish and Walker (1993). While the data used to generate this data covers a broad pressure range (from 0.1 MPa up to 6.4 MPa) over a solely kinetically controlled temperature range (733 to 842 K), the graphite flakes used were significantly different in composition, structure and shape than the graphite spheres of interest in this study. The Ranish and Walker graphite flakes averaged 30 μm in diameter and 0.5 μm thickness. They were also a high purity, non-porous natural crystalline graphite. In the HTF facility described earlier, the graphite used in the facility heater and the piping liners is Union Carbide PGX graphite (GrafTech, 2005). PGX is an artificial molded graphite material formed using lampblack particles as large as 0.8 mm held together with a coal-tar pitch based binder. These materials are mixed together, poured into a mold and graphitized by baking. The resultant material has a density of 1730 Kg/m^3 (Graftech, 2005), which translates to a porosity of 0.2345 (based on a non-porous graphite density of 2260 Kg/m^3) with an average pore diameter of 6 μm (Pierson, 1993). Observations made during test facility operations indicate that roughly spherical particles are to be expected. Because of these differences, an alternate data set from which to generate the kinetic constants was needed. However, no available data set was found in the literature for an appropriate material that covered the pressure and temperature range of interest. In particular, no data sets including data for pressures above 1 atmosphere were found. Because of this, the Hong kinetic constants were used as a starting point, since they included the effect of pressure, and then the constants in the k_{1p} expression were modified to fit the available ambient pressure data.

The frequently referenced graphite sphere combustion rate data of Tu, et al. (1934) was one possible data set, but upon examination, it was found that the graphite used was not sufficiently characterized so as to provide all the inputs needed for the combustion model of Hong. A number of other graphite oxidation data sets, such as that of Okada and Ikegawa (1953), were obtained for cylindrical graphite electrodes, but not for spheres. The only applicable data was that taken by Froberg (1967) in a set of experiments modeled after the work of Tu, et al. (1934), but for which significantly more graphite characterization information was available. The graphite used by Froberg had a density of 1650 Kg/m^3 and an average pore diameter of 5 μm , both similar to the PGX graphite used at HTF. In the set of Froberg's experiments that were used to generate the graphite rate constants for this study, large graphite spheres (~12.6 mm diameter) were exposed to heated air streams with air temperatures ranging from 813 to 1196 K. The air heater inflow velocity was held constant at 1.0 cm/s (at standard temperature and pressure), which resulted in an increasing air velocity as the air temperature was raised. The graphite sphere was allowed to come to equilibrium before combustion rate data was taken, which resulted in graphite surface temperatures as high as 1311 K for the highest temperature air flow. The combustion rate was directly measured via sphere weight loss.

For the Q1D simulation of this configuration, thermal conductivity and heat capacity as a function of temperature were also needed for the graphite. As this data was not available from Froberg for the specific graphite studied, estimates were made based on literature information. The thermal conductivity of PGX is 120 W/m-K at room temperature (Graftech, 2005) and decays exponentially as temperature increases. It was assumed that the Froberg graphite had the same room temperature thermal conductivity as the PGX. The thermal conductivity decay rate, as well as graphite specific heat as a function of temperature, are given graphically by Pierson (1993), and were used to generate 3rd order polynomial curve fits of these properties for use in the Q1D code, as shown in Figures 23 and 24. For those cases where an internal particle temperature profile was used, mass-averaged values for heat capacity and thermal conductivity were used.

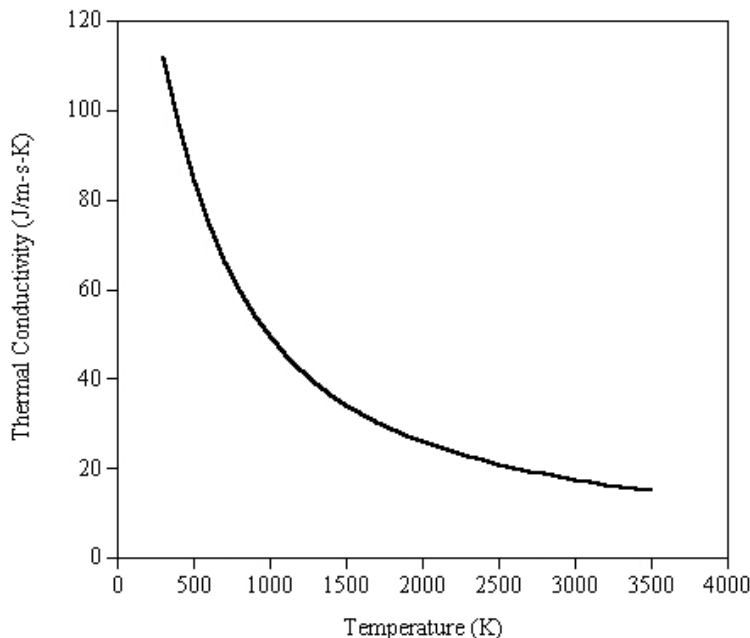


Figure 23.—PGX graphite thermal conductivity.

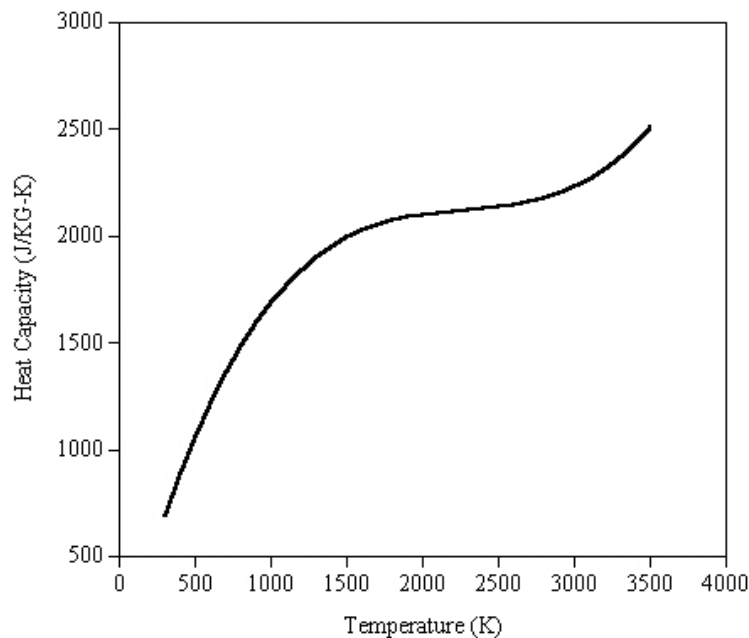


Figure 24.—PGX graphite heat capacity.

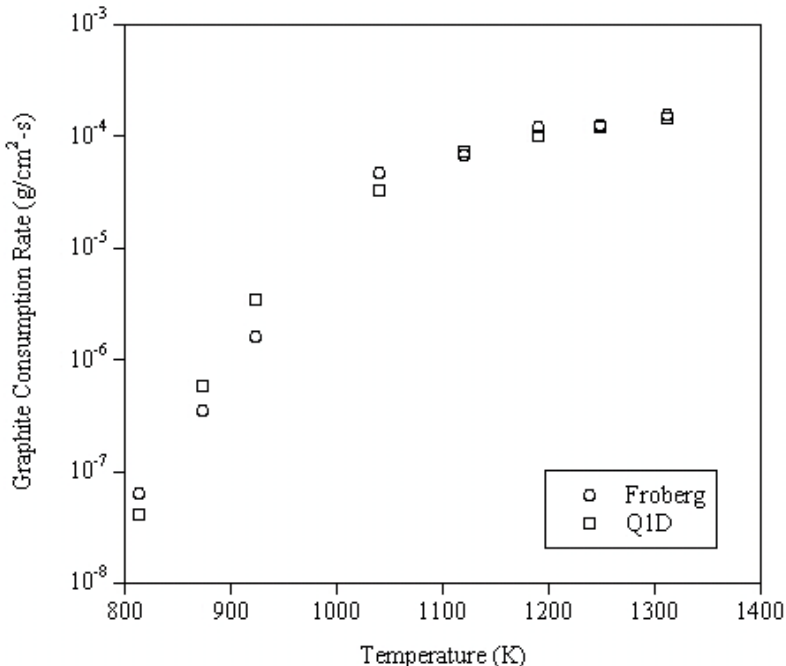


Figure 25.—Q1D kinetic constant fit to Froberg data.

With this information, Q1D simulations of a number of data points from Froberg were made, and the kinetic constants adjusted until the simulations and the experimental results were in reasonable agreement. The resultant expression for k_{1p} is given in Equation (93), which represents a factor of 11.3 increase in the pre-exponential factor and a 24 percent increase in the activation energy over the expression from Hong (2000) for non-porous graphite flakes given in Equation (55).

$$k_{1p} = 7.11 \times 10^9 e^{\frac{-63100}{R_u T_{p,i}}} \quad (93)$$

A graphical comparison between the Froberg data and the adjusted kinetic model is shown in Figure 25, based on the sphere surface temperature. Using this adjusted expression for k_{1p} , PGX graphite can be simulated by adjusting the particle density, pore diameter, and particle size to the appropriate values.

5.0 Model Facility and Scramjet Simulation Geometry and Flow Conditions

5.1 Test Facility Components

In the introduction, two different hypersonic propulsion test facility storage-heater types were described. The first utilized ceramic pebbles heated by flowing combustion exhaust gases through the bed. The second consisted of inductively heated drilled graphite blocks. The first type is found in the GASL Leg IV facility (Roffe, et al., 1997), while the second type is used at the NASA Plumbrook HTF facility (Perkins, et al., 1998). Schematics of these facilities were presented in Figure 1 and Figure 2. Rather than attempting to simulate both of these existing facilities for this code demonstration, a single facility geometry will be used to allow for a direct comparison of results for non-reacting and reacting particles. As the goal of this study is not to determine the state of particulates entering the combustor of a particular facility at a specific test condition, but instead to parametrically determine the range of particulate states that could be encountered, and the dominant physical processes that determine these states, the use of a generic facility geometry does not detract from the objectives of the study.

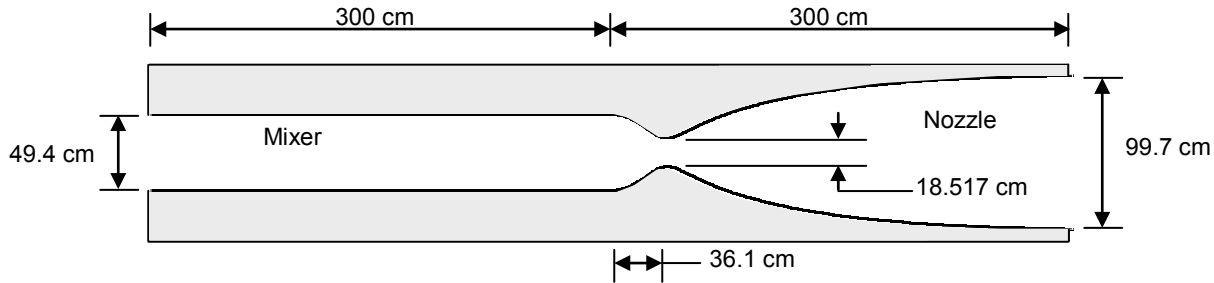


Figure 26.—Scaled axisymmetric geometry for facility settling chamber/mixer and nozzle.

The selected generic facility geometry, shown in Figure 26, consists of a 3 m long low speed (~ Mach 0.08 gas flow velocity) mixing section followed by a 3 m long Mach 5 exit freejet nozzle. The scale of the mixer and nozzle sections is slightly less than that of the NASA HTF facility, and considerably larger than that of GASL Leg IV facility. The nozzle contour was generated using a spline fit to the inlet, throat, and exit axial locations and diameters, estimated from the facility descriptions given in the above cited facility references. The same nozzle geometry is used for testing at simulated flight Mach numbers of 5, 6, and 7 by adjusting the mixer section inflow total pressure and total temperature, and by adjusting the flow deflection angle and length of a pre-compression plate that will be described in detail in the next section. The inflow conditions for the Mach 5, 6 and 7 simulated flight conditions are given in Table I, along with the representative flight dynamic pressures used to calculate the facility conditions, and include corrections for real gas effects taken from NASA compressible flow tables (Ames Research Staff, 1953).

TABLE 1.—MIXER SECTION INFLOW TOTAL PRESSURE, TOTAL TEMPERATURE AND DYNAMIC PRESSURE FOR MACH 5, 6 AND 7 SIMULATED FLIGHT CONDITIONS

	P_{total} (KPa)	T_{total} (K)	Dynamic pressure (KPa)
Mach 5	3082	1219	89
Mach 6	4498	1652	54
Mach 7	8247	2174	47

5.2 Scramjet Inlet and Isolator Sections

After the facility components are defined, it is necessary to define the geometry of the scramjet model to be simulated. In practice, the entire scramjet inlet is not used in ground testing due to its length. The multiple external compression ramps are instead replaced by a single pre-compression plate that provides the same inflow condition at the engine inflow plane. However, it is still necessary to define the full inlet geometry in order to determine the appropriate pre-compression plate geometry. Figure 27 shows a generic, unscaled scramjet inlet and isolator, along with a short section of the combustor. Table 2 defines the geometric parameters shown in the figure for a Mach 7 design point inlet/isolator system. The values upstream of the engine throat were determined by first selecting the throat height, H_1 , to set an overall engine scale consistent with the generic facility size, and then iterating on the compression ramp angles and lengths such that all of the oblique shocks converge on the cowl lip, and the cowl lip oblique shock in turn impinges on the shoulder that defines the inlet throat, as shown in Figure 27. This design was further constrained by the typical design practices of keeping the compression ramp turning angles approximately equal to minimize overall total pressure loss, and of targeting a throat Mach number of approximately one-half of the free stream Mach number. The isolator section was sized using the methodology described by Heiser and Pratt (1994) for constant area isolators, with an isolator pressure ratio of 2. The slight

divergence angle within the isolator section accounts for boundary layer growth that would otherwise restrict the flow in the duct. A series of linked spreadsheets were used to automate this design process.

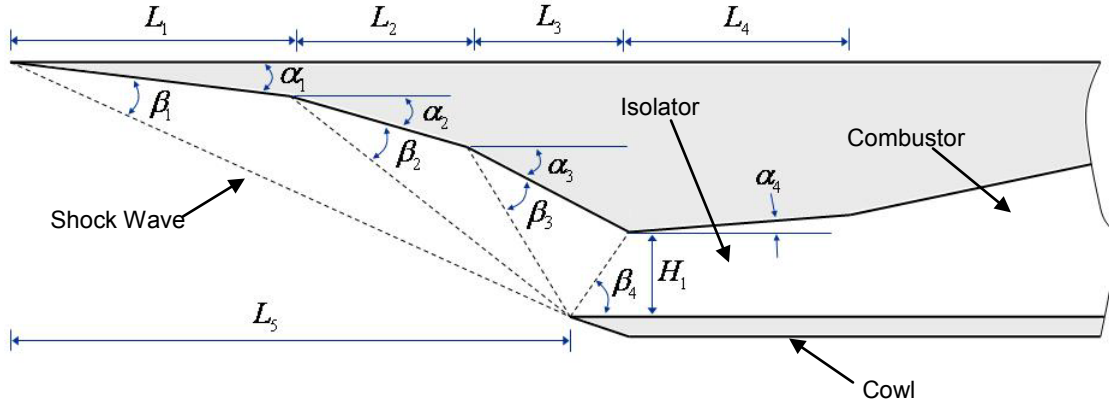


Figure 27.—Scramjet geometric design parameters.

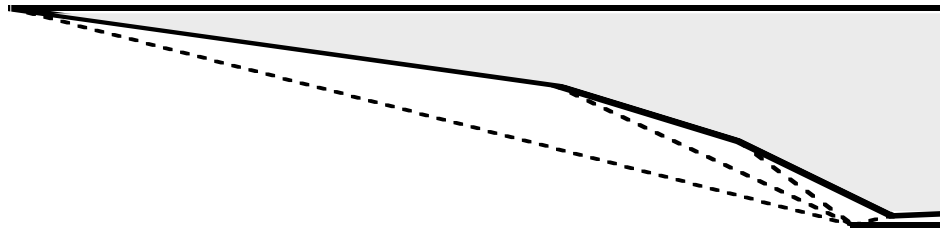


Figure 28.—Scaled inlet/isolator at Mach 7 design point.

Figure 28 shows a scaled representation of the inlet/isolator and the shock system at the Mach 7 design point based on the geometric parameters given in Table 2. Figures 29 and 30 show the shock structure moving out from the cowl lip as the flight Mach number is decreased to Mach 6 and Mach 5, respectively. Table 3 then provides the static pressure, static temperature, and Mach number at key points through the geometry for the selected Mach 5, 6 and 7 flight conditions. It should be noted that the conditions at the isolator entrance are a result of the combination of the cowl lip oblique shock with an expansion fan emanating from the inflection point at the inlet throat , which is not shown in Figures 27 to 30.

TABLE 2.—SUMMARY OF MODEL SCRAMJET INLET/ISOLATOR GEOMETRY AT MACH 7 DESIGN POINT

$L_1 = 353.2 \text{ cm}$	$H_1 = 6.0 \text{ cm}$	$\beta_1 = 6.4^\circ$
$L_2 = 120.2 \text{ cm}$	$\alpha_1 = 8^\circ$	$\beta_2 = 8.2^\circ$
$L_3 = 99.6 \text{ cm}$	$\alpha_2 = 17^\circ$	$\beta_3 = 10.4^\circ$
$L_4 = 33.2 \text{ cm}$	$\alpha_3 = 26^\circ$	$\beta_4 = 13.2^\circ$
$L_5 = 547.6 \text{ cm}$	$\alpha_4 = 2^\circ$	-----

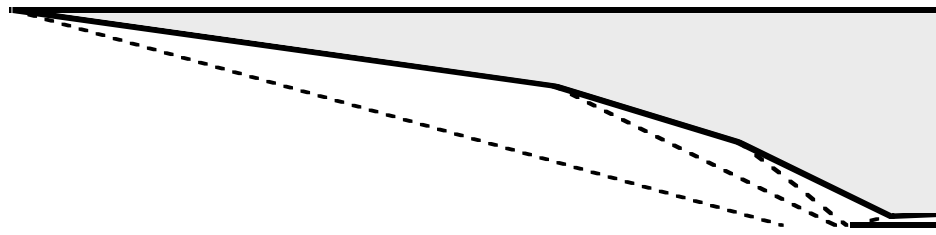


Figure 29.—Scaled inlet/isolator with shock locations corresponding to Mach 6 operation.

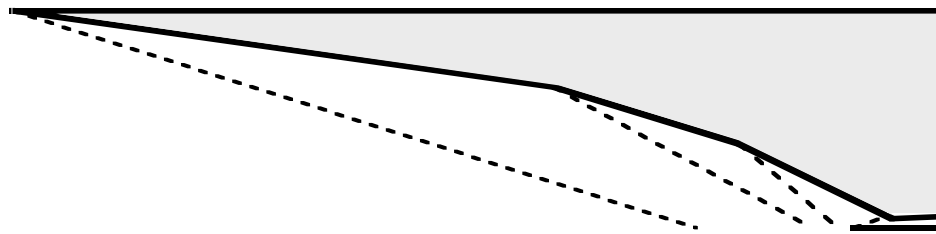


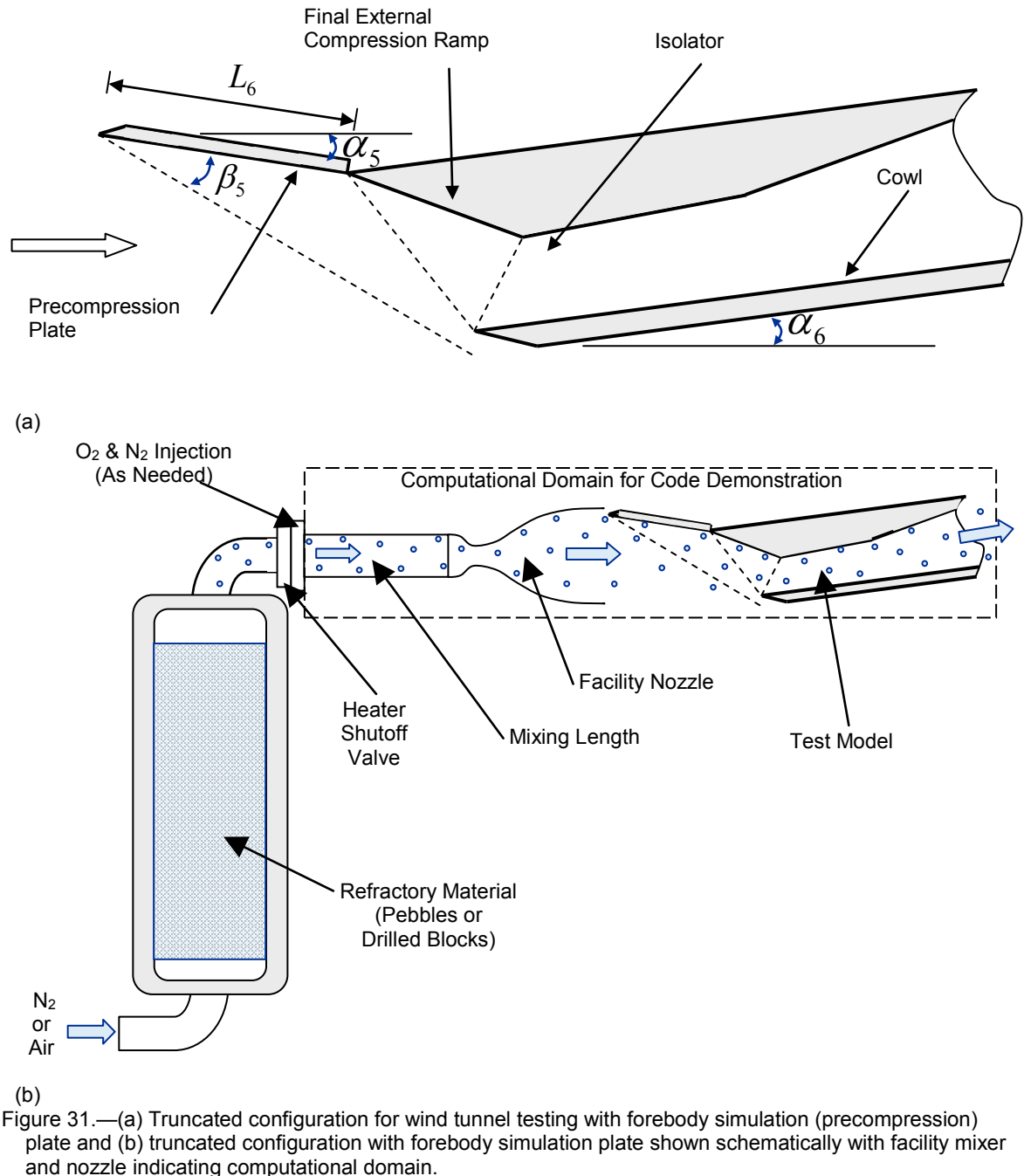
Figure 30.—Scaled inlet/isolator with shock locations corresponding to Mach 5 operation.

TABLE 3.—SUMMARY OF FLOW FIELD CONDITIONS FOR MODEL SCRAMJET

	Mach 5			Mach 6			Mach 7		
	P_{static} (Pa)	T_{static} (K)	Mach no.	P_{static} (Pa)	T_{static} (K)	Mach no.	P_{static} (Pa)	T_{static} (K)	Mach no.
Free stream	5024	215	5	2110	227	6	1370	230	7
Along 1 st ramp	12600	285	4.2	6200	319	5.0	4670	342	5.6
Along 2 nd ramp	30100	372	3.6	16900	434	4.1	14200	483	4.6
Along 3 rd ramp	63500	463	3.0	39300	555	3.5	35800	634	3.8
Isolator inlet	60400	512	2.8	37400	636	3.1	34300	751	3.4
Isolator exit	120800	798	1.8	74800	1000	2.0	68600	1237	2.2

Having established the scramjet inlet/isolator geometry and the flow conditions at each step through those components, the test configuration to be used can be defined. To shorten the scramjet geometry, the first two external compression ramps from Figure 27 are replaced by a single pre-compression plate, leaving the last external compression ramp, the cowl, and the isolator unchanged. In order to create the same conditions along the last external compression ramp before the throat as those achieved in the original configuration from Figure 27, the geometry has to be rotated slightly counter-clockwise, as shown in Figure 31(a). This rotation compensates for the change in the flow direction coming at the last

external compression ramp in the shortened configuration relative to that in the original configuration. Each of the geometric parameters shown in Figure 31(a) needs to be changed for each test Mach number to be able to match the flow conditions approaching the last external compression ramp calculated for the original configuration. The required values as a function of flight simulation Mach number are given in Table 4. The flow conditions remain the same along the last external compression ramp and within the isolator, but a new set of flow conditions are created along the precompression plate, which are given in Table 5. Figure 31 (b) shows the test article from Figure 31(a) schematically “installed” in the model test facility, indicating the full computational domain.



(b)
Figure 31.—(a) Truncated configuration for wind tunnel testing with forebody simulation (precompression) plate and (b) truncated configuration with forebody simulation plate shown schematically with facility mixer and nozzle indicating computational domain.

TABLE 4.—TEST ARTICLE CONFIGURATION FOR MACH 5, 6 AND 7 TEST CONDITIONS

	Mach 5	Mach 6	Mach 7
β_5	9.3°	9.3°	10.1°
α_5	15.0°	9.5°	4.5°
α_6	2.0°	7.5°	12.5°
L_6	100.6 cm	99.1 cm	84.0 cm

TABLE 5.—FLOW CONDITIONS ALONG THE PRE-COMPRESSION PLATE FOR MACH 5, 6, AND 7 TEST CONDITIONS

	Mach 5	Mach 6	Mach 7
P_{static} (Pa)	23700	21900	25200
T_{static} (K)	370	430	510
Mach no.	3.5	4.0	4.4

5.3 Modeling Approach

Simplifying assumptions must be made in order to model a gas-particle flow through the facility mixer, the facility nozzle, along two external compression ramps, through the inlet throat area and the isolator section using a quasi-1D code. Since the facility mixer and nozzle are assumed to be axisymmetric, it is straightforward to cast their geometry into a quasi-1D format. However, the precompression plate, final external inlet ramp and isolator geometries are inherently two-dimensional, as are the oblique shocks preceding each of those components and the expansion fan leading into the isolator. This difficulty was addressed by modeling each of these last three components separately from the mixer/nozzle section. The jump conditions across each of the oblique shocks were calculated from the exit conditions of the upstream component and the specified turning angle using classical methods, such as those found in Saad (1985). The calculated post-shock conditions were then used as the inflow boundary conditions for the next component. For the isolator, the post-shock conditions were used as the input to a classical expansion fan calculation to determine the inflow boundary conditions of that component. Each of these last components was then treated as a constant area section having a length equal to the corresponding body-side bounding surface, as shown in Figure 31. The isolator was considered as a constant area section, even though a slight area increase with length is shown in Figure 26. However, that area relief is designed to accommodate boundary layer growth so that the isolator can behave as a truly constant area section and not prematurely choke near the end of the duct. Since the 1-D analysis does not include boundary layer, a constant area duct was modeled. The cross-sectional area for these constant area sections can be any arbitrary value, though a value of 0.1 m² was generally used throughout. It should be noted that the length of each component is representative of the gas-particle flow near the bounding wall. Gas-particle flows further out from the wall will have a shorter residence time between shocks.

One additional modeling step was required for the isolator. Isolator flow is generally characterized by a complex, three-dimensional series of reflected oblique shocks, possibly followed by a weakened normal shock in the ramjet operating mode. It is not realistic to try and model this flowfield using a 1-D code. Instead, a uniform negative momentum source term was added to the momentum Equation (2), at each grid point along the isolator length to reflect the total pressure loss generated by the internal shock structure. This approach yielded nearly linear changes in the primary flow variables between the isolator inlet and exit, ending at the desired isolator exit values given in Table 3. This behavior for the various flow parameters can be observed in the various plots in the later Results section.

With these modeling assumptions, a 1 percent reacting particle mass fraction case had a typical total run time of approximately 80 hr on a dual-processor (2 GHz) PC workstation. This relatively long run time was driven primarily by the low convective velocity in the low-speed mixer section. A similar case with just a single reacting particle typically took approximately 40 CPU hours on the same machine. In both cases, a converged no-particle solution was used as the initial condition.

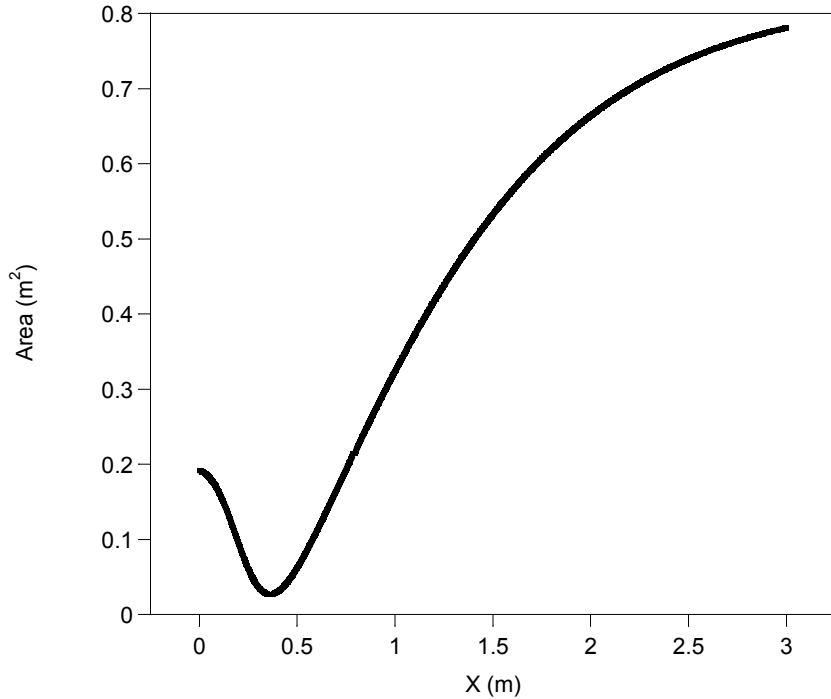


Figure 32.—Nozzle area distribution where $X = 0$ indicates the beginning of the convergent section of the nozzle.

5.4 Grid Descriptions

Simple uniform 1-D grids were used for each component. For the mixer/nozzle simulation, an overall grid totaling 4000 points was split two sections. An 800 point uniform grid was used for the 300 cm constant-area mixer section and a 3200 point uniform grid was used for the 300 cm nozzle section. The exact area distribution used for all of the simulations for the 3 m long nozzle, as shown schematically in Figure 26. Each of the remaining three components downstream of the nozzle was modeled using uniform 300 point grids.

6.0 Results

6.1 Inert Particle Calculations

A series of Q1D calculations were performed with inert alumina particles utilizing the test facility and scramjet geometries described in the previous section at the Mach 5 and 6 total temperature flow conditions defined therein. The Mach 7 total temperature condition was not run because this condition is near the melting point of alumina (2323 K). As mentioned in the introduction, particle diameters of 10 μm to 1 mm (1000 μm) were considered for this study. In addition to examining the two extreme particle diameters, an intermediate diameter of 100 μm was also included in the study to help define the effect of particle diameter on particle and gas flow conditions entering the model scramjet combustor. The majority of results shown below are for single particles traversing the facility mixer/nozzle, precompression plate, final inlet compression ramp and isolator components. Additionally, a single case with a 1 percent particle mass fraction was run to determine if the effect of increased particle mass fraction on the scramjet combustor inflow conditions warranted additional calculations at elevated inert particle mass fractions.

The particles used in this portion of the study were assumed to be low porosity, high purity tabular alumina. All the required material properties, including temperature dependent properties, were available

from Munro (1997), with the exception of particle emissivity. However, Pluchino and Masturzo (1981) determined that the emissivity of small alumina particles approaches zero as the material purity approaches 100 percent. As the tabular alumina is a very high purity form of alumina, it was therefore assumed that the particle emissivity was in fact zero for these calculations, eliminating all radiative heat transfer from the particles to the water-cooled facility walls (500 K wall temperature). The published density for tabular alumina is 3984 Kg/m³. Temperature dependant values of heat capacity and thermal conductivity are shown in Figures 33 and 34, respectively.

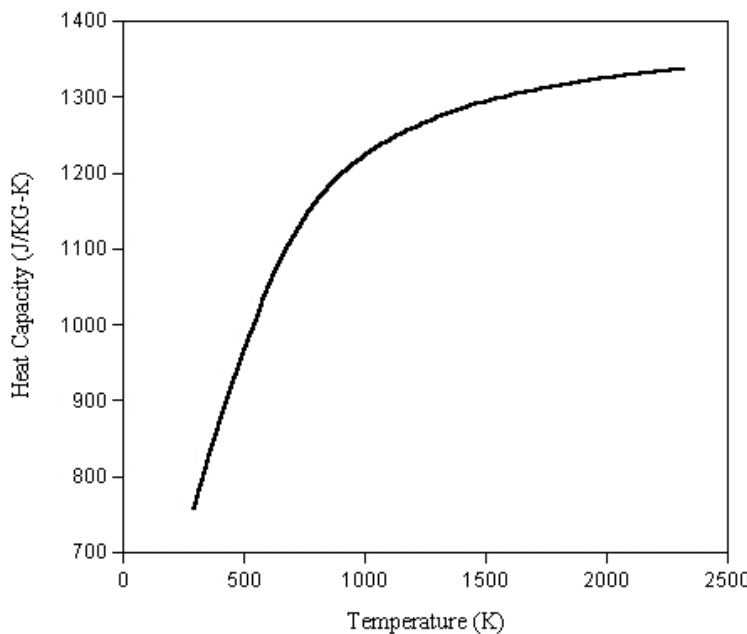


Figure 33.—Tabular alumina heat capacity.

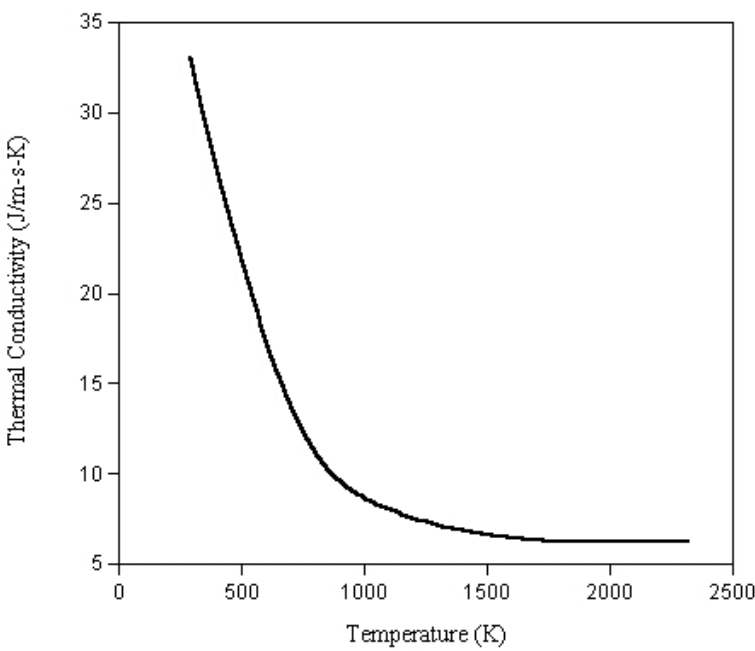


Figure 34.—Tabular alumina thermal conductivity.

It should be noted that these property values had to be extrapolated above 1800 K. However, as each of these properties approach an asymptote by that temperature, no significant error is incurred. For particles with an internal temperature gradient, mass-averaged values of these temperature dependent properties were calculated and applied at each time step.

Prior to running these inert particle cases, it was desirable to determine whether or not it would be necessary to include gas-phase chemistry in the calculations. Gas-only calculations with and without gas-phase chemistry were run at the Mach 5 and 6 total temperature conditions. The Mach 5 and 6 calculations showed no significant difference in the bulk fluid properties between the results with and without gas-phase chemistry. All minor species in the finite-rate chemistry calculations remained below 1 part-per-million throughout the computational domain for both conditions. Based on these results, it was determined that the inert particle cases could reasonably be run without using finite rate chemistry. By running all of the inert particle cases in this manner, significant computational run-time improvements were achieved.

A total of six cases were run using single 10-, 100- and 1000- μm alumina particles at the Mach 5 and 6 total temperature flow conditions. Initial test runs showed that the Biot number for the 10 μm particles never exceeded 0.1 during the simulation, indicating that those particles should be modeled as isothermal. The larger particles were modeled with internal grids of 51 grid points for the 100 μm particles and 101 grid points for the 1000 μm particles. The number of internal grid points for each particle size was selected by running a series of test cases with increasingly refined grids until the solution became grid independent. Figures 35 to 38 show the gas and particle surface temperature and velocity results for these six cases, each plot at a single facility operating point total temperature. Only a single gas-phase solution is given in each of these figures as the gas-phase solutions at any given Mach number are not effected by the insertion of a single particle. The discontinuities in the gas flow results indicate the positions of the oblique shock waves indicated in Figure 31 at each flow turning point. The particle initial temperature was set 200 K higher than the initial gas temperature in the mixer section to simulate the overheating of the test gas typically required in storage heater facility operations, as described earlier. The particle initial velocity is set to the incoming gas flow velocity.

Examining these figures, several observations can be made. First, that while the 10 μm particles reasonably follow the gas flow temperature and velocity profiles, the 100 and 1000 μm particles significantly lag the gas flow due to their higher mass to surface area ratio that decreases the particle drag relative to the particle inertia. Second, that while the 10 μm particles respond to the step-change in gas flow properties at the oblique shock positions, albeit with significant delay, the 100 and 1000 μm particles show almost no response to the shocks for the same reason as the first observation above. And lastly, that increasing the facility total temperature from the Mach 5 condition to the Mach 6 condition does little to alter the response of the particles, other than to shift the temperature and velocity scales. This shift in scales is more evident in Figures 39 to 44, where the data is replotted keeping the particle size constant in each figure, while varying the simulated Mach number total temperature.

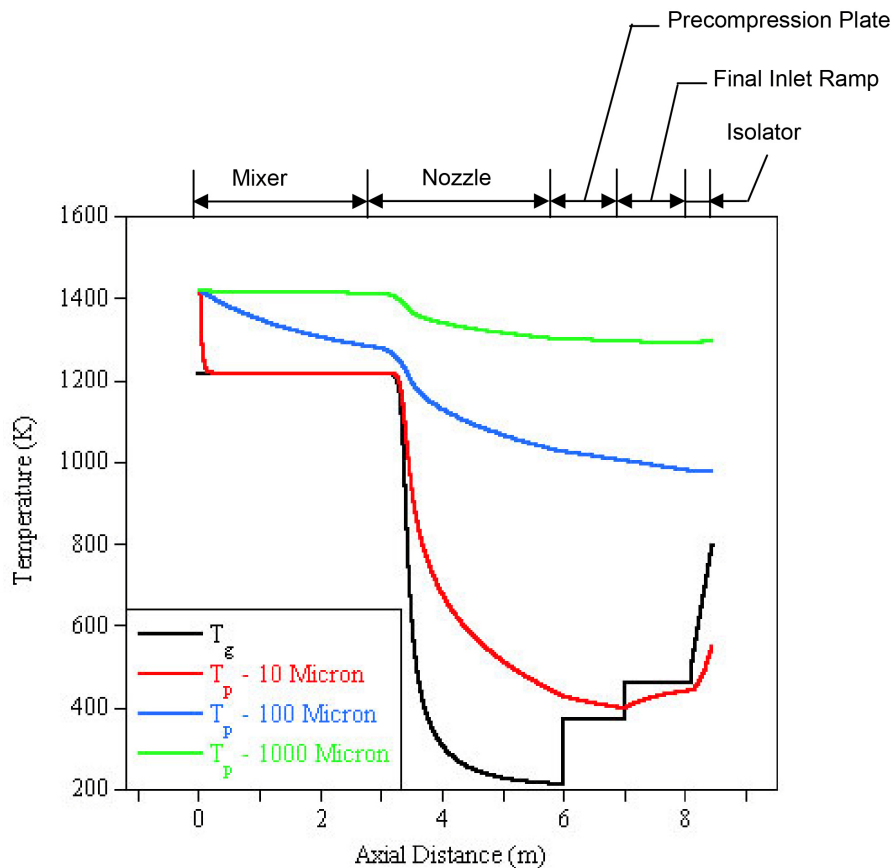


Figure 35.—Comparison of gas and single particle surface temperature profiles for various particle sizes for the Mach 5 total temperature flow condition.

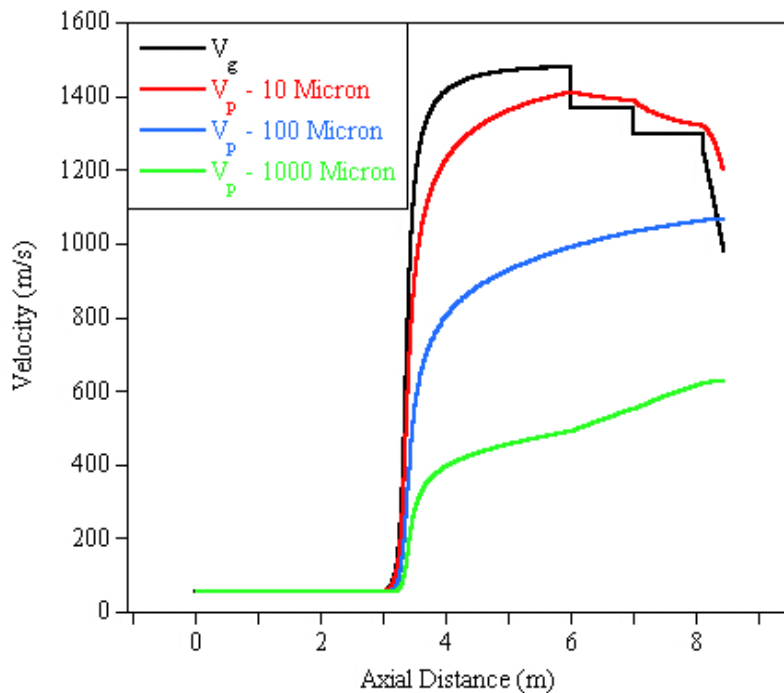


Figure 36.—Comparison of gas and single particle velocity profiles for various particle sizes for the Mach 5 total temperature flow condition.

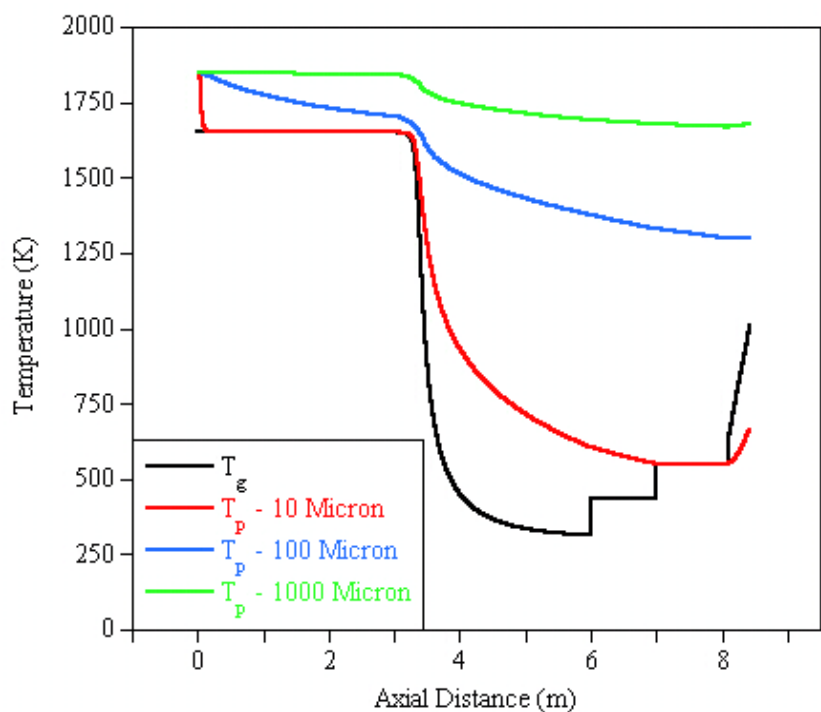


Figure 37.—Comparison of gas and single particle surface temperature profiles for various particle sizes for the Mach 6 total temperature flow condition.

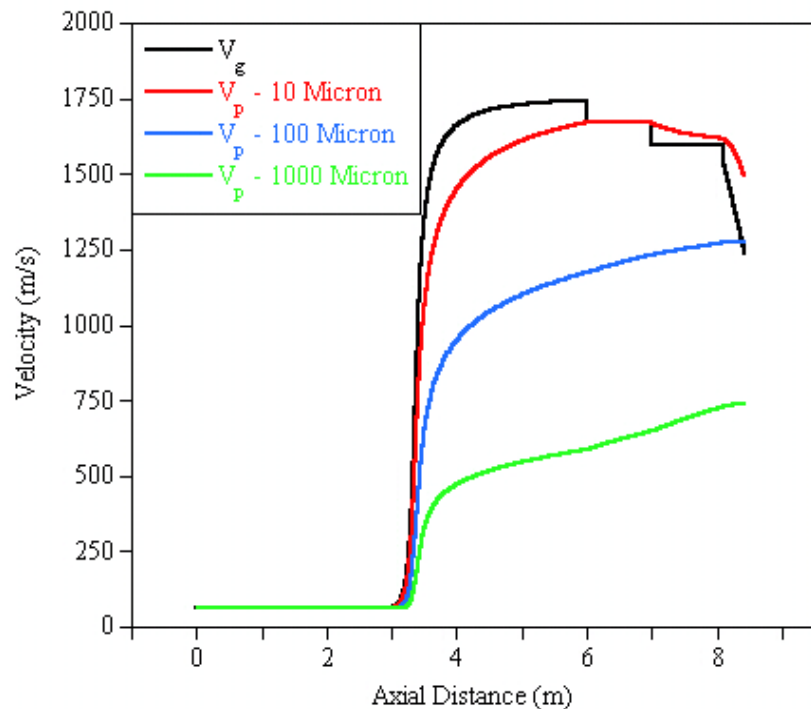


Figure 38.—Comparison of gas and single particle velocity profiles for various particle sizes for the Mach 6 total temperature flow condition.

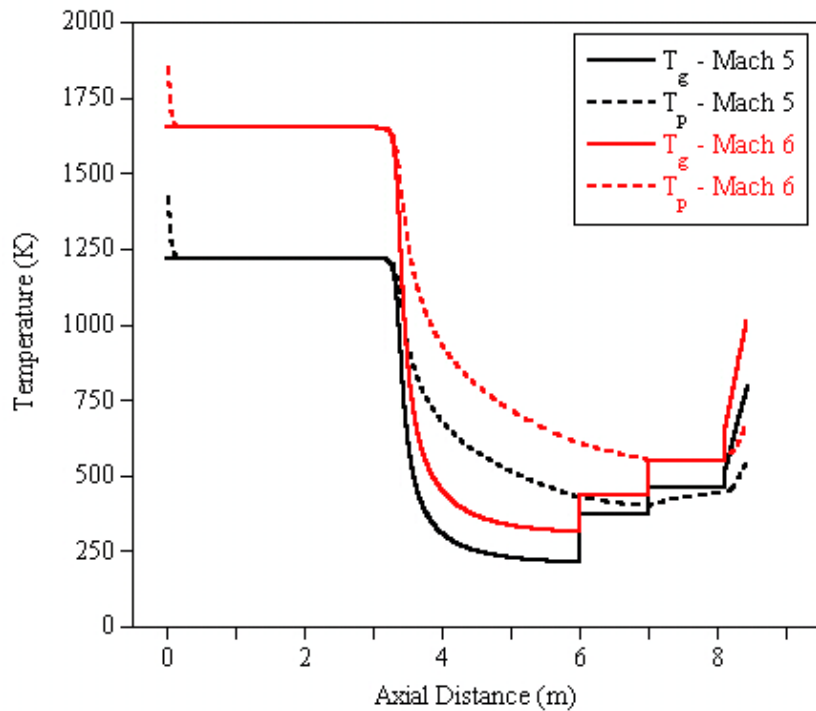


Figure 39.—Comparison of gas and $10 \mu\text{m}$ particle surface temperature profiles for Mach 5 and 6 total temperature flow conditions.

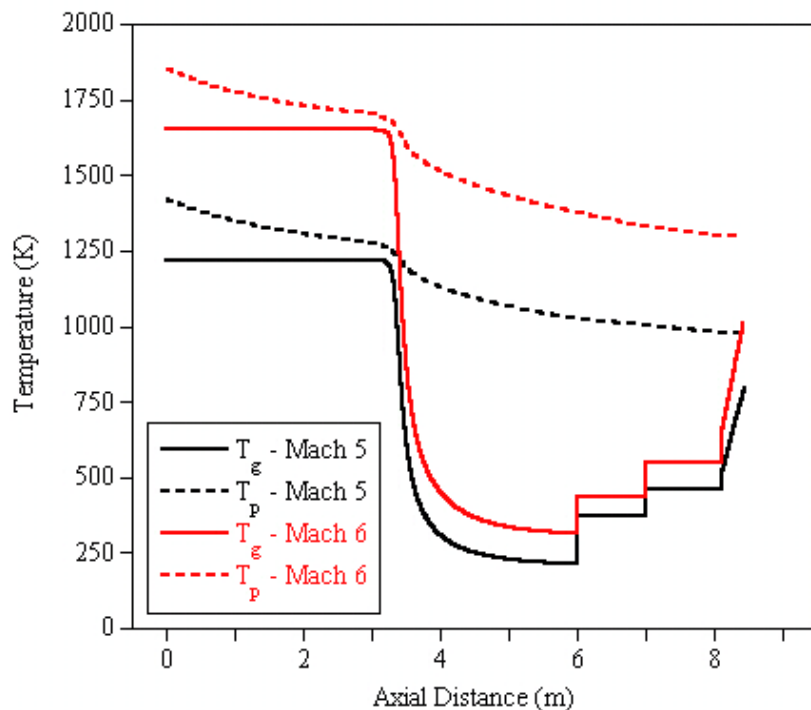


Figure 40.—Comparison of gas and $100 \mu\text{m}$ particle surface temperature profiles for Mach 5 and 6 total temperature flow conditions.

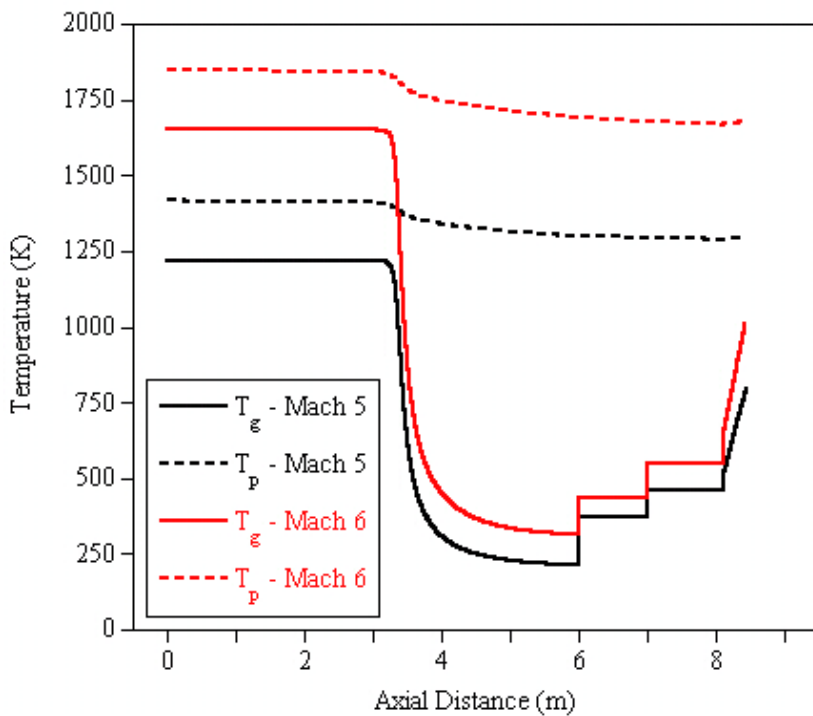


Figure 41.—Comparison of gas and $1000\text{ }\mu\text{m}$ particle surface temperature profiles for Mach 5 and 6 total temperature flow conditions.

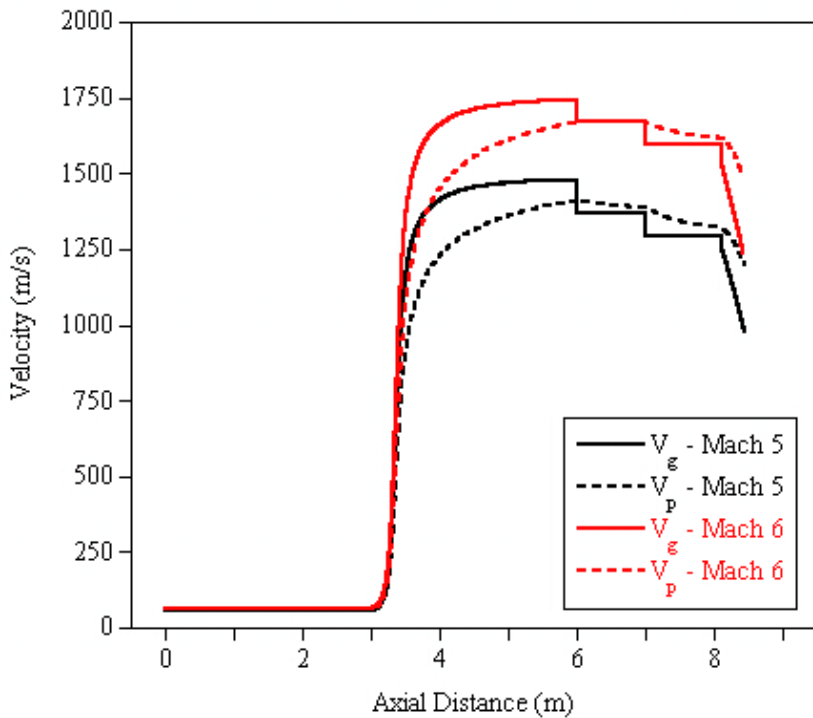


Figure 42.—Comparison of gas and $10\text{ }\mu\text{m}$ particle velocity profiles for Mach 5 and 6 total temperature flow conditions.

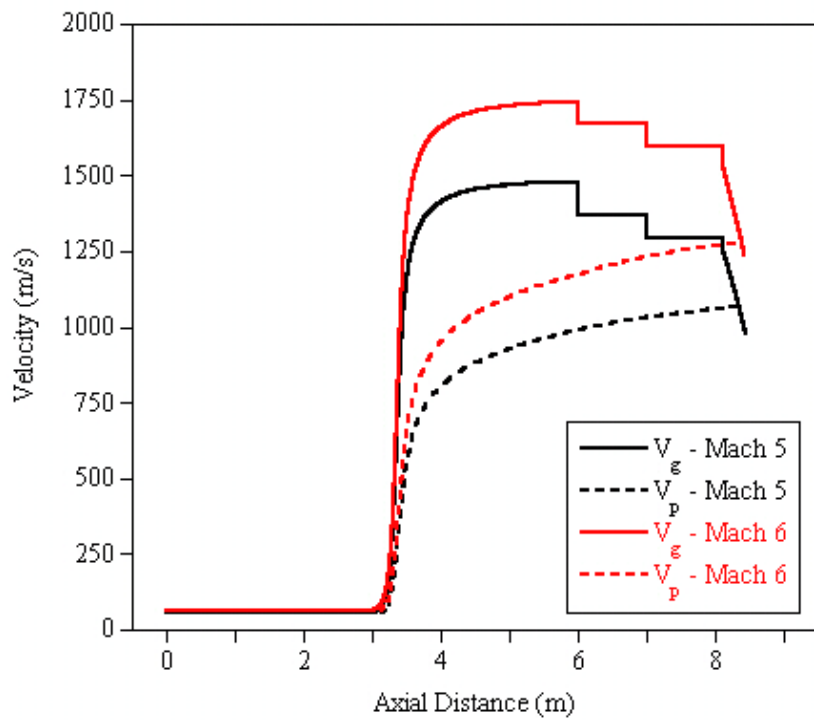


Figure 43.—Comparison of gas and 100 μm particle velocity profiles for Mach 5 and 6 total temperature flow conditions.

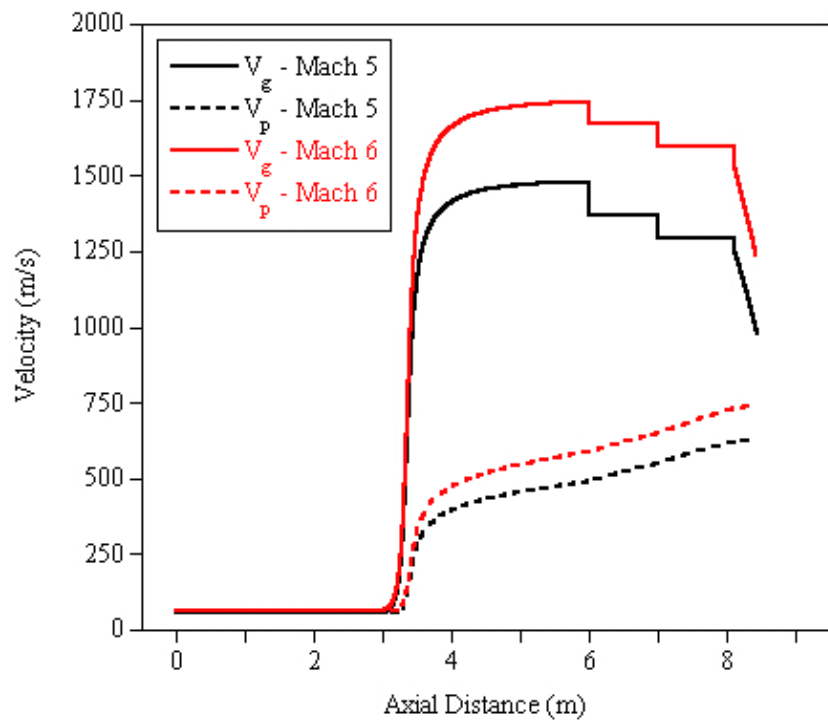


Figure 44.—Comparison of gas and 1000 μm particle velocity profiles for Mach 5 and 6 total temperature flow conditions.

Figures 45 and 46 show the internal particle temperature profiles for the 100 μm particles and 1000 μm particles, respectively, at the exit plane of the mixer-nozzle section (MN) and the exit plan of the isolator (IS). The temperature values are normalized by temperature at which they are initially inserted in the flow stream, T_{insert} , while the particle radius coordinate, r , is normalized by the particle outer radius, r_p . It is of interest that the 100 μm particle internal temperature profiles shift somewhat with the change in simulated Mach number in Figure 45, indicative of significant particle temperature change, but that the particle internal temperature profiles remain almost constant with the change in simulated Mach number for the 1000 μm particles shown in Figure 46. It is also evident, as expected, that the larger particles, with their larger thermal mass, sustain a larger thermal gradient at the particle surface.

Lastly, the effect of a relatively high particle mass fraction is examined in Figures 47 to 52. In Figure 47, the gas and particle temperature profiles for a case using a single 10 μm particle are compared to the gas and particle temperature profiles for a case wherein the flow contained a 1 percent mass fraction of 10 μm particles inserted into the flow at the same conditions as the single particles. The profiles are nearly identical for both the gas and particles. Figures 48 and 49 show a closer view of the nozzle exit and the ramp and isolator sections where a small difference in gas and particle temperatures is evident, however. After the same manner, the overall gas and particle velocity profiles are shown in Figure 50, with more detailed views given in Figures 51 and 52. Looking at these results, one must conclude that while some difference does exist in gas and particle properties due to the presence of a 1 percent mass fraction of particles, the differences are insignificant. Based on this result, no further 1 percent inert particle mass fraction simulations were performed.

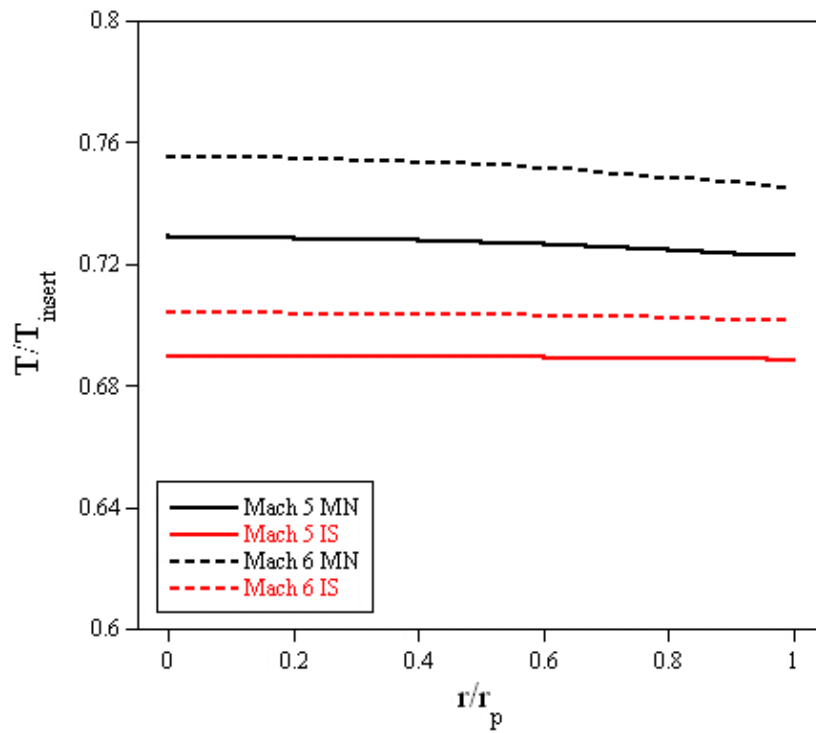


Figure 45.—Radial temperature profiles of 100 μm particles for the Mach 5 and 6 conditions at the exit planes of the mixer/nozzle (MN) and the isolator (IS).

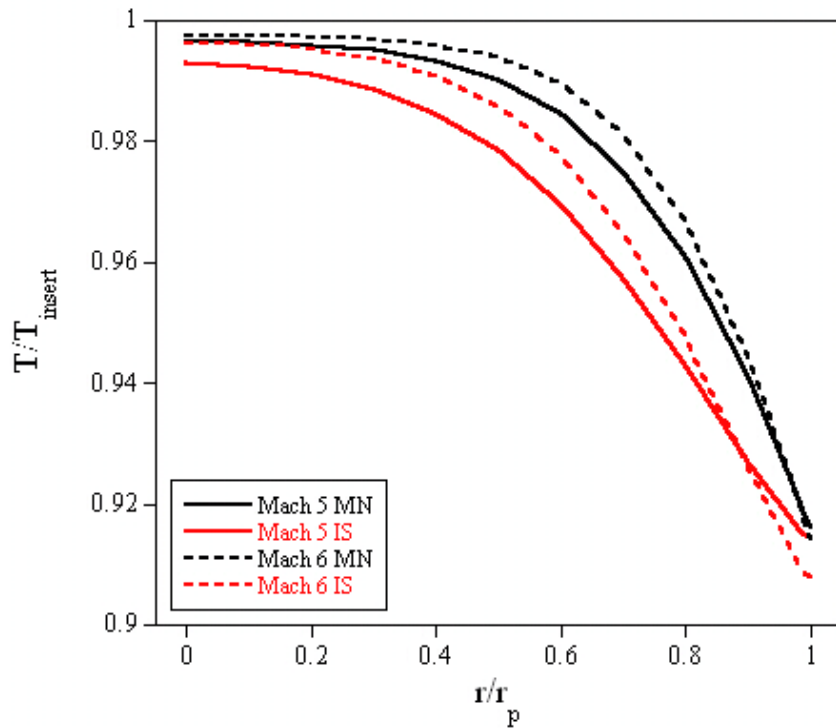


Figure 46.—Radial temperature profiles of $1000 \mu\text{m}$ particles for the Mach 5 and 6 conditions at the exit planes of the mixer/nozzle (MN) and the isolator (IS).

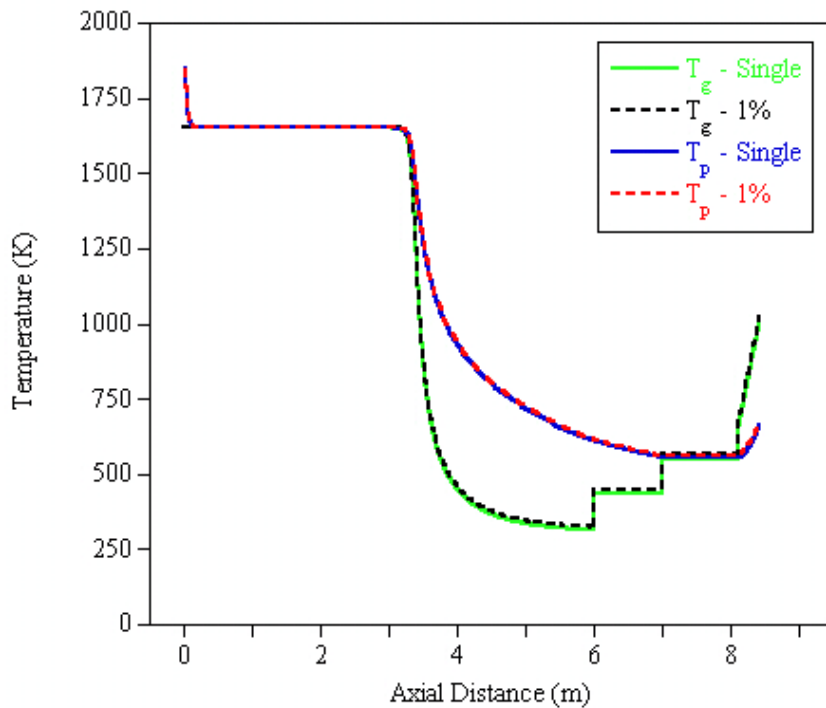


Figure 47.—Comparison of gas and particle temperature profiles for the Mach 6 total temperature flow condition for a single $10 \mu\text{m}$ particle and for a 1 percent $10 \mu\text{m}$ particle mass fraction.

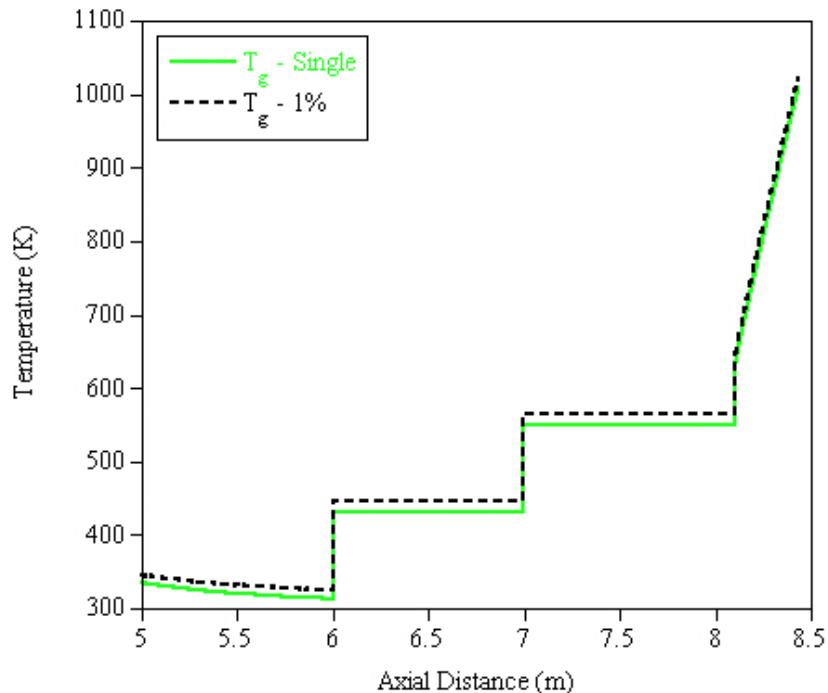


Figure 48.—Comparison of gas temperature profiles for the Mach 6 total temperature flow condition for a single 10 μm particle and for a 1 percent particle mass fraction of 10 μm particles over the last 1.0 m of the nozzle, the precompression plate, the final external compression ramp, and the isolator.

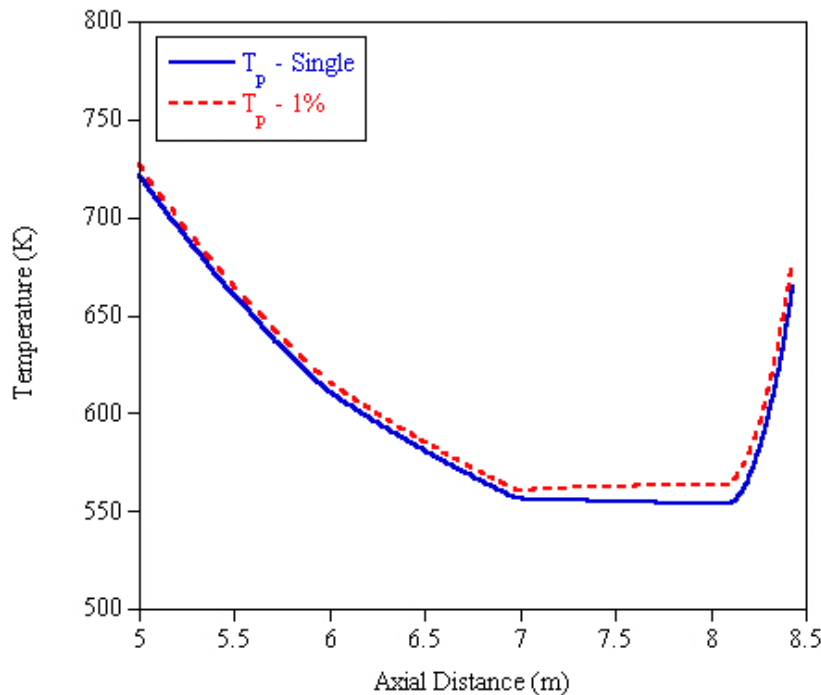


Figure 49.—Comparison of particle temperature profiles for the Mach 6 total temperature flow condition for a single 10 μm particle and for a 1 percent particle mass fraction of 10 μm particles over the last 1.0 m of the nozzle, the precompression plate, the final external compression ramp, and the isolator.

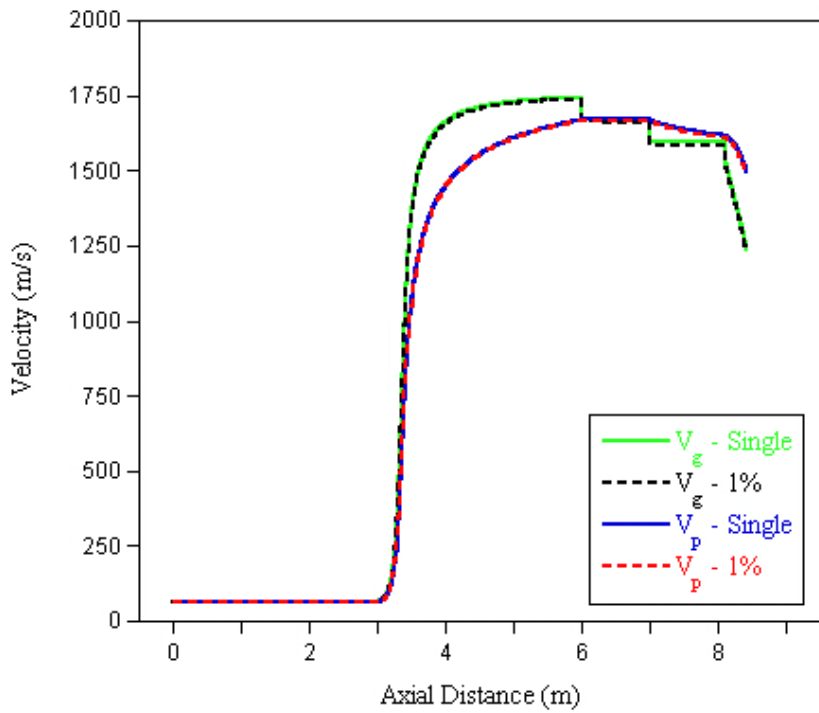


Figure 50.—Comparison of gas and particle velocity profiles for the Mach 6 condition for a single 10 μm particle and for a 1 percent 10 μm particle mass fraction.

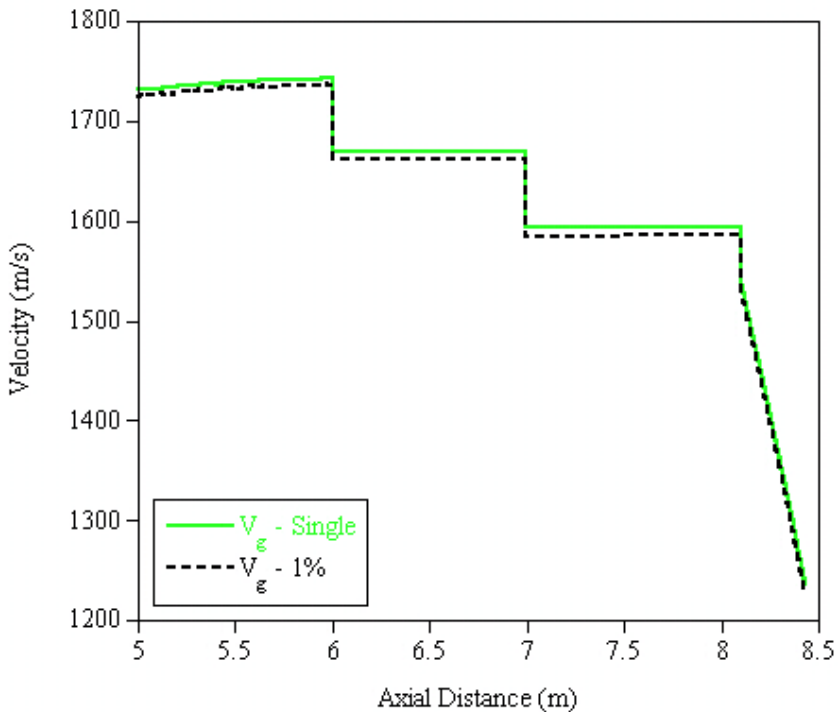


Figure 51.—Comparison of gas velocity profiles for the Mach 6 total temperature flow condition for a single 10 μm particle and for a 1 percent particle mass fraction of 10 μm particles over the last 1.0 m of the nozzle, the precompression plate, the final external compression ramp, and the isolator.

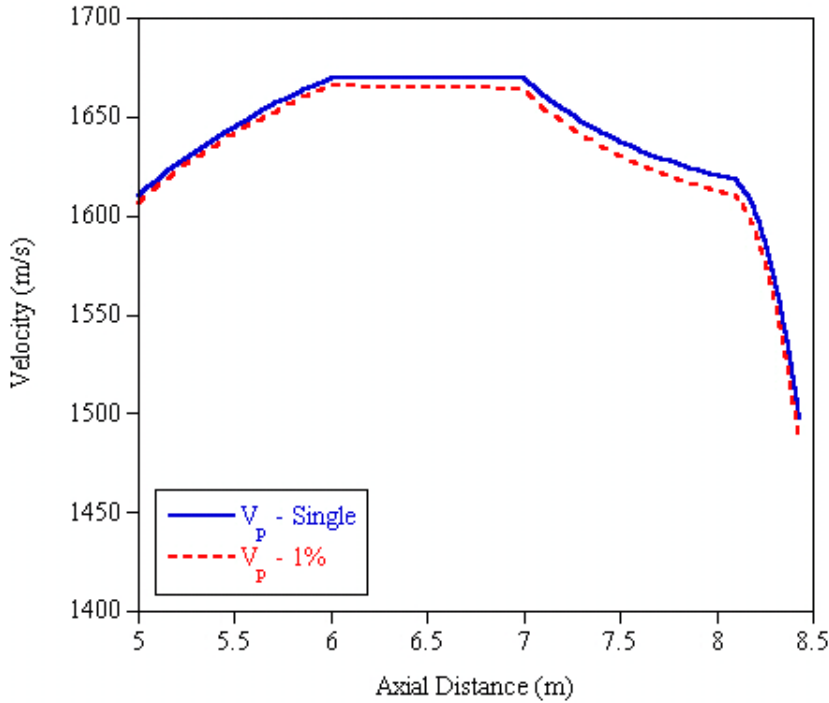


Figure 52.—Comparison of particle velocity profiles for the Mach 6 total temperature flow condition for a single 10 μm particle and for a 1 percent particle mass fraction of 10 μm particles over the last 1.0 m of the nozzle, the precompression plate, the final external compression ramp, and the isolator.

6.2 Single Graphite Particle Calculations

Using the kinetic and physical property information for graphite previously described, the Mach 5 and 6 total temperature single inert particle simulations were repeated using single graphite particles of the same particle diameters. For graphite the radiative emissivity is non-zero, so radiation heat transfer from the hot particles to the facility wall is included in each graphite particle simulation. A value for the emissivity of graphite of 0.9 was used (Pierson, 1993). Also, since the allowable temperature for graphite is considerably higher than that for alumina, Mach 7 total temperature simulations were performed for all three particle sizes. As with the inert particle cases, gas-phase finite rate chemistry was not used for the Mach 5 and 6 calculations. For the Mach 7 total temperature simulations, examination of gas-phase only calculations with and without finite-rate chemistry showed that significant mass fractions of minor species, particularly NO, were generated, as shown in Figure 53.

The formation of NO in turn had a measurable impact upon the O₂ and N₂ concentrations, as shown in Figure 54, which in turn had an effect on the static temperature, shown in Figure 55. Based on these results, the Mach 7 total temperature simulations were run with gas-phase finite-rate chemistry. In order to decrease computational time, those reactions given in Appendix B that include hydrogen-containing species were eliminated for these calculations, as there is no hydrogen in the system up through the isolator section.

One additional adjustment was made for the graphite particle calculations in comparison to the alumina particle calculations. For the alumina particles, an internal grid was used for both the 100 and 1000 μm diameter particles. However, the much higher thermal conductivity of graphite compared to alumina resulted in a Biot number for the 100 μm graphite particle below 0.1 during the entire particle trajectory. During the code validation portion of this study, it was shown that such low Biot numbers, particularly at high heat flux conditions, yielded lower accuracy heat transfer results. Therefore, the 100 μm graphite particle cases were run without an internal particle grid (i.e. with the whole particle at a single temperature).

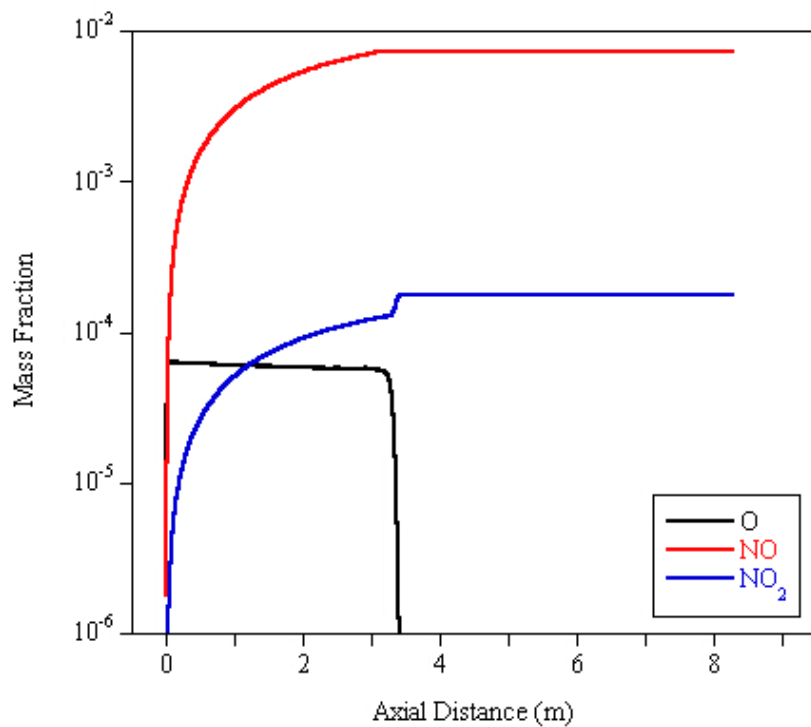


Figure 53.—Mass fractions of minor species from Mach 7 total temperature reacting flow simulation

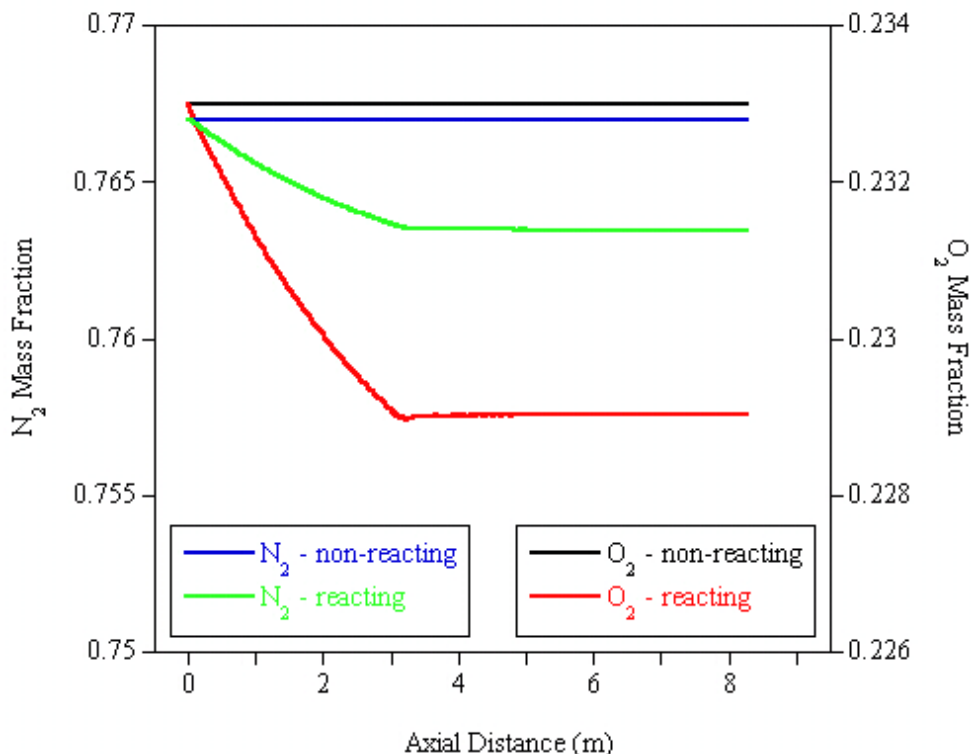


Figure 54.—Comparison of mass fractions of major species from Mach 7 total temperature simulations with and without finite-rate chemistry.

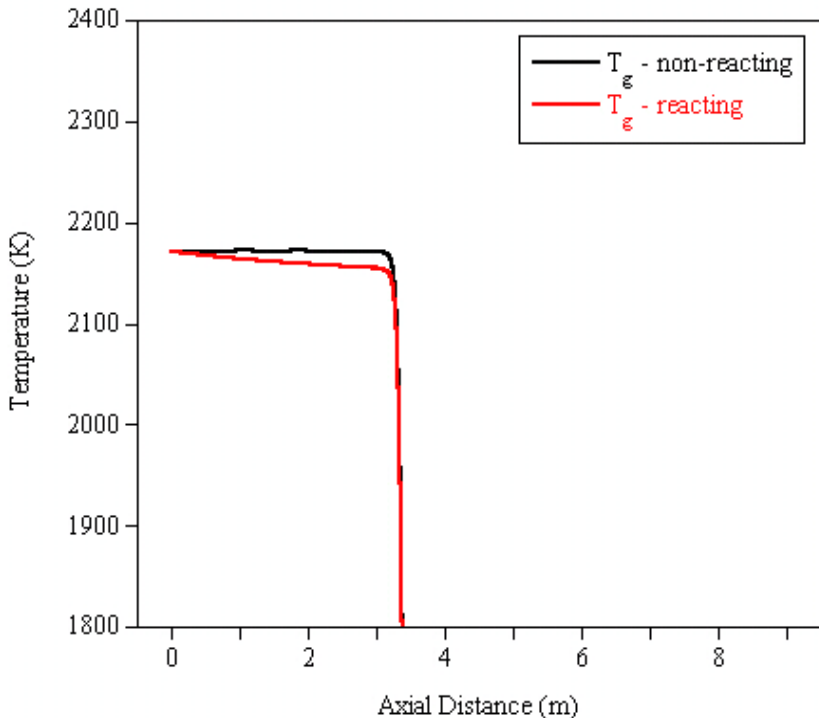


Figure 55.—Comparison of static temperature profiles from Mach 7 total temperature simulations with and without finite-rate chemistry.

Figures 56 and 57 show the particle temperature results for the Mach 5 and Mach 6 total temperature conditions, respectively, along with the corresponding inert alumina particle results for comparison. Figure 58 shows the temperature results for the Mach 7 condition that was not run for the inert particles. The 10 μm graphite particle is immediately quenched at the Mach 5 condition by the colder gas around it due to its high surface area to mass ratio leading to a high heat loss to the surroundings relative to the combustion heat addition at this condition, and stays quenched throughout the particle trajectory. The different thermal response compared to the 10 μm alumina particle in the nozzle is due to the differences in density, porosity, heat capacity, and thermal conductivity between the two materials. For the Mach 6 and 7 simulations, the 10 μm particle is consumed within a very short distance as the combustion heat addition is now much greater than the heat loss to the environment. The code does not contain a specific particle burnout model, and so the final phases of particle combustion may be somewhat inaccurate, but considering how rapidly the particle burns out, it is unlikely that a more accurate modeling approach would yield a substantially different result. For all cases, burnout is assumed to occur when the particle density reaches 1 percent of the initial particle density, at which point the particle is removed from the simulation.

The 100 μm graphite particles show similar behavior for the Mach 5, 6 and 7 total temperature conditions. In the constant-area low speed mixer, the first three meters, combustion is diffusion limited, as the particle and gas velocities are nearly identical. However, as the particle enters the convergent portion of the nozzle, a particle velocity lag is introduced, which greatly increases the transport of oxygen to the particle surface, and the temperature rapidly increases. The temperature rise then levels off, and for the Mach 6 case even drops off somewhat, based on the competing effects of lower free stream pressure in the nozzle leading to lower oxygen concentration, decreased particle mass due to combustion, increased particle internal surface area, heat transfer and combustion kinetics. For the Mach 7 total temperature condition, the particle burned out just after entering the convergent portion of the nozzle.

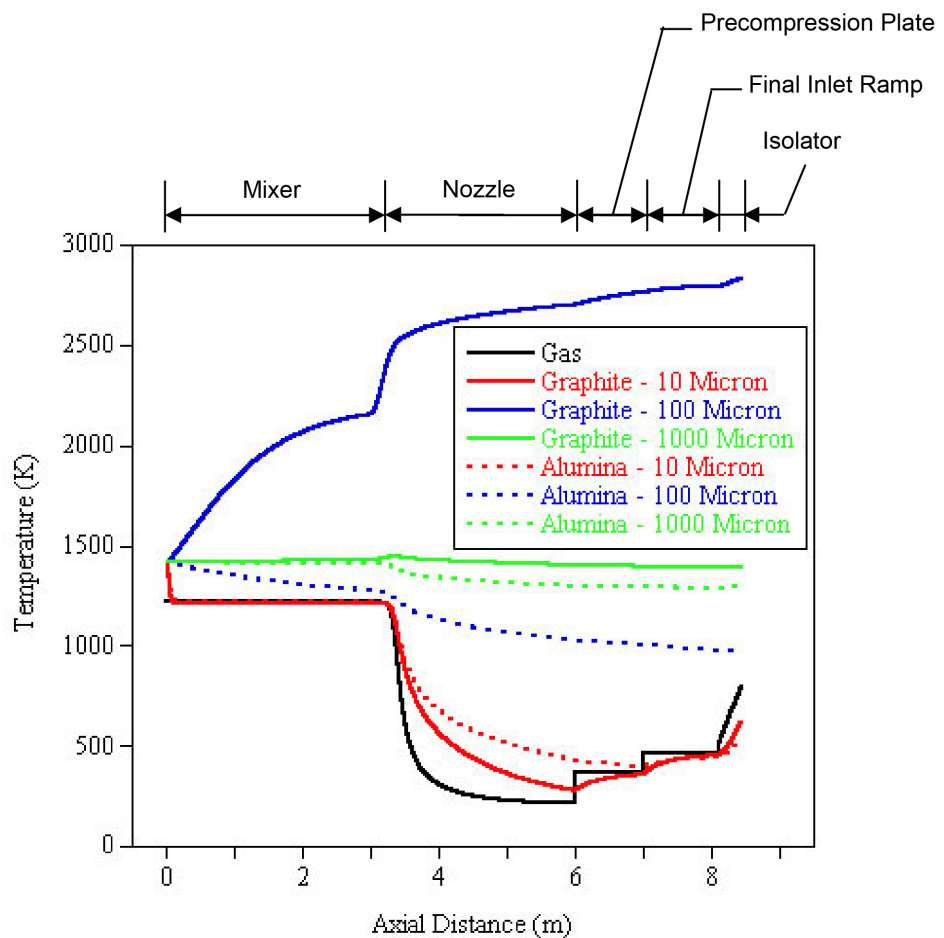


Figure 56.—Mach 5 graphite versus alumina surface temperature comparison.

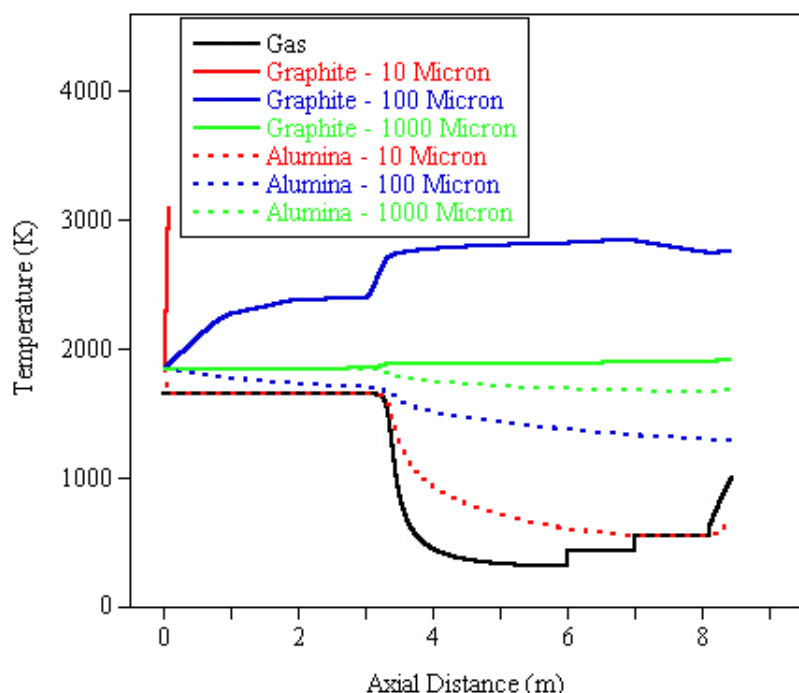


Figure 57.—Mach 6 graphite versus alumina surface temperature comparison.

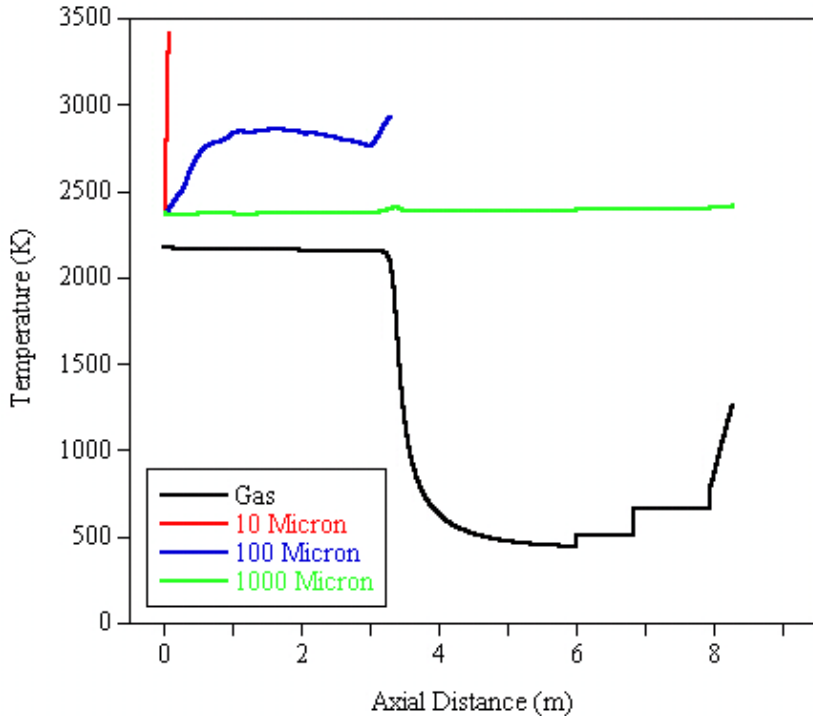


Figure 58.—Mach 7 surface temperature results.

The 1000 μm particles show very little temperature change at any of the three simulated Mach numbers due to their size. The relatively low external surface area to particle mass ratio of the 1000 μm particles decreases the impact of radiation and convective heat transfer on particle temperature. Simultaneously, intra-particle diffusion of oxygen and combustion products is greatly restricted, limiting combustion to the outer regions of the particle.

Figure 59 shows the internal particle temperature profiles for the 1000 μm particle at the exit plane of the mixer-nozzle section (MN) and the exit plan of the isolator (IS). The T/T_{insert} values above 1.0 are indicative of ongoing particle combustion.

Figures 60 to 62 show the velocity results for all three simulated Mach numbers and all three particle sizes, with the Mach 5 and Mach 6 results compared to their corresponding alumina particle cases. The Mach 6 and Mach 7 10 μm particle results are not readily discernable in these plots as the particles burn out so quickly that their trajectories do not differentiate themselves from the other cases. Since graphite is significantly less dense than alumina, it is not surprising to see that the graphite particles more closely follow the gas flow than the corresponding alumina particles do. This effect is accentuated due to mass loss from oxidation of the graphite particles, particularly for the 100 μm particles. In Figure 63, graphite particle porosity histories are given for each particle size and simulated Mach number. This plot shows that at each simulated Mach number, the 100 μm particles approach complete burnout, allowing the 100 μm graphite particles to respond much more quickly to changes in flow velocity than the corresponding alumina particles. The 1000 μm graphite particles lose a relatively small amount of mass traversing the domain in each case, and so behave similarly to the alumina particles, but reach a higher velocity due to the density difference.

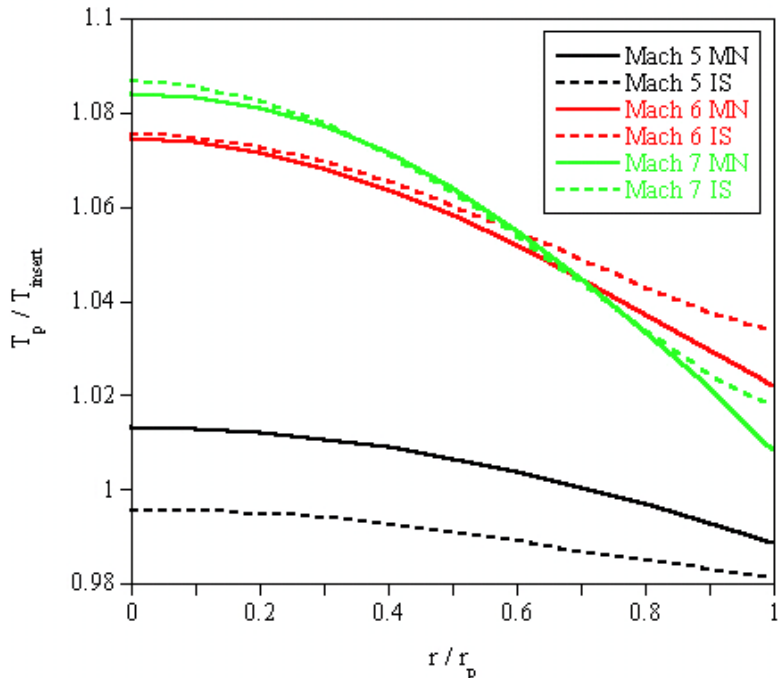


Figure 59.—Radial temperature profiles of the $1000 \mu\text{m}$ particle for the Mach 5, 6 and 7 conditions at the exit planes of the mixer/nozzle (MN) and the isolator (IS).

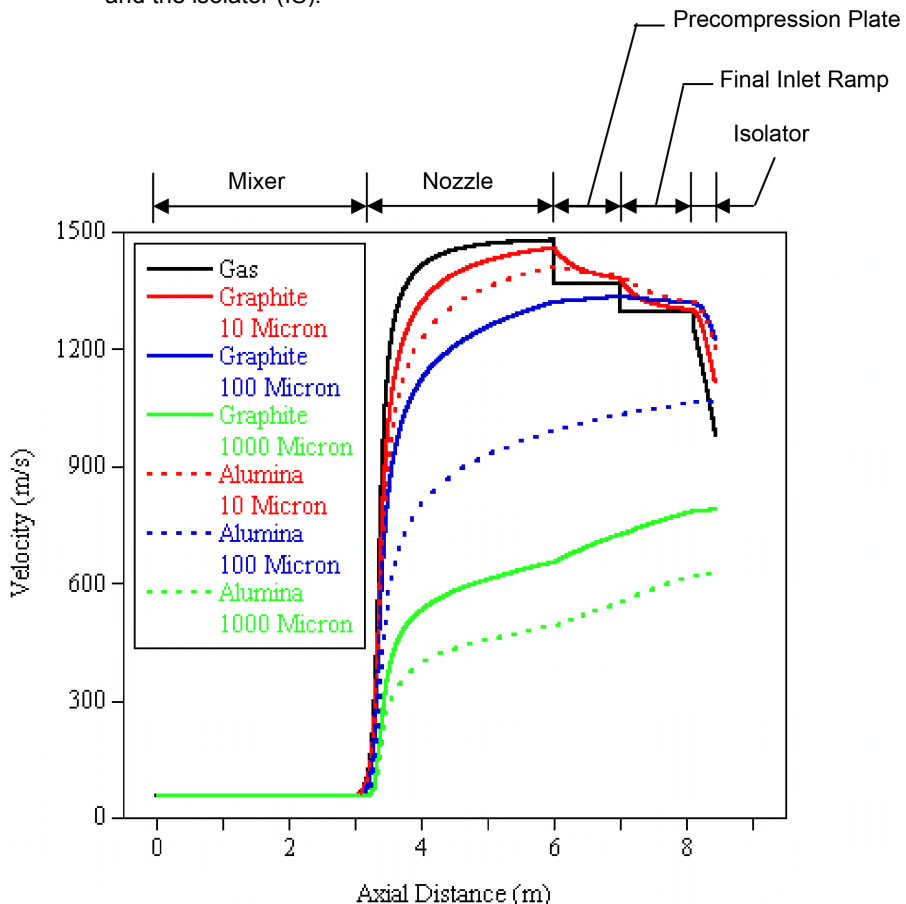


Figure 60.—Mach 5 graphite versus alumina velocity comparison.

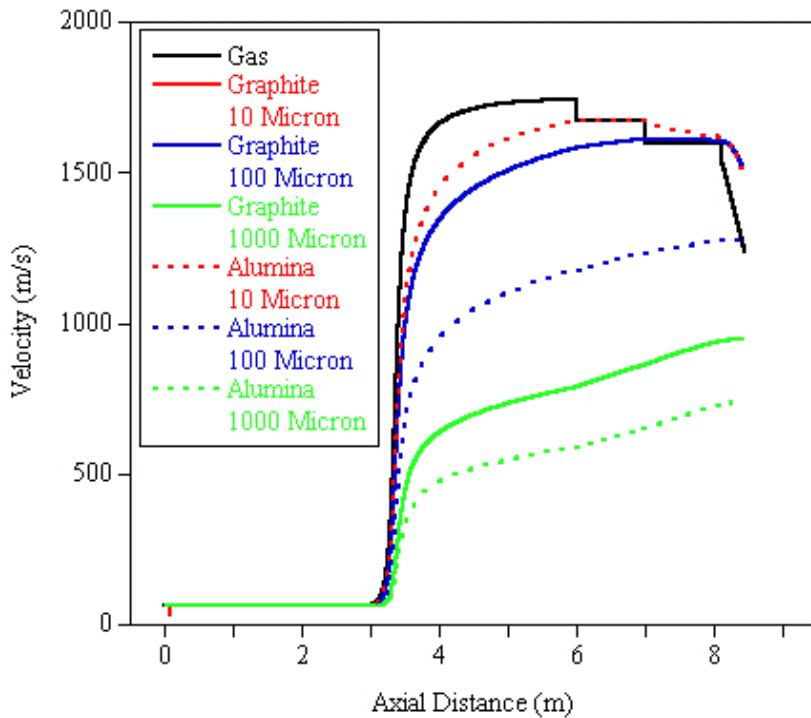


Figure 61.—Mach 6 graphite versus alumina velocity comparison.

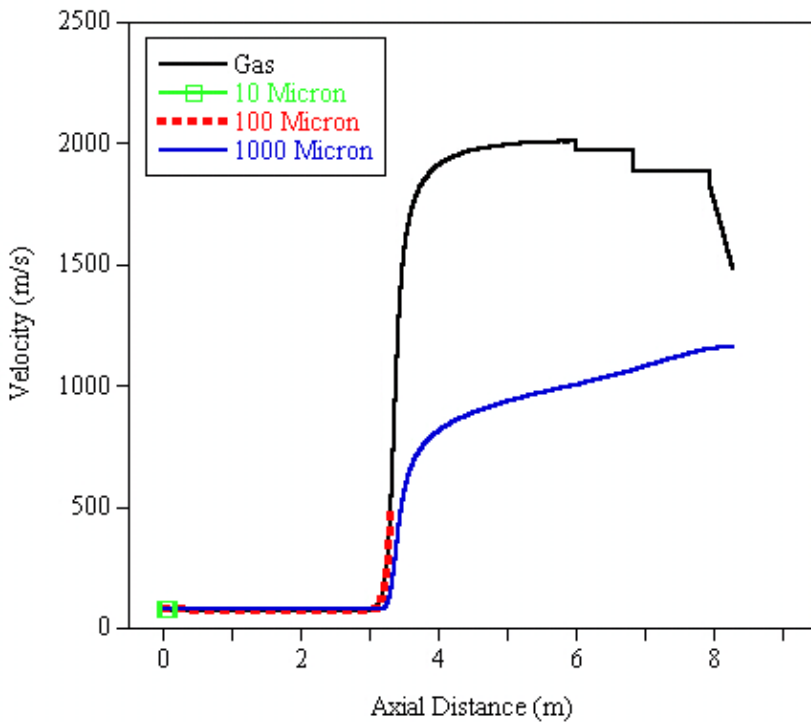


Figure 62.—Mach 7 velocity results.

It should be noted that for the 100 and 1000 μm graphite particles, the increase in porosity, corresponding to mass loss, does not increase as much as might be expected with simulated Mach number, despite the higher gas and particle temperatures. This is due to two causes. First, the particle

combustion is primarily diffusion limited throughout the particle trajectory. The higher temperature cases do not have significantly higher oxygen diffusion rates to and within the particle, so the mass loss cannot proceed at a much higher rate despite the increase in kinetic rate with temperature. Second, an increase in radiative heat transfer from the particle surface with increasing temperature tends to offset the internal heat generation from increased combustion rate.

To gain additional insight into the various factors effecting particle velocity and temperature profiles as a function of particle size, it is of interest to examine some additional parameters. Figure 64 give particle-gas relative Mach number (defined as $V_{\text{gas}} - V_{\text{particle}}$ divided by the local sound speed) data for all three particle sizes at the Mach 5 total temperature condition. The Mach 5 data was selected here because at the higher Mach numbers the 10 μm particle quickly burned out and therefore these values could not be compared throughout the particle trajectories. The relative Mach number traces shown in Figure 64 trend as expected, with the larger, heavier particles showing a larger velocity deficit. The 1000 μm particles have a supersonic relative Mach number through much of the nozzle, while the smaller particles never achieve a supersonic relative Mach number. While Mach number is generally defined as a scalar, for these Mach number calculations the relative Mach number is allowed to go negative when the particle velocity is greater than the gas flow velocity. Therefore, negative Mach numbers are shown in Figure 64, occurring in each case for the 10 μm particle after a shock jump-condition has been imposed on the gas flow and for the last two segments of the flowpath for the 100 μm particle.

Figures 65 to 67 show the different heat flows into, out of, and accumulating in the particle outer shell, as defined in Figure 3, for the three Mach 5 total temperature conditions. For the 10 and 100 μm particles, the “outer shell” actually encompasses the entire particle, since no internal grid was used. This means that the conduction term into or out of the outer shell is by definition zero, and is not shown. For the 1000 μm particle, a 101 point internal grid was used, so the outer shell has a thickness equal to 1 percent of the particle radius (5 μm). It should be noted that in these figures, some of the heat flow terms have been multiplied by 10 to make them visible on the scale of the plot.

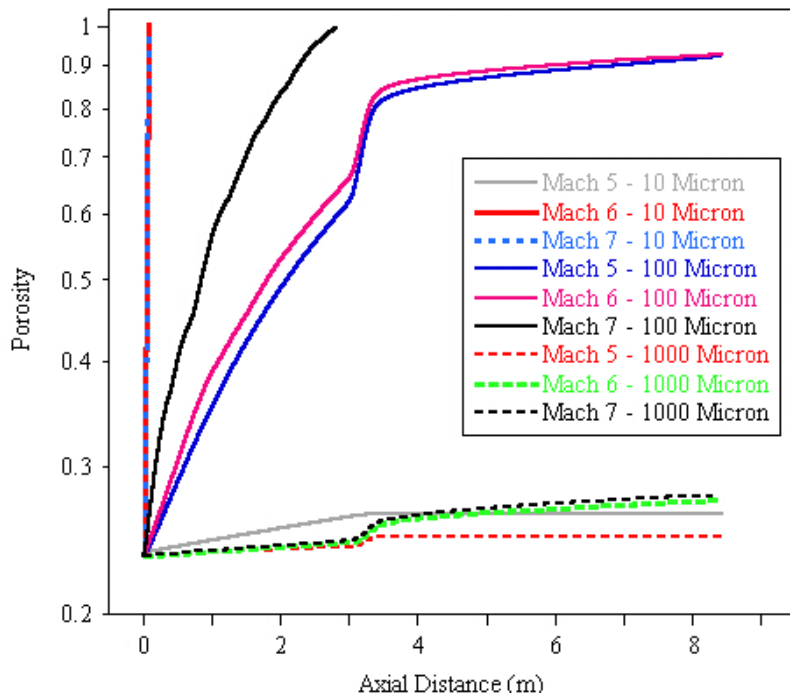


Figure 63.—Graphite particle porosity.

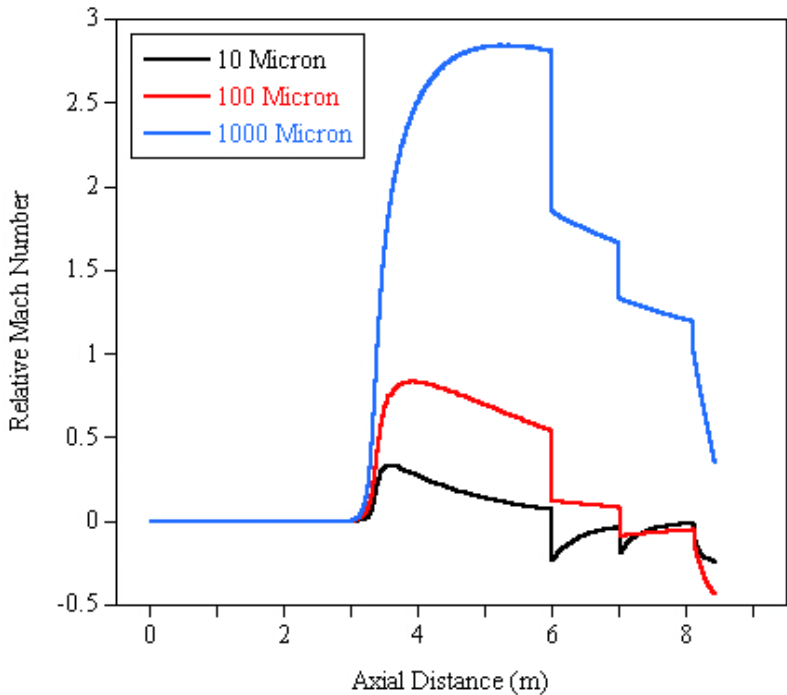


Figure 64.—Mach 5 gas-particle relative mach number.

Looking at Figure 65, heat flows for the $10 \mu\text{m}$ particle, we see high initial heat flow rates as the particle cools from the particle insertion temperature (200 K higher than the gas temperature) down to the gas temperature. The particle quickly reaches steady state within the mixer section, up to the 3.0 m point, and the heat flows stay constant until the particle enters the nozzle section. As the gas temperature drops in the nozzle, combustion is quenched and the particle radiation drops to zero. At the same time, convection spikes, removing heat from the particle as shown by the negative heat accumulation term. Finally, there is some particle heating across each of the oblique shocks and throughout the isolator section, located at approximately 6.0 m, 7.0 m, and 8.0 to 8.4 m, respectively.

For the $100 \mu\text{m}$ particle, Figure 66, we see that the combustion term is always larger than the convection heat loss term (convection out of the particle is defined as being positive, as is radiation), resulting in continuous particle temperature rise, as the radiation heat loss remains small. In the area of the isolator, the sum of the convection and radiation heat flows do approach the value of the combustion term, so the temperature remains fairly constant, as shown in Figure 56.

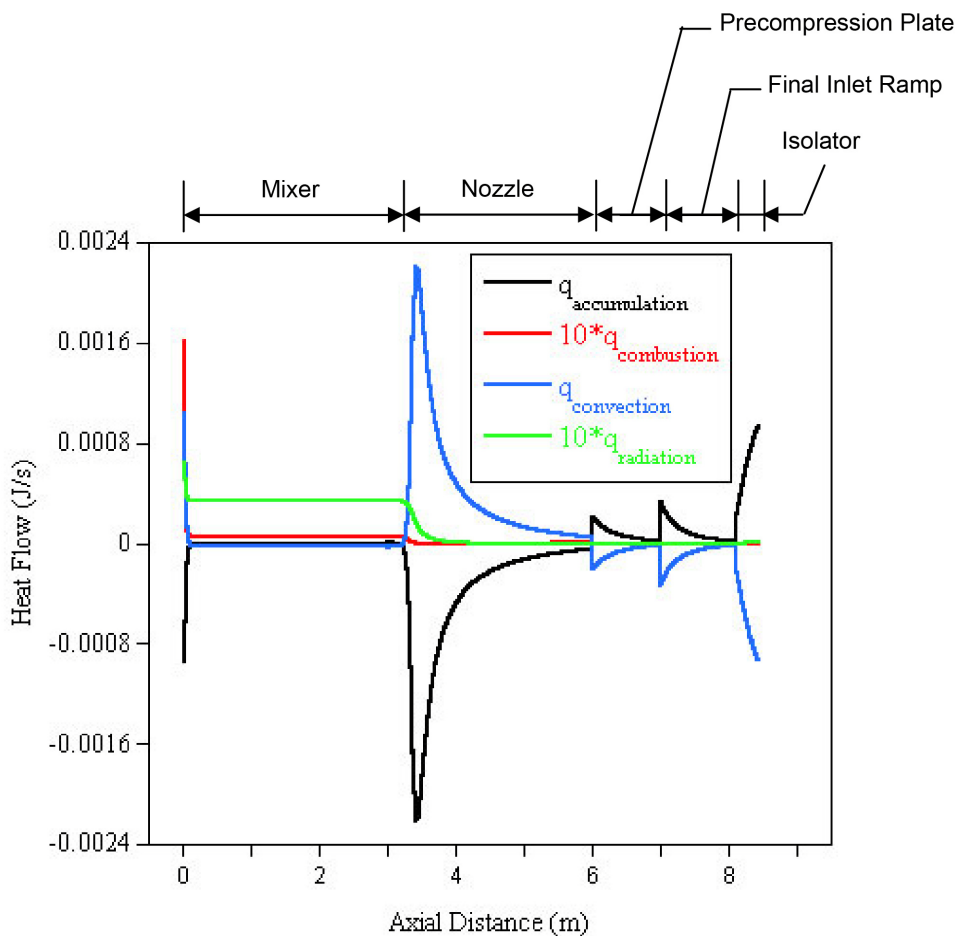


Figure 65.—Heat flows for 10 μm graphite particle at Mach 5 total temperature condition.

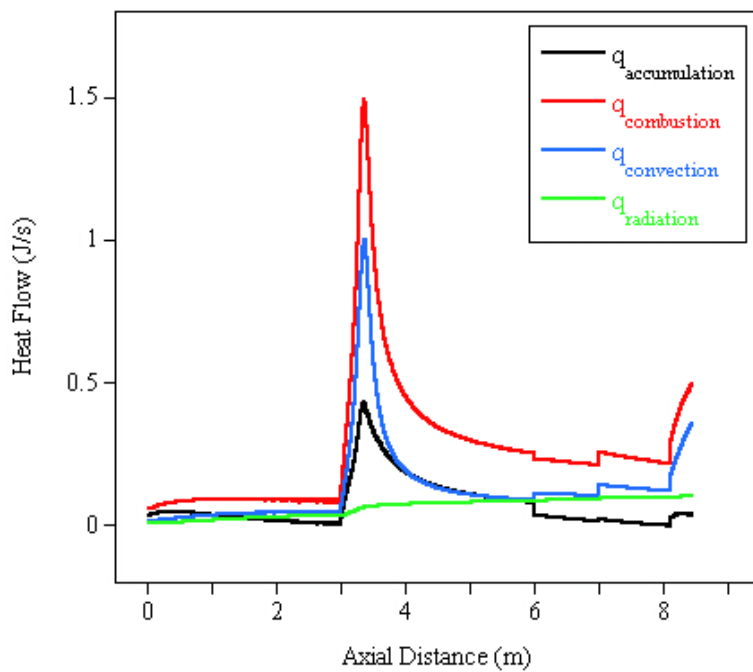


Figure 66.—Heat flows for 100 μm graphite particle at Mach 5 total temperature condition.

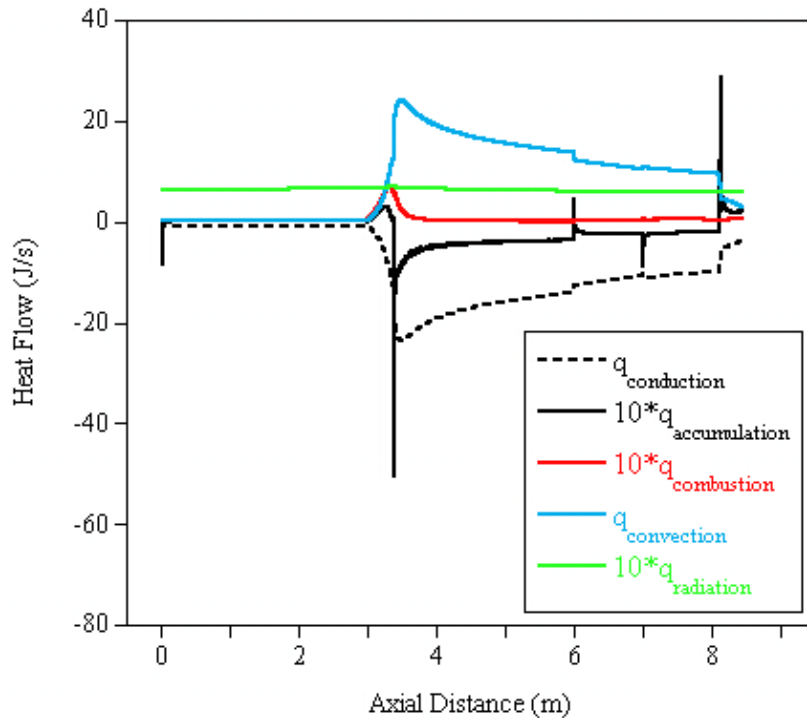


Figure 67.—Heat flows for 1000 μm graphite particle outer shell at Mach 5 total temperature condition.

Lastly, the heat flows (including internal conduction) for the 1000 μm graphite particle at the Mach 5 condition are given in Figure 67. As this particle's temperature changes very little throughout the simulation, we see that the radiative heat loss is essentially constant. As with the other particle sizes, the convection term increases rapidly entering the nozzle, but the actual change in particle temperature is small because of the large thermal mass represented by this relatively large particle. The ramp shocks and isolator section are discernible in Figure 67, but have only a very minor effect on the particle temperature profile.

6.3 One Percent Mass Fraction Graphite Particle Simulations

The same simulations that were run for the inert particles and the single graphite particles were then run using a 1 percent mass fraction of graphite particles. All of the 1 percent mass fraction simulations were run using finite rate chemistry in the gas phase. As in the Mach 7 single graphite particle simulations, the hydrogen-containing species were eliminated from the kinetic mechanism to speed the calculations. Each 1 percent mass fraction simulation was run until a time invariant solution was obtained for both the particle and gas streams.

Figures 68 to 76 show the temperature and velocity histories of 10, 100, and 1000 μm graphite particles and the corresponding gas stream solutions calculated using a 1 percent mass fraction of particles at each of the three simulated Mach numbers. These figures also contain the single graphite particle results for comparison.

For the 10 μm particles at the Mach 5 total temperature flow condition, Figure 68, there is virtually no difference between the single particle case and the 1 percent mass fraction case. Since combustion of the particle is almost immediately quenched by the cooler surrounding gas, there is no impact on the gas stream that could cause a change in the overall solution. The insertion into the gas stream of a 1 percent

ass fraction of particles at a temperature 200 K higher than the gas stream is insufficient to cause a significant change in the gas stream variables, as was observed with the inert alumina particles. At the Mach 6 and Mach 7 total temperature flow conditions, Figures 69 and 70, the 10 μm graphite particles undergo very rapid combustion. The heat release from the particles significantly raises the gas stream temperature in the mixer. This increase in mixer temperature results in an increased isolator exit temperature, as well as increased velocity in sections of the flow path. The increase in velocity is due to an increase in the sound speed due to the higher static temperature in regions of approximately constant Mach number. The somewhat lower relative temperature increase in the Mach 7 case, Figure 70, is due primarily to the increase in gas specific heat with increasing temperature.

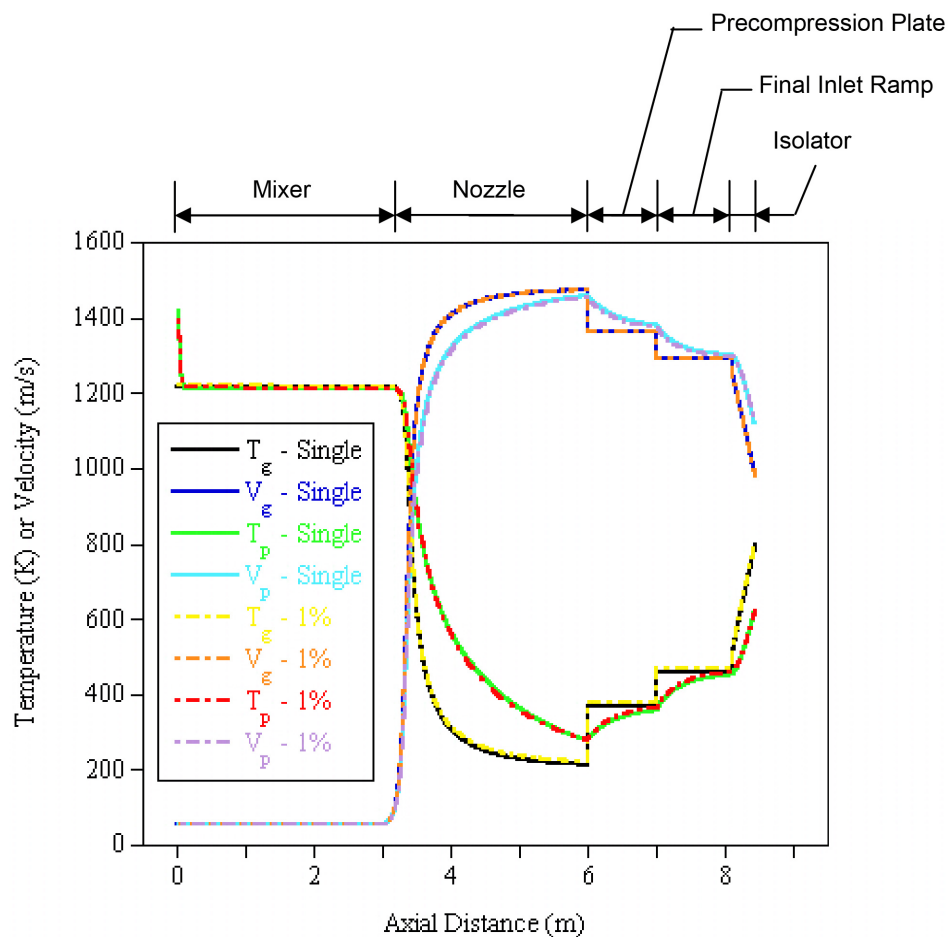


Figure 68.—Comparison of particle temperature and velocity profiles between a single 10 μm graphite particle and a 1 percent mass fraction of 10 μm graphite particles at the Mach 5 total temperature flow condition.

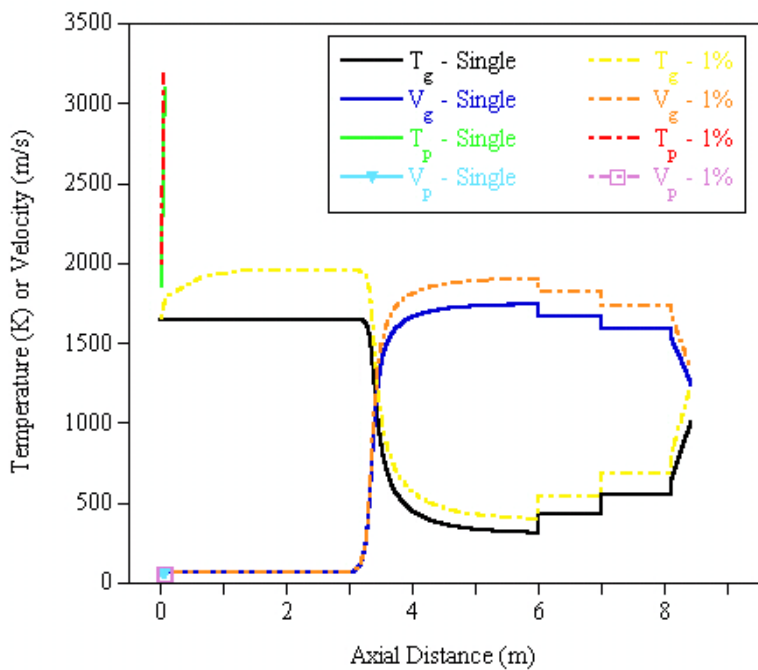


Figure 69.—Comparison of particle temperature and velocity profiles between a single 10 μm graphite particle and a 1 percent mass fraction of 10 μm graphite particles at the Mach 6 total temperature flow condition.

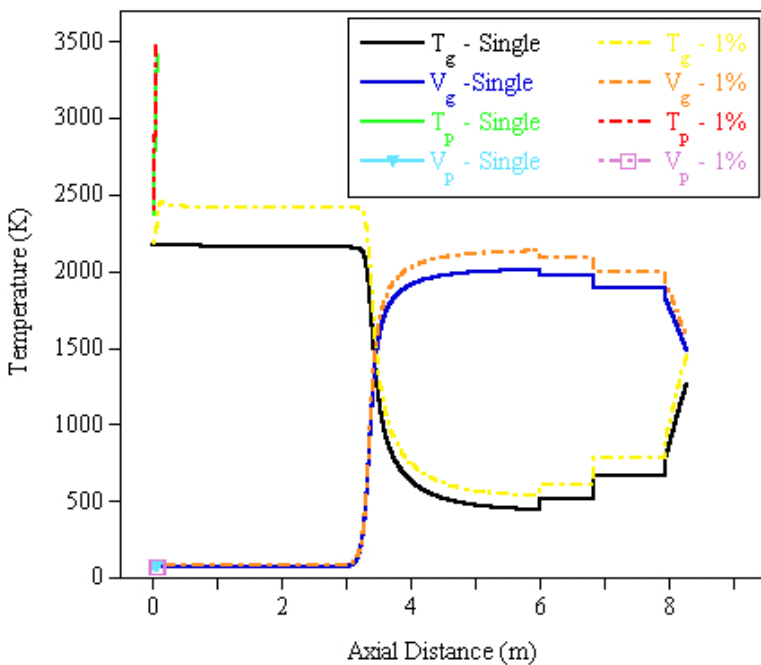


Figure 70.—Comparison of particle temperature and velocity profiles between a single 10 μm graphite particle and a 1 percent mass fraction of 10 μm graphite particles at the Mach 7 total temperature flow condition.

Comparing the results for the Mach 5 and Mach 6 total temperature flow condition for the 100 μm particles, Figures 71 and 72, similar results are observed. While the single particles do not burn out within the computational domain, the higher gas temperature for the 1 percent mass fraction simulations from graphite combustion leads to more rapid particle consumption and eventual burnout. As would be expected, the particles burn out more rapidly at the higher Mach 6 total temperature condition.

Some unique features are visible in the Mach 7 results for the 100 μm graphite particles, as shown in Figure 73. Here the single graphite particle and the 1 percent graphite particle stream burn out at approximately the same point. This occurs despite the increasing gas temperature found in the 1 percent mass fraction results. This occurs because at this very high temperature condition the combustion process is completely diffusion limited. Increasing the gas temperature does not translate into a higher particle combustion rate.

Lastly, in Figures 74 to 76, little difference is observed between the single particle solutions and the 1 percent mass fraction solutions for the 1000 μm particles at each of the three simulated Mach numbers. Since relatively little combustion is occurring in these cases, the gas streams are unaffected by the presence of the 1 percent mass fraction of particles.

Figures 77 to 79 show the particle porosity histories for the single graphite particles and the 1 percent mass fraction graphite particle stream as a function of particle size and simulated Mach number.

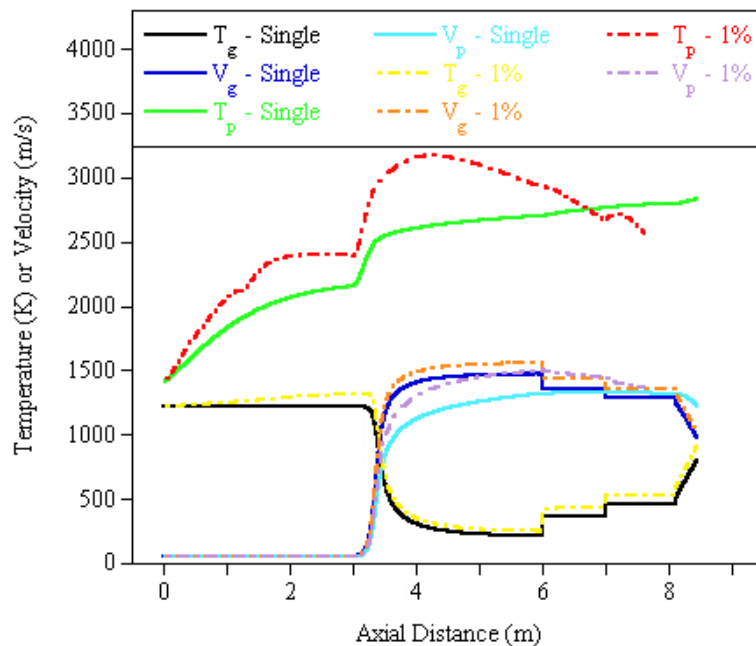


Figure 71.—Comparison of particle temperature and velocity profiles between a single 100 μm graphite particle and a 1 percent mass fraction of 100 μm graphite particles at the Mach 5 total temperature flow condition.

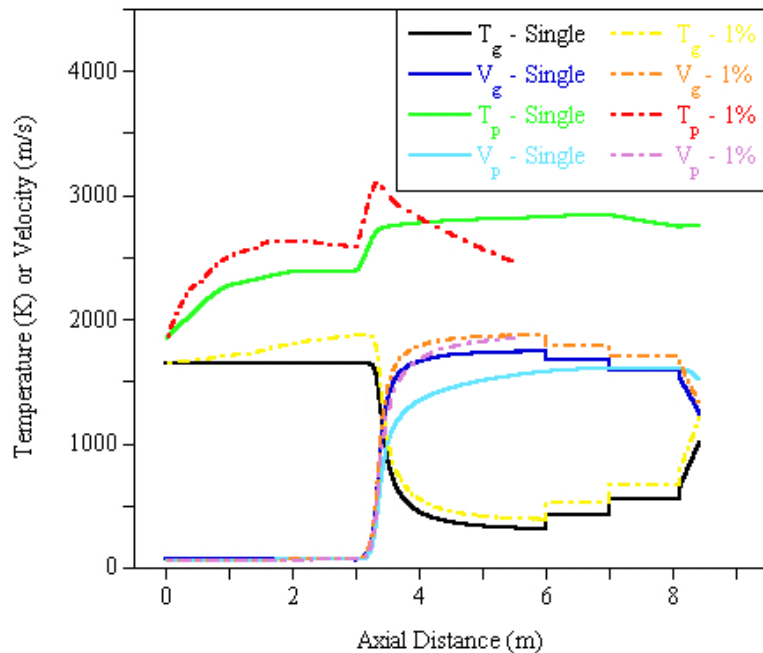


Figure 72.—Comparison of particle temperature and velocity profiles between a single 100 μm graphite particle and a 1 percent mass fraction of 100 μm graphite particles at the Mach 6 total temperature flow condition.

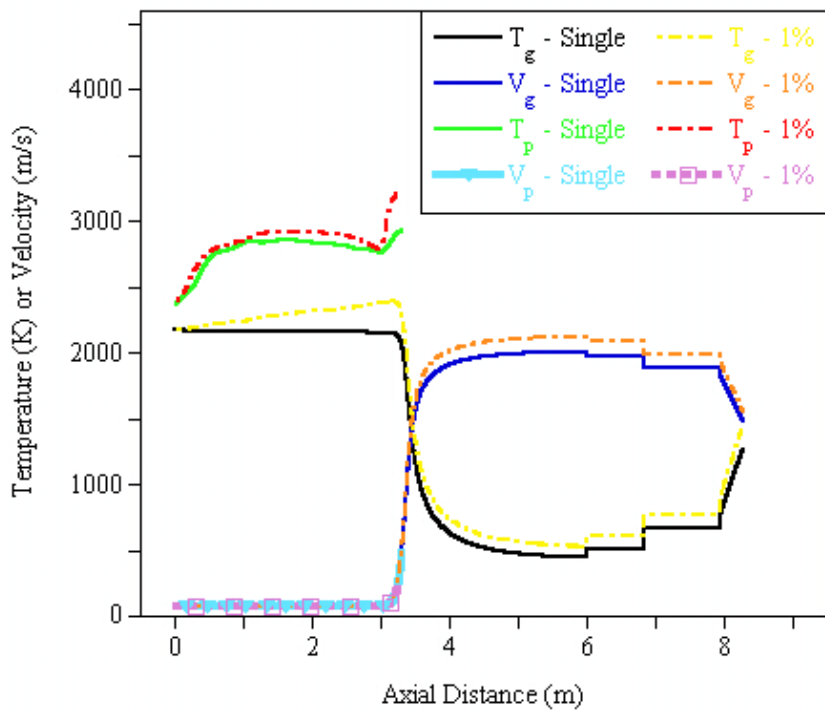


Figure 73.—Comparison of particle temperature and velocity profiles between a single 100 μm graphite particle and a 1 percent mass fraction of 100 μm graphite particles at the Mach 7 total temperature flow condition.

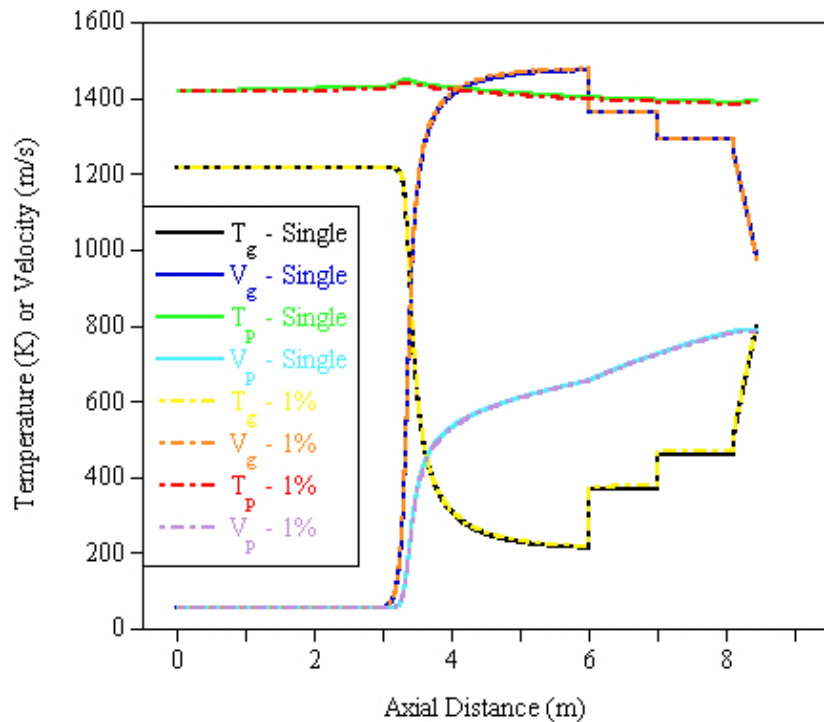


Figure 74.—Comparison of particle temperature and velocity profiles between a single 1000 μm graphite particle and a 1 percent mass fraction of 1000 μm graphite particles at the Mach 5 total temperature flow condition.

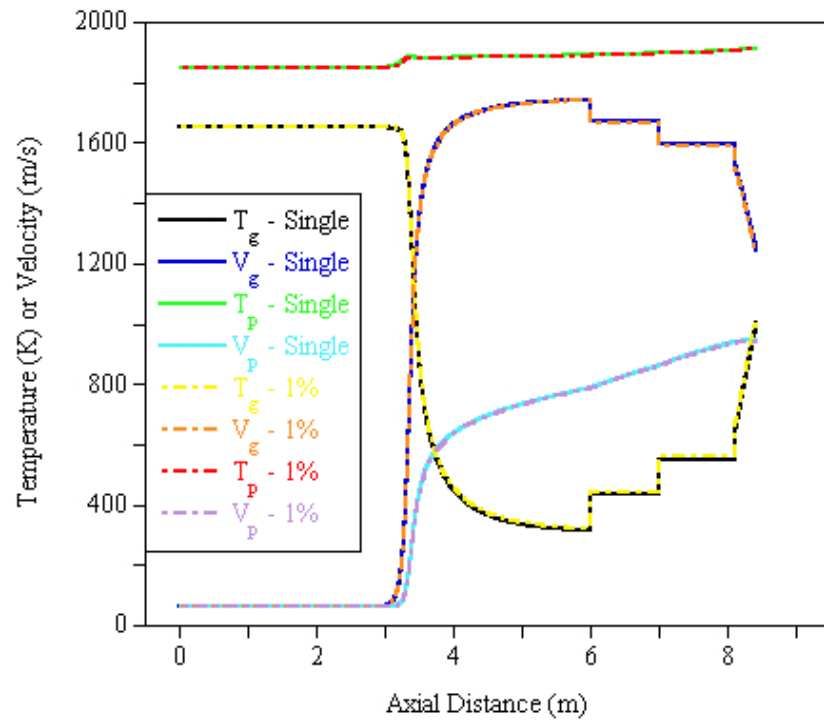


Figure 75.—Comparison of particle temperature and velocity profiles between a single 1000 μm graphite particle and a 1 percent mass fraction of 1000 μm graphite particles at the Mach 6 total temperature flow condition.

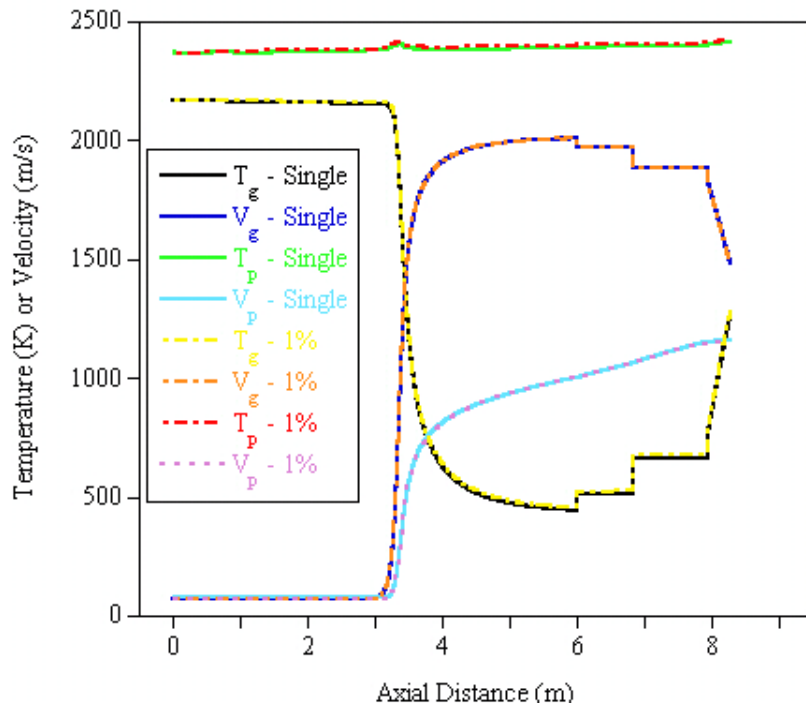


Figure 76.—Comparison of particle temperature and velocity profiles between a single 1000 μm graphite particle and a 1 percent mass fraction of 1000 μm graphite particles at the Mach 7 total temperature flow condition.

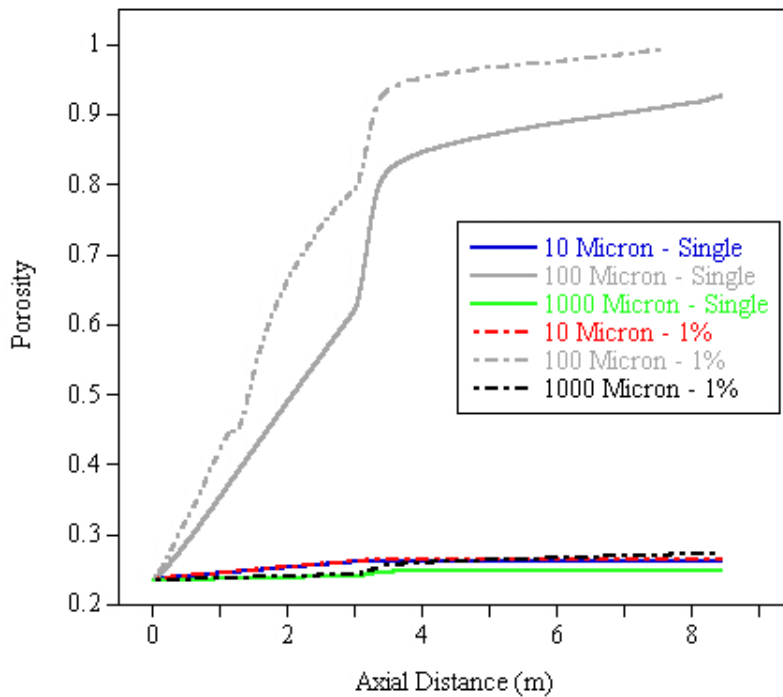


Figure 77.—Comparison of particle porosity profiles between single graphite particles and a 1 percent mass fraction of graphite particles at the Mach 5 total temperature flow condition.

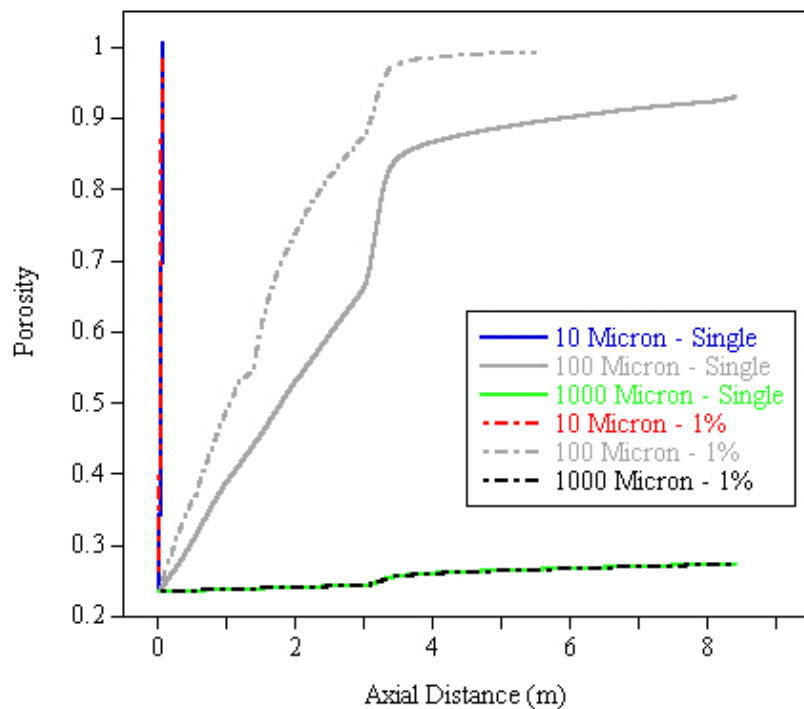


Figure 78.—Comparison of particle porosity profiles between single graphite particles and a 1 percent mass fraction of graphite particles at the Mach 6 total temperature flow condition.

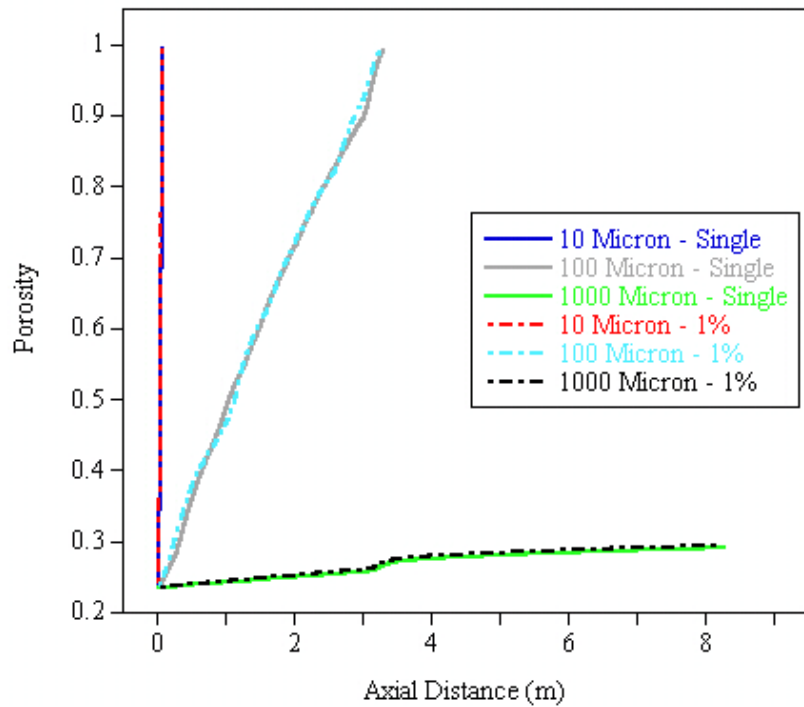


Figure 79.—Comparison of particle porosity profiles between single graphite particles and a 1 percent mass fraction of graphite particles at the Mach 7 total temperature flow condition.

Figure 80 shows the NO mass fraction profile for all the 1 percent graphite particle mass fraction cases where NO is produced above a mass fraction of 1×10^{-6} at any point in the computational domain. All of the Mach 5 total temperature flow condition cases and the Mach 6 total temperature flow condition case with no particles have NO levels below this threshold. The Mach 6 cases with particles all have very low NO mass fractions which only make it above the 1×10^{-6} mass fraction threshold because of particle combustion. However, all of the Mach 7 simulations have significant mass fractions of NO. The NO is generated by the high temperature in the mixing section, particularly when enhanced by particle combustion. The NO level decreases as the temperature drops with expansion, but the NO reactions are eventually “frozen” in the expansion section of the nozzle due to the rapid temperature drop along with relatively slow nitrogen chemistry. Looking at Figures 81 and 82, the NO₂ and O mass fraction profiles, it is evident that a small mass fraction of O is generated by the high temperatures in the mixing section in addition to the NO, and that this atomic oxygen combines with the NO to produce NO₂ during the expansion just upstream and downstream of the nozzle throat. These NO₂ mass fractions are then also “frozen” as they progress downstream. Prominent in Figure 81 is a spike in the NO₂ mass fraction early in the mixer for the 100 μm graphite particles at the Mach 7 total temperature flow condition. This spike represents a region wherein the kinetics favors the formation of NO₂ from the NO and O formed at the initial high temperature. As the temperature increases due to graphite combustion, the kinetics transitions to favor the formation of NO and O instead of NO₂, and the NO₂ previously formed dissociates back to NO and O. In general, it can be concluded from these figures that the more rapid the particle combustion process, the higher the levels of NO and O that are generated, and therefore an increased mass fraction of NO₂ is generated in the expansion.

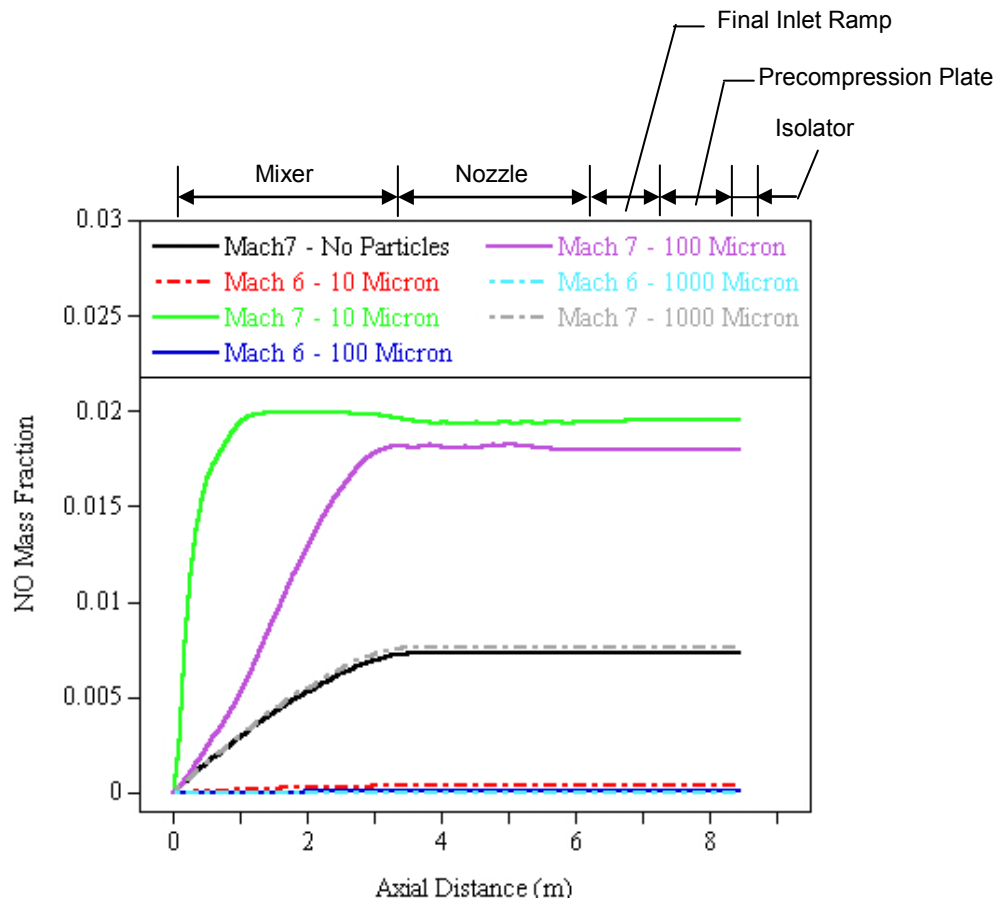


Figure 80.—Comparison of NO mass fraction profiles between no graphite particles and a 1 percent mass fraction of graphite particles.

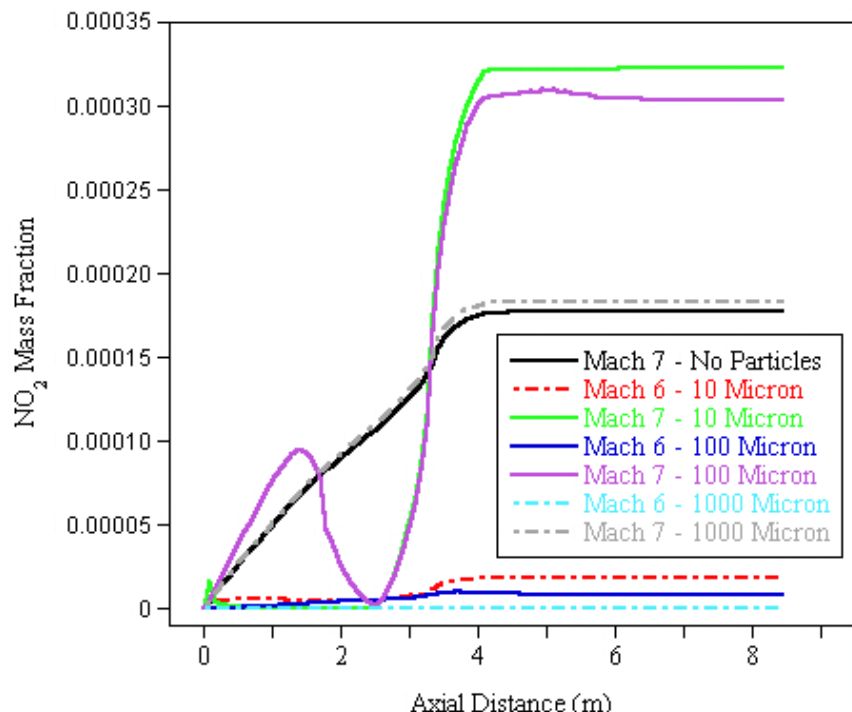


Figure 81.—Comparison of NO₂ mass fraction profiles between no graphite particles and a 1 percent mass fraction of graphite particles.

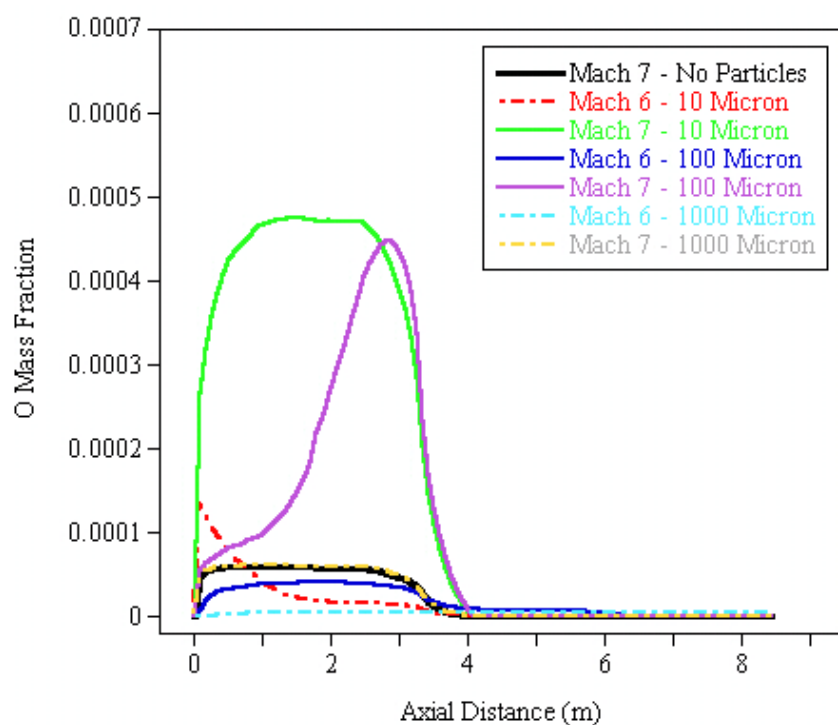


Figure 82.—Comparison of O mass fraction profiles between no graphite particles and a 1 percent mass fraction of graphite particles.

Figures 83 and 84 show the spatial distribution of CO₂ and CO, respectively. As expected, the combinations of particle size and simulated Mach number that yield little or no particle combustion show low levels of CO₂ and CO. This would include all the 1000 μm particle cases and the Mach 5, 10 μm particle case. Low temperature graphite combustion favors CO production at the particle surface and inhibits CO oxidation in the gas phase, as seen with the Mach 5 total temperature, 100 μm graphite particle case. As the temperature increases due to more rapid graphite combustion, such as with the Mach 6 total temperature, 10 and 100 μm particle cases, CO is initially produced by the particle, but this transitions to CO₂ production with rising particle temperature. With increasing gas phase temperature, the CO is oxidized to CO₂. This gas phase CO oxidation takes much longer for the slower burning Mach 6, 100 μm particle case, and is not completed before the nozzle expansion lowers the flow temperature. At that point, CO production is again favored over CO₂ at the particle surface, and the CO level rises through the nozzle. This rise in the CO mass fraction for the Mach 6, 100 μm case in the nozzle is also contributed to by a small amount of CO₂ dissociation, as indicated by the drop in CO₂ concentration in Figure 83.

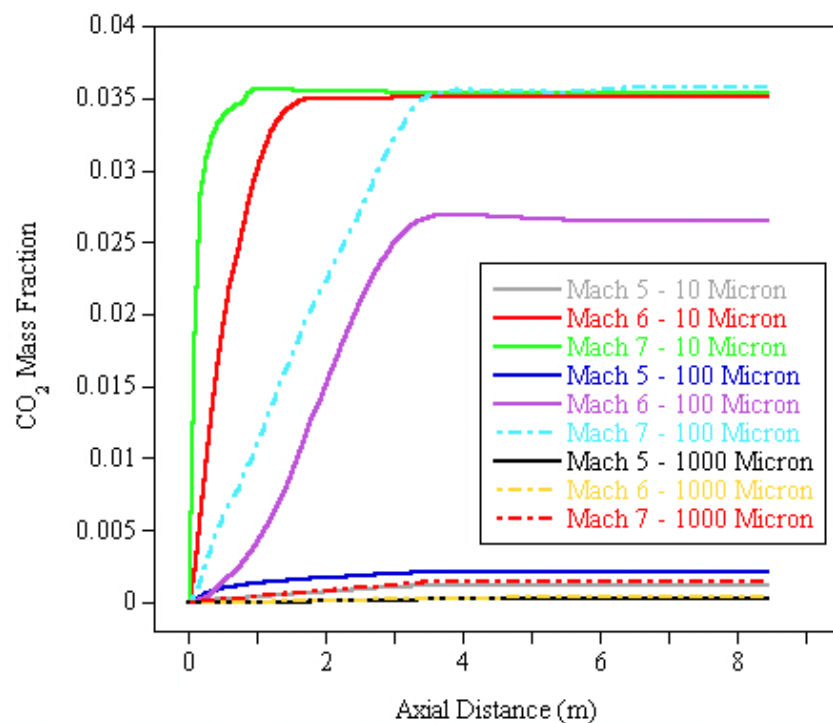


Figure 83.—Comparison of CO₂ mass fraction profiles between 1 percent graphite particle mass fraction cases.

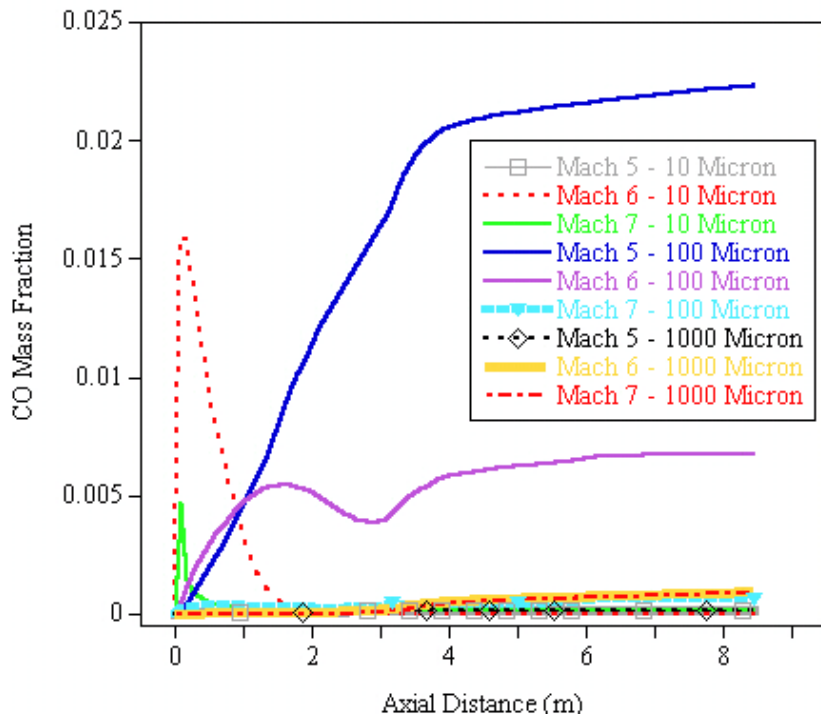


Figure 84.—Comparison of CO mass fraction profiles between 1 percent graphite particle mass fraction cases.

6.4 Ignition Calculations

As a final step in examining the effect of graphite particulate vitiation on hypersonic propulsion testing, a series of ignition delay calculations were performed based on the isolator section exit flow conditions for each 1 percent graphite particle mass fraction case. Hydrogen was used as the fuel at an equivalence ratio of 0.8 based upon the amount of molecular oxygen present at the exit of the isolator. The computational domain generally consisted of a constant area duct 0.5 meters long, open at each end. 450 equally spaced grid points were used in each model. In some cases the length of the domain was extended to 1.0 m if ignition did not occur within the 0.5 m length. A supersonic inlet boundary condition was used with the pressure, temperature, velocity, and species mass fractions taken from the isolator exit conditions, as given in Tables 6 and 7. If particles were present at the isolator exit, they were included in the ignition delay calculation at their isolator exit condition, Table 8, and were allowed to continue to react based on the local flow conditions. The exit boundary conditions remained supersonic for each case. The initial condition within the duct was 100 percent N₂ at the temperature, pressure, and velocity of the isolator exit. Pure nitrogen gas was used as the initial condition for the calculation to help distinguish the location of the interface between the gas coming from the in-flow boundary versus and the gas initially in the duct for this plug-flow simulation. Ignition was defined as the point in time when a 200 K temperature rise above the inlet boundary condition was observed within the computational domain. Figure 85 shows a typical result at the point of ignition.

TABLE 6.—GAS TEMPERATURES (K) AT THE EXIT OF THE ISOLATOR SECTION

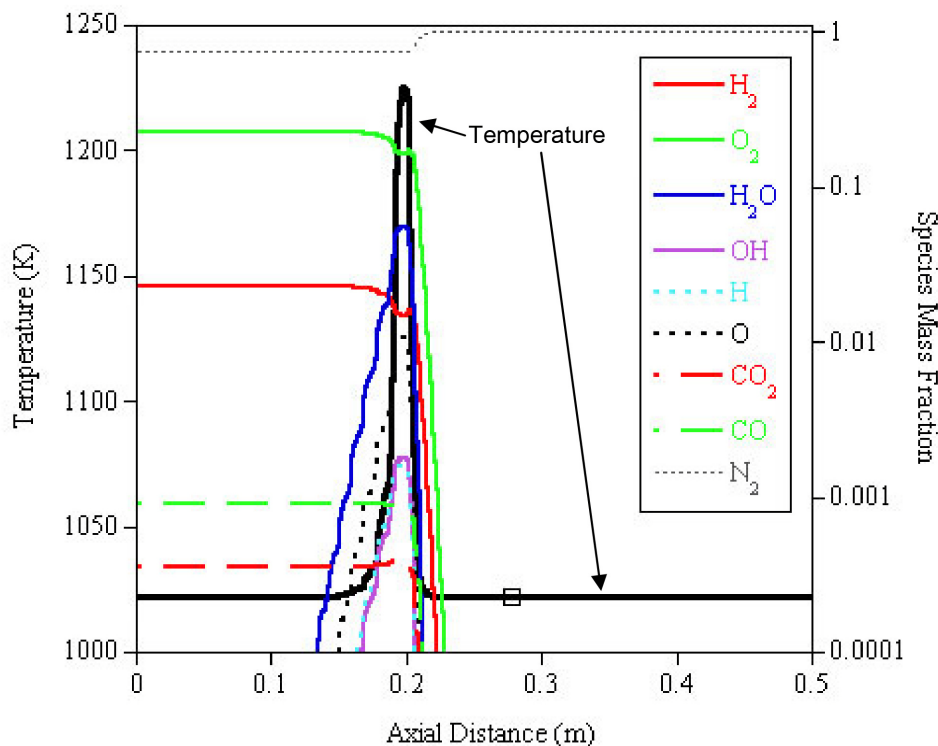
Mach no.	No particles	10 μm	100 μm	1000 μm
5	798	800	908	802
6	1008	1229	1201	1022
7	1264	1452	1441	1278

TABLE 7.—SPECIES MASS FRACTIONS AT THE EXIT OF THE ISOLATOR SECTION

Mach no./particle size	O ₂	N ₂	NO	NO ₂	CO ₂	CO	O
5 / None	0.233000	0.767000	-----	-----	-----	-----	-----
6 / None	0.233000	0.767000	-----	-----	-----	-----	-----
7 / None	0.229035	0.763448	0.007340	0.000177	-----	-----	-----
5 / 10	0.232141	0.766549	-----	-----	0.001175	0.000135	-----
6 / 10	0.207284	0.757233	0.000347	0.000018	0.035111	0.000007	-----
7 / 10	0.196415	0.743837	0.019493	0.000323	0.035401	0.000141	-----
5 / 100	0.218665	0.756865	-----	-----	0.002132	0.022322	0.000016
6 / 100	0.209855	0.756875	0.000084	0.000008	0.026443	0.006705	-----
7 / 100	0.196023	0.744401	0.017977	0.000304	0.035747	0.000668	-----
5 / 1000	0.232698	0.766849	-----	-----	0.000271	0.000182	-----
6 / 1000	0.232200	0.766511	0.000002	-----	0.000359	0.000923	0.000005
7 / 1000	0.227262	0.762568	0.007643	0.000183	0.001472	0.000872	-----

TABLE 8.—PARTICLE SURFACE TEMPERATURE, VELOCITY, AND POROSITY FOR SURVIVING GRAPHITE PARTICLES AT THE EXIT OF THE ISOLATOR SECTION

Mach no./particle size	Surface temperature (K)	Velocity (m/s)	Porosity
5 / 10	625	1115	0.264
5 / 1000	1387	785	0.247
6 / 1000	1911	941	0.273
7 / 1000	2421	1156	0.294

Figure 85.—Example of ignition point for a H₂/vitiated air/particle mixture from the Mach 6 total temperature simulation with a 1 percent mass fraction of 1000 μm graphite particles.

The calculated ignition delay times for each condition with a 1 percent initial mass fraction of graphite particles, along with the ignition delay times for simulations done without any particles, are given in Table 9. In those cases where little graphite combustion occurred, only a slight reduction in ignition is observed, or even a slight increase in ignition delay (due to the heat-sink effect of the particles during the ignition delay calculation) for the Mach 5, 10 μm particle case. However, in the calculations where significant graphite combustion has occurred, the ignition delay time is greatly reduced from the cases with no particles. To examine this effect further, a second set of ignition delay calculations were performed to determine if the decrease in ignition delay time was due to vitiate species being present (including particles) or graphite combustion heat release. These calculations were performed at the elevated temperatures given in Table 6, but using no gas phase or particulate vitiates, only regular air. These results are given in Table 10. Comparing the results from Tables 9 and 10, it is evident that the majority of the graphite particle vitiation effect for these conditions is simply heat release. The presence of the vitiate species in the flow generally serves to slightly retard ignition. The relatively small impact of the combined vitiate species is consistent with other studies, such as Han, et al. (2004), where the significant effects of known ignition enhancing species such as NO are generally seen at lower temperatures and higher pressures than those studied here, and where the expected effects of a particular vitiate is frequently cancelled out by the effects of other vitiate species when they are studied in combination. The purpose of these ignition delay calculations is only to look at the combined effect of all the vitiates. Further studies of individual vitiate species effects would be needed to determine more detailed information, but such studies are not warranted here.

TABLE 9.—IGNITION DELAY TIME IN MICROSECONDS WITH VITIATES

Mach no.	No particles	10 μm	100 μm	1000 μm
5	1105	1112	367	1055
6	183	82.7	91.2	169
7	56.1	43.1	41.9	52.1

TABLE 10.—IGNITION DELAY TIME IN MICROSECONDS WITHOUT VITIATES

Mach no.	No particles	10 μm	100 μm	1000 μm
5	1105	1094	353	1055
6	183	75.8	84.4	169
7	56.0	39.1	37.8	51.7

7.0 Conclusions

In order to improve the understanding of particulate vitiation in hypersonic propulsion test facilities, a quasi-one dimensional numerical tool has been developed capable of efficiently modeling reacting particle-gas flows over a wide range of gas and particle conditions. Features of this code include finite rate kinetics for gas phase chemistry, a global porous-particle combustion model for the solid phase, mass, momentum and energy interactions between phases, subsonic and supersonic particle drag and heat transfer models, variable time step, and appropriate sets of subsonic and supersonic boundary conditions. The basic capabilities of this tool have been validated against available literature data or other validated codes.

This code has been demonstrated through a parametric study of particle vitiation effects in a model hypersonic propulsion test facility and scramjet. Parameters studied were simulated flight Mach number (Mach 5, 6, and 7), particle size (10, 100, and 1000 μm diameters), particle mass fraction (single particles and 0.01) and particle material (alumina and graphite). For the inert alumina particles, it was found that the presence of particles up to the 1 percent mass fraction had very little effect on the gas phase. As a 1 percent mass fraction would in reality be an extreme case, it is safe to conclude that hot wall ignition on the particle surface is likely to be the only potential inert particle vitiation effect, an effect that was

beyond the scope of this study. It was observed that only the 10 μm alumina particles tracked the gas flow reasonably well, and that when the particle size was increased to 1000 μm , the particle responded very little at all to changes in the gas flow, including shock waves, even though supersonic relative Mach numbers are observed. This is to be expected as the large particles have significant inertia against velocity changes, and have a relatively large volume-to-surface-area ratio that decreases heat transfer effects with the surroundings.

With the graphite particles, it was observed that the smallest particles in the study will either quickly quench, or quickly be consumed, depending on the gas and particle temperatures. The combustion of these 10 μm particles is solely determined by the particle temperature-dependent kinetic rates and not by oxygen diffusion. As the particle size increases, the particle is less likely to quench, because it has a larger thermal inertia, and so will remain at a high temperature long enough for the particle to ignite. As the particle and surrounding gas temperatures increase, the particle consumption rate increases somewhat, but not as fast as might be expected. This is due to diffusion rate limitations, both to the particle surface and internal to the particle. For the largest particles, combustion is significantly diffusion limited, so particle and gas temperature have little effect on the combustion rate. As the particle mass fraction is stepped up to 1 percent, the main change is the addition of significant heat release. As the choice of 1 percent mass fraction was meant to be a limiting case, the amount of heat release is extreme and not expected to be observed in real facilities. However, it does serve to increase the particle combustion rate, and to increase the quantity of NOx generated in the flow. In those cases where low reaction rates of graphite were observed for single particles, the increase to 1 percent mass fraction had very little impact, similar to the inert particles. Ignition delay time calculations for the 1 percent mass fraction of graphite particles cases showed significant decreases in ignition delay in the cases where higher graphite combustion rates, and therefore higher gas temperatures, were observed, but further calculations showed that this was due primarily to the increased combustor inlet temperature, not the vitiate species present in the flow. What chemical effects were present appeared to slightly increase the ignition delay. A review of several summary papers on gas-phase vitiate effects did little to clarify this result, as the findings are typically highly case-specific and not easily compared.

While the results discussed above are by no means conclusive regarding the potential effects of particle vitiation, they do provide significant insight into the physical effects of gas flow conditions on the particles, and of the particles on the gas flow. Understanding of the relative effects of the particle drag, the various forms of heat transfer, and combustion throughout the test facility and test engine is an important first step. The tool developed as part of this effort can be useful in determining the likely effects of specific particle contamination situations at specific test conditions, when the required modeling inputs are made available. This numerical tool is also generally useful for modeling any gas phase or gas-solid two-phase fluid flow problem that can be modeled as quasi-one dimensional.

8.0 Recommendations for Future Work

During the course of demonstrating the numerical tool developed for this study, a number of potential improvements were noted. These can be broadly categorized into three areas, as follows.

8.1 Modeling Improvements

1. Particle burnout model.—A particle burnout model should be added to the code if medium size particles are to be modeled. This is not important for very small particles which burn out quickly or for very large particles which suffer low mass loss.

2. Particle diameter shrinkage model.—This is another model that would be most critical for medium size particles. For smaller particles that burn out or quench quickly, the impact of incorrectly modeling the particle shrinkage is small, as there would not be expected to be a significant difference in the numerical solution at any significant distance downstream of the insertion point. For large particles, little

diameter change would be expected unless extremely long residence times were being considered. A particle diameter shrinkage model would need to be based on empirical data for the material, particle geometry, and test conditions under study.

3. Multiple simultaneous particle sizes.—The code currently only models a single particle size for a given run. The capability for handling multiple particle sizes simultaneously would enhance the ability of the code to model real situations.

4. Hot wall ignition model.—The ability to examine gaseous fuel-oxidizer ignition at the surface of an individual hot, reacting particle could be important. This type of modeling is most likely beyond the capability of a quasi-one dimensional code. A multi-dimensional code that addresses multi-species diffusion to and from the particle surface and particle surface chemistry would be needed to complement the current capability.

8.2 Input Data Improvements

1. Graphite Combustion Data.—For accurate results with reacting particles, it is necessary to have graphite combustion data, including combustion rate and particle shrinkage, across the full range of conditions to be experienced by the particles in the model. Such data could then be applied to the global reaction model in the code.

2. Good particle characterization.—For modeling a real system, it is necessary to have characterized the particle contamination in the facility. Particle size distribution and particle mass fraction must be known. Also the particles themselves need to be fully characterized in terms of overall porosity and internal pore size.

3. Validation Data.—It was not possible to validate the quasi-one dimensional code as a whole because of a lack of relevant validation data. Each capability within the code was validated separately, to the greatest extent possible. Gathering applicable validation data would greatly enhance confidence in the accuracy of the numerical results.

8.3 Additional Modeling

1. Lower Particle Mass Fractions for Reacting Particles.—The upper limit of 1 percent particle mass fraction used for this study was unrealistically high, although it does provide an upper bound. Cases could be run at various particle mass fractions below this level to understand the effect of particle vitiation at more realistic levels for those facility test conditions at which particle vitiation effects were observed.

2. Additional Particle Sizes for Reacting Particles.—In this demonstration study, different modes of behavior were observed at the different particle sizes. Running more studies in the intermediate size range would be of significant interest, since it is in this size range that the particle behavior is the least predictable.

Appendix A.—Symbols List

c_p	Gas phase mixture specific heat
$c_{p,i}$	Specific heat of gaseous species i
d_{pore}	Particle internal pore diameter
e_g	Gas phase specific internal energy
f_c	Effectiveness factor coefficient
g_f^o	Gas phase Gibbs energy of formation
$g_{f,i}^o$	Gibbs energy of formation of gaseous species i
h_g	Gas phase specific enthalpy
$h_{g,i}$	Specific enthalpy of gaseous species i
h_p	Particle convection coefficient
h_{to}	Gas phase enthalpy of formation
$h_{to,i}$	Enthalpy of formation of gaseous species i
k_b	Backward reaction rate
k_f	Forward reaction rate
k_g	Gas thermal conductivity
k_{1p}	1 st kinetic rate for carbon combustion
m_{obs}	Observed carbon combustion reaction order
n	Arrhenius reaction temperature exponent
ns	Number of chemical species
p	Pressure
q_{accum}	Heat accumulation within the particle outer shell
q_c	Gas phase conductive heat flux
q_{cond}	Conductive heat flow into the particle from the particle outer shell
q_{conv}	Convective heat flow out of the particle outer shell
q_{comb}	Combustion heat addition in particle outer shell
q_{rad}	Radiative heat flow out of the particle outer shell
q_w	Wall heat flux
r	Particle radial coordinate
r_e	Particle combustion rate based on particle outer shell energy balance
r_k	Mass-averaged particle combustion rate based on carbon kinetics
$r_{k,i}$	Local internal particle combustion rate based on carbon kinetics
r_{ox}	Particle combustion rate based on oxygen diffusion

r_p	Particle radius
r^\pm	Inner product used to calculate artificial viscosity
t	Time
u_g	Gas phase velocity
u_p	Particle velocity
x	Axial distance coordinate
x_p	Particle axial position
A	Cross sectional area
A_f	Arrhenius reaction pre-exponential factor
C	Artificial viscosity interim variable
C_D	Particle drag coefficient
C_s	Particle material heat capacity
D_e	Particle internal diffusion coefficient
D_i	Diffusion coefficient of gaseous species i
$D_{i,j}$	Binary diffusion coefficient between gaseous species i and j
D_K	Knudsen diffusion coefficient
$D_{O_2,M}$	Molecular diffusion coefficient of oxygen into gas mixture
E_a	Arrhenius reaction activation energy
F	Array of convective terms from the gas phase governing equations
F_p	Drag force on a particle
H_1	Scramjet inlet throat height
J	Array of source terms from the gas phase governing equations
K_D	Mass transfer coefficient
K_{eq}	Equilibrium constant
K_P	2 nd kinetic rate for carbon combustion
K_s	Particle thermal conductivity
K^\pm	Artificial viscosity interim variable
L_i	Scramjet inlet and isolator ramp lengths
M	Mixture average molecular weight
M_c	Carbon atomic mass
M_i	Species molecular weight
MR	Ratio of moles of CO to moles of CO ₂ produced in carbon combustion
M_{rel}	Mach number based on particle/gas relative velocity
MSR	Molecular speed ratio
M_T	Thiele modulus

N	Number of chemical reactions
Nu_d	Nusselt number based on particle diameter
$P_{\text{O}_2,\text{fs}}$	Free stream partial pressure of oxygen
$P_{\text{O}_2,s}$	Partial pressure of oxygen at the particle surface
Pr	Prandtl number
R	Mixture gas constant
Re_{rel}	Particle Reynolds number based on particle/gas relative velocity
R_u	Universal gas constant
S_e	Energy equation energy source term
S_{ext}	Particle external surface area
Sh	Sherwood number
S_i	Reactant or product species
S_{int}	Particle internal surface area
S_m	Continuity equation mass source term
$S_{m,i}$	Species continuity equation mass source term
S_p	Momentum equation momentum source term
S_{tot}	Particle total surface area
T_{film}	Particle film temperature
T_g	Gas temperature
$T_g^*_{i,j}$	Reduced gas temperature for collision between species i and j
T_{insert}	The temperature at which a particle is inserted into the flow stream
T_p	Particle surface temperature or bulk temperature for uniform temperature particles
$T_{p,i}$	Particle temperature at internal grid point i
T_{rec}	Convective recovery temperature
T_{wall}	Facility mixer/nozzle wall temperature
$T_{\varepsilon,i}$	Effective temperature of gaseous species i
$T_{\varepsilon,i,j}$	Average effective temperature between gaseous species i and j
$T^*_{2,2}$	Reduced temperature for mixture viscosity
U	Array of dependent variables from the gas phase governing equations
X_i	Mole fraction of gaseous species i
Y_i	Mass fraction of gaseous species i
α	Ratio of particle mass flow to gas mass flow
α_i	Scramjet inlet/isolator ramp lengths
β_i	Scramjet inlet/isolator shock angles

χ	Artificial viscosity
ε	Particle porosity
ε_{rad}	Particle emissivity
ϕ	Gas phase volume fraction
$\varphi_{i,j}$	Averaging variable for mixture viscosity
γ	Ratio of specific heats
η	Particle internal diffusion effectiveness factor
η_{avg}	Mass-averaged particle internal diffusion effectiveness factor
λ	Artificial viscosity velocity eigenvalue
μ	Gas phase viscosity
μ_i	Viscosity of gaseous species i
v_c	Courant number
v_i	Diffusion velocity of gaseous species i
v'_i	Stoichiometric coefficient of reactant species i
v''_i	Stoichiometric coefficient of product species i
v_o	Stoichiometric coefficient of oxygen consumed per mole of carbon consumed
θ	Artificial viscosity flux limiter
ρ_g	Gas phase density
ρ_s	Particle material density
σ_i	Effective collision diameter of gaseous species i
$\sigma_{i,j}$	Average effective collision diameter between species i and j
σ_{S-B}	Stefan-Boltzmann constant
ζ	Oxygen diffusion coefficient
Δt	Numerical time step
Δr	Particle internal grid size
$\Omega_{D,i,j}$	Collision integral between species i and j
$\Omega_{2,2}$	Collision integral for mixture viscosity
ξ	Intermediate variable for carbon combustion rate calculation
Ψ	Ratio of moles of CO ₂ to total moles produced in carbon combustion

Appendix B.—Gas Phase Kinetic Mechanism

The detailed gas phase kinetic mechanism used for this study is given in Table B.1. While the majority of the reactions follow the simple Arrhenius form, there are a number that have additional features. Ten of the reactions required the participation of a third body, for which the species third body efficiencies are included in Table B.2. Reactions 18, 19, 23, and 25 include a second duplicate reaction with different Arrhenius constants. The sum of the two reactions provides the correct temperature dependent behavior. Lastly, reactions 12, 14, and 24 are pressure dependent reactions. The first set of Arrhenius constants represents the high pressure limit, while the second set represents the low pressure limit. These two reaction rates are then combined via the Troe method, using the constants provided, for reactions 12 and 14, and via the Lindemann method for reaction 24. These methods are described in detail by Kee, et al (1993).

TABLE B.1.—GAS-PHASE KINETIC MECHANISM^c

Reaction ref. no.	Reaction	A_f	n	E_a	Reaction source ^a
1	$H + O_2 \rightleftharpoons O + OH$	2.644×10^{16}	-0.6707	17041	05Davis
2	$O + H_2 \rightleftharpoons H + OH$	4.589×10^4	2.70	6260	05Davis
3	$OH + H_2 \rightleftharpoons H + H_2O$	1.734×10^8	1.51	3430	05Davis
4	$2OH \rightleftharpoons O + H_2O$	3.973×10^4	2.40	-2110	05Davis
5	$H + H + M \rightleftharpoons H_2 + M$	1.78×10^{18}	-1.0	0.0	05Davis
6	$2H + H_2 \rightleftharpoons 2H_2$	9.0×10^{16}	-0.600	0.0	05Davis
7	$2H + H_2O \rightleftharpoons H_2 + H_2O$	5.624×10^{19}	-1.25	0.0	05Davis
8	$2H + CO_2 \rightleftharpoons H_2 + CO_2$	5.50×10^{20}	-2.0	0.0	05Davis
9	$H + OH + M \rightleftharpoons H_2O + M$	4.40×10^{22}	-2.0	0.0	05Davis
10	$O + H + M \rightleftharpoons OH + M$	9.428×10^{18}	-1.0	0.0	05Davis
11	$O + O + M \rightleftharpoons O_2 + M$	1.20×10^{17}	-1.0	0.0	05Davis
12	$H + O_2(+M) \rightleftharpoons HO_2(+M)$	5.116×10^{12}	0.44	0.0	05Davis
	Low	6.328×10^{19}	-1.4	0.0	
	TROE	0.5	1×10^{-30}	1×10^{30}	
13	$H_2 + O_2 \rightleftharpoons HO_2 + H$	5.916×10^5	2.433	53502	05Davis
14 ^b	$2OH(+M) \rightleftharpoons H_2O_2(+M)$	1.11×10^{14}	-0.37	0.0	05Davis
	Low	2.01×10^{17}	-0.584	-2293	
	TROE	0.0	345	10	
15	$HO_2 + H \rightleftharpoons O + H_2O$	3.97×10^{12}	0.0	671	05Davis
16	$HO_2 + H \rightleftharpoons 2OH$	7.485×10^{13}	0.0	295	05Davis
17	$HO_2 + O \rightleftharpoons OH + O_2$	4×10^{13}	0.0	0.0	05Davis
18a	$HO_2 + OH \rightleftharpoons O_2 + H_2O$	2.375×10^{13}	0.0	-500	05Davis
18b	$HO_2 + OH \rightleftharpoons O_2 + H_2O$	1×10^{16}	0.0	17330	05Davis
19a	$2HO_2 \rightleftharpoons O_2 + H_2O_2$	1.3×10^{11}	0.0	-1630	05Davis
19b	$2HO_2 \rightleftharpoons O_2 + H_2O_2$	3.658×10^{14}	0.0	12000	05Davis
20	$H_2O_2 + H \rightleftharpoons HO_2 + H_2$	6.05×10^6	2.0	5200	05Davis
21	$H_2O_2 + H \rightleftharpoons OH + H_2O$	2.41×10^{13}	0.0	3970	05Davis
22	$H_2O_2 + O \rightleftharpoons OH + HO_2$	9.63×10^6	2.0	3970	05Davis
23a	$H_2O_2 + OH \rightleftharpoons HO_2 + H_2O$	2×10^{12}	0.0	427	05Davis
23b	$H_2O_2 + OH \rightleftharpoons HO_2 + H_2O$	2.67×10^{41}	-7.0	37600	05Davis
24	$CO + O(+M) \rightleftharpoons CO_2(+M)$	1.362×10^{10}	0.0	2384	05Davis
	Low	1.173×10^{24}	-2.79	4191	
25a	$CO + OH \rightleftharpoons CO_2 + H$	8×10^{11}	0.14	7352	05Davis
25b	$CO + OH \rightleftharpoons CO_2 + H$	8.784×10^{10}	0.03	-16	05Davis

TABLE B.1.—GAS-PHASE KINETIC MECHANISM^c

Reaction ref. no.	Reaction	A_f	n	E_a	Reaction source ^a
26	$\text{CO} + \text{O}_2 \rightleftharpoons \text{CO}_2 + \text{O}$	1.119×10^{12}	0.0	47700	05Davis
27	$\text{CO} + \text{HO}_2 \rightleftharpoons \text{CO}_2 + \text{OH}$	3.01×10^{13}	0.0	23000	05Davis
28	$\text{HCO} + \text{H} \rightleftharpoons \text{CO} + \text{H}_2$	1.2×10^{14}	0.0	0.0	05Davis
29	$\text{HCO} + \text{O} \rightleftharpoons \text{CO} + \text{OH}$	3×10^{13}	0	0	05Davis
30	$\text{HCO} + \text{O} \rightleftharpoons \text{CO}_2 + \text{H}$	3×10^{13}	0	0	05Davis
31	$\text{HCO} + \text{OH} \rightleftharpoons \text{CO} + \text{H}_2\text{O}$	3.02×10^{13}	0	0	05Davis
32	$\text{HCO} + \text{M} \rightleftharpoons \text{CO} + \text{H} + \text{M}$	1.87×10^{17}	-1	17000	05Davis
33	$\text{HCO} + \text{H}_2\text{O} \rightleftharpoons \text{CO} + \text{H} + \text{H}_2\text{O}$	2.244×10^{18}	-1	17000	05Davis
34	$\text{HCO} + \text{O}_2 \rightleftharpoons \text{CO} + \text{HO}_2$	1.204×10^{10}	.807	-727	05Davis
35	$\text{N} + \text{NO} \rightleftharpoons \text{N}_2 + \text{O}$	2.7×10^{13}	0	355	GRI3.0
36	$\text{N} + \text{O}_2 \rightleftharpoons \text{NO} + \text{O}$	9×10^9	1	6500	GRI3.0
37	$\text{N} + \text{OH} \rightleftharpoons \text{NO} + \text{H}$	3.36×10^{13}	0	385	GRI3.0
38	$\text{HO}_2 + \text{NO} \rightleftharpoons \text{NO}_2 + \text{OH}$	2.11×10^{12}	0	-480	GRI3.0
39	$\text{NO} + \text{O} + \text{M} \rightleftharpoons \text{NO}_2 + \text{M}$	1.06×10^{20}	-1.4	0	GRI3.0
40	$\text{NO}_2 + \text{O} \rightleftharpoons \text{NO} + \text{O}_2$	3.9×10^{12}	0	-240	GRI3.0
41	$\text{NO}_2 + \text{H} \rightleftharpoons \text{NO} + \text{OH}$	1.32×10^{14}	0	360	GRI3.0
42	$\text{H} + \text{NO} + \text{M} \rightleftharpoons \text{HNO} + \text{M}$	4.48×10^{19}	-1.3	740	GRI3.0
43	$\text{HNO} + \text{O} \rightleftharpoons \text{NO} + \text{OH}$	2.5×10^{13}	0	0	GRI3.0
44	$\text{HNO} + \text{H} \rightleftharpoons \text{H}_2 + \text{NO}$	9×10^{11}	.7	660	GRI3.0
45	$\text{HNO} + \text{OH} \rightleftharpoons \text{NO} + \text{H}_2\text{O}$	1.3×10^7	1.9	-950	GRI3.0
46	$\text{HNO} + \text{O}_2 \rightleftharpoons \text{HO}_2 + \text{NO}$	1×10^{13}	0	13000	GRI3.0
47	$\text{N} + \text{CO}_2 \rightleftharpoons \text{NO} + \text{CO}$	3×10^{12}	0	11300	GRI3.0

^a05Davis refers to the mechanism developed by Davis, et al (2005), while GRI3.0 refers to the GRI 3.0 (2005) mechanism.^bFor this reaction, the optional fourth Troe constant is used with a value of 345.^cThe units for the pre-exponential factor A_f are $\text{Kg/m}^2\text{-s-atm}$, while the units for the activation energy E_a are cal/g-mole. The temperature exponent n is unit-less.

TABLE B.2.—THIRD BODY EFFICIENCIES

Species	React 5	React 9	React 10	React 11	React 12	React 14	React 24	React 32	React 39	React 42
H_2	0	2	2	2.4	.75	2	2	2	1	1
O_2	1	1	1	1	.85	1	1	1	1	1
H_2O	0	6.3	12	15.4	11.89	6	12	0	1	1
OH	1	1	1	1	1	1	1	1	1	1
H	1	1	1	1	1	1	1	1	1	1
O	1	1	1	1	1	1	1	1	1	1
HO_2	1	1	1	1	1	1	1	1	1	1
H_2O_2	1	1	1	1	1	1	1	1	1	1
N	1	1	1	1	1	1	1	1	1	1
NO	1	1	1	1	1	1	1	1	1	1
NO_2	1	1	1	1	1	1	1	1	1	1
HNO	1	1	1	1	1	1	1	1	1	1
CO_2	0	3.6	3.6	3.6	2.18	3.6	3.6	3.6	1	1
CO	1	1.75	1.75	1.75	1.09	1.75	1.75	1.75	1	1
HCO	1	1	1	1	1	1	1	1	1	1
Ar	.63	.38	.7	.83	.4	.7	.7	1	1	1
N_2	1	1	1	1	1	1	1	1	1	1

References

- Ames Research Staff "Equations, Tables, and Charts for Compressible Flow," NASA Report 1135, 1953.
- Anderson, Jr., J.D. *Computational Fluid Dynamics*, McGraw-Hill, Inc., New York, 1995.
- Baek, S.W. "The Ignition of Dust Particles Behind Moving Shock Waves," Ph.D. Dissertation, University of Michigan, Ann Arbor, MI, 1985.
- Bailey, A.B.; Hiatt, J. "Free-Flight Measurements of Sphere Drag at Subsonic, Transonic, Supersonic, and Hypersonic Speeds for Continuum, Transition, and Near-Free-Molecular Flow Conditions," AEDC -TR-70-291, March 1971.
- Blake, T.R. "Low Reynolds Number Combustion of a Spherical Carbon Particle," Combustion and Flame, Vol. 129, No. 1 / 2, pp. 87–111, April 2002.
- Carlson, D.J.; Hoglund, R.F. "Particle Drag and Heat Transfer in a Rocket Nozzle," AIAA Journal, Vol. 2, No. 11, pp. 1980–1984, November, 1964.
- Chang, I.S. "One- and Two-Phase Nozzle Flows," AIAA Journal, Vol. 18, No. 12, pp. 1455–1461; December 1980.
- Chase, M.W.; Davies, C.A.; Downey, J.R.; Frurip, D.J.; McDonald, R.A.; Syverud, A.N. *JANAF Thermochemical Tables, Third Edition*, American Institute of Physics, New York, 1986.
- Crowe, C.T. "Drag Coefficient of Particles in a Rocket Nozzle," AIAA Journal, Vol. 5, No. 5, pp. 1021–1022; May 1967.
- Davis, S.F. "A Simplified TVD Finite Difference Scheme Via Artificial Viscosity," SIAM Journal on Scientific and Statistical Computing, Vol. 8, No. 1, pp. 1–18, January 1987.
- Davis, S.G.; Joshi, A.V.; Wang, H.; Egolfopoulos, F. "An Optimized Kinetic Model of H₂/CO Combustion," Proceedings of the 30th International Symposium of The Combustion Institute, pp. 1283–92, Chicago, IL, July 2002.
- Di Giacinto, M.; Sabetta F.; Piva, R. "Two-way Coupling Effects in Dilute Gas-Particle Flows," Transactions of the ASME, Vol. 104, pp. 304–312, September 1982.
- Drake, R.M.; Backer, G.H. "Heat Transfer from Spheres to a Rarefied Gas in Supersonic Flow," Transactions of the ASME, Vol. 74, pp. 1241–1249; October 1952.
- Drummond, J.P. "Supersonic Reacting Internal Flow Fields," NASA TM-103480, 1990.
- Egolfopoulos, F.N.; Campbell, C.S. "Dynamics and Structure of Dusty Reacting Flows: Inert Particles in Strained, Laminar, Premixed Flames," Combustion and Flame, Vol. 117, No. 1 / 2, pp. 206–226, April 1999.
- Fox, T.W.; Rackett, C.W.; Nicholls, J.A. "Shock Wave Ignition of Magnesium Powders," Proceedings of the 11th International Symposium on Shock Tube and Shock Wave Research, pp. 262–268, Seattle, WA, July 1977.
- Froberg, R.W. "The Carbon-Oxygen Reaction: An Experimental study of the Oxidation of Suspended Carbon Spheres," Ph.D. Dissertation, The Pennsylvania State University, State College, PA, 1967.
- Fry, R.S. "Fundamentals of Test Medium Effects in Ground Testing for Scramjet-Powered Flight," CPIA CPTR 78, January 2004.
- Georgiadis, N.J. "A Hybrid Numerical Method for Turbulent Mixing Layers," NASA/TM—2001-210811, May 2001.
- Gordon S.; McBride, B.J. "Computer Program for Calculation of Complex Chemical Equilibrium Compositions and Applications," NASA Reference Publication 1311, 1994.
- GrafTech International, Ltd., "Technical Data Sheet 43: Grade PGX Molded Graphite," www.graftech.com, 2005.
- Han, B.; Sung, C.J.; Nishioka, M. "Effects of Vitiated Air on Hydrogen Ignition in a High-Speed Laminar Mixing Layer," Combustion Science and Technology, Vol. 176, No. 3, pp. 305–330, March 2004.
- Heiser, W.H.; Pratt, D.T. *Hypersonic Airbreathing Propulsion*, AIAA, Washington D.C., 1994.
- Henderson, C.B. "Drag Coefficients of Spheres in Continuum and Rarefied Flows," AIAA Journal, Vol. 14, No. 6, pp. 707–708; June 1976.

- Hirschfelder, J.O.; Curtiss, C.F.; Bird R.B. *Molecular Theory of Gases and Liquids*, John Wiley & Sons, New York, 1964.
- Hong, J. "Modeling Char Oxidation as a Function of Pressure using an Intrinsic Langmuir Rate Equation," Ph.D. Dissertation, Brigham Young University, Salt Lake City, UT, 2000.
- Hurt, R.; Sun, J-K; Lunden, M. "A Kinetic Model of Carbon Burnout in Pulverized Coal Combustion," *Combustion and Flame*, Vol. 113, No. 1/2, pp. 181–197, April 1998.
- Hurt, R.H.; Mitchell, R.E. "Unified High Temperature Char Combustion Kinetics for a Suite of Coals of Various Rank," Proceedings of the 24th International Symposium of The Combustion Institute, pp. 1243–1250, Sydney, Australia, July 1992.
- Igra, O; Takayama, K. "Shock Tube Study of the Drag Coefficient of a Sphere in a Nonstationary Flow," *Proceedings of the Royal Society-Series A*, Vol. 442, No. 1915, pp. 1243–1250, August 1993.
- Incropera, F.P.; DeWitt, D.P. *Fundamentals of Heat and Mass Transfer*, John Wiley & Sons, New York, 2002.
- Ishii, R.; Umeda, Y.; Kawasaki, K. "Nozzle Flow of Gas-Particle Mixtures," *Physics of Fluids*, Vol. 30, No. 3, pp. 752–760; March 1987.
- Kee, R.J.; Rupley, F.M.; Miller, J.A. "Chemkin-II: A Fortran Chemical Kinetics Package for the Analysis of Gas Phase Chemical Kinetics," Sandia Report SAND89–8009B, September 1993.
- Kuo, K.K. *Principles of Combustion*, John Wiley & Sons, New York, 1986.
- Lee, J.C.; Yetter, R.A.; Dryer, F.L. "Transient Numerical Modeling of Carbon Particle Ignition and Oxidation," *Combustion and Flame*, Vol. 101, No. 4, pp. 387–398, June 1995.
- Libby, P.A. "Ignition, Combustion, and Extinction of Carbon Particles," *Combustion and Flame*, Vol. 38, No. 3, pp. 285–300, August 1980.
- Ludwig, T.; Roth, P. "Modeling of Laminar Combustion Wave Propagation in Reactive Gas/Particle Mixtures," *International Journal of Multiphase Flow*, Vol. 23, No. 1, pp. 93–111, February 1997.
- Makino, A.; Law, C.K. "Quasi-Steady and Transient Combustion of a Carbon Particle: Theory and Experimental Comparisons," *Proceedings of the 21st Symposium of the Combustion Institute*, Munich, West Germany pp. 183–191, August 1986.
- Maxwell, B.R.; Seasholtz, R.G. "Velocity Lag of Solid Particles in Oscillating Gases and in Gases Passing Through Normal Shock Waves," NASA Technical Note D-7490, March 1974.
- Mitani, T. "Ignition Problems in Scramjet Testing," *Combustion and Flame*, Vol. 101, No. 3, pp. 347–359, May 1995.
- Moors, J.H.J. "Pulverized Char Combustion and Gasification at High Temperatures and Pressures," Ph.D. Dissertation, Technische Universiteit Eindhoven, Eindhoven, Netherlands, 1998.
- Munro, R.G. "Evaluated Material Properties for a Sintered Alpha-Alumina," *Journal of the American Ceramic Society*, Vol. 80, No. 8, pp. 1919–1928, August 1997.
- Okada, J.; Ikegawa, T. "Combustion Rate of Artificial Graphites from 700 °C to 2000 °C in Air," *Journal of Applied Physics*, Vol. 24, No. 9, pp. 1149–1150, September 1953.
- Paxson, D.E. "A Comparison Between Numerically Modeled and Experimentally Measured Loss Mechanisms in Wave Rotors," AIAA Paper 93–2522, June 1993.
- Pellett, G.L.; Bruno, C.; Chinitz, W. "Review of Air Vitiation Effects on Scramjet Ignition and Flameholding Combustion Processes," AIAA Paper 2002–3880, July 2002.
- Perkins, H.D.; Thomas, S.R.; DeBonis, J.R. "Rocket-Based Combined Cycle Propulsion System Testing," *Journal of Propulsion and Power*, Vol. 14, No. 6, pp. 1065–1076, November 1998.
- Pierson, H.O. *Handbook of Carbon, Graphite, Diamond, and Fullerenes*, Noyes Publications, Park Ridge, NJ, 1993.
- Pluchino, A.B.; Masturzo, D.E. "Emissivity of Al₂O₃ Particles in a Rocket Plume," *AIAA Journal*, Vol. 19, No. 9, pp. 1234–1237, September 1981.
- Poinsot, T. J.; Lele, S. K. "Boundary Conditions for Direct Simulations of Compressible Viscous Flows," *Journal of Computational Physics*, Vol. 101, No. 1, pp. 104–129, July 1992.
- Powell, E.S.; Stallings, D.W. "A Review of Test Medium Contamination Effects on Test Article Combustion Processes," AIAA Paper 98–0551, January 1998.

- Ranish, J.M.; Walker, P.L. "High Pressure Studies of the Carbon-Oxygen Reaction," *Carbon*, Vol. 31, No. 1, pp. 135–141, 1993.
- Roffe, G.; Bakos, R.; Erdos, J. "The Propulsion Test Complex at GASL," ISABE Paper 97–7096, September 1997.
- Saad, M.A. *Compressible Fluid Flow*, Prentice-Hall, Englewood Cliffs, NJ, 1985.
- Shepherd, J.E. "Chemical Kinetics of Hydrogen-Air-Diluent Detonation," in *Progress in Astronautics and Aeronautics*, Vol. 106, p. 263–293, AIAA, New York, 1986.
- Sichel, M.; Baek, S.W.; Kauffman, C.W.; Maker, B.; Nicholls, J.A. "The Shock Wave Ignition of Dusts," *AIAA Journal*, Vol. 23, No. 9, pp. 1374–1380, September 1985.
- Slack, M.; Grillo, A. "Investigation of Hydrogen-Air Ignition Sensitized by Nitric Oxide and by Nitrogen Dioxide," NASA CR-2896, October 1977.
- Smith, G.P.; Golden, D.M.; Frenklach, M.; Moriarty, N.W.; Eiteneer, M.G.; Bowman, C.T.; Hanson, R.K.; Song, S.; Gardiner, W.C.; Lissianski, V.V.; Qin, Z. "GRI-Mech 3.0," http://www.me.berkeley.edu/gri_mech/, March 2006.
- Smith, J.M. *Chemical Engineering Kinetics*, McGraw-Hill, New York, 1981.
- Svehla, R.A. "Estimated Viscosities and Thermal Conductivities of Gases at High Temperatures," NASA TR R-132, 1962.
- Tannehill, J.C.; Anderson, D.A.; Pletcher, R.H. *Computational Fluid Mechanics and Heat Transfer, 2nd Edition*, Taylor & Francis, Washington D.C., 1997.
- Tu, C.M.; Davis, H.; Hottel, H.C. "Combustion Rate of Carbon: Combustion of Spheres in Flowing Gas Streams," *Industrial and Engineering Chemistry*, Vol. 26, No. 7, pp. 749–757, July 1934.
- Warnatz, J.; Maas, U.; Dibble, R.W. *Combustion*, Springer-Verlag, Berlin, 1999.
- Weber, J., Editor, "Scramjet Propulsion Testing Recommended Practices and Guidelines," CPIA Publication 710, March 2002.
- White, F.M. *Viscous Fluid Flow*, McGraw-Hill, New York, 1991.
- White, F.M. *Heat and Mass Transfer*, Addison-Wesley, Reading, MA, 1988.
- Zhou, H.; Flamant, G.; Gauthier, D.; Lu, J. "Lagrangian Approach for Simulating the Gas-Particle Flow Structure in a Circulating Fluidized Bed Riser," *International Journal of Multiphase Flow*, Vol. 28, No. 11, pp. 1801–1821, November 2002.

REPORT DOCUMENTATION PAGE				Form Approved OMB No. 0704-0188
<p>The public reporting burden for this collection of information is estimated to average 1 hour per response, including the time for reviewing instructions, searching existing data sources, gathering and maintaining the data needed, and completing and reviewing the collection of information. Send comments regarding this burden estimate or any other aspect of this collection of information, including suggestions for reducing this burden, to Department of Defense, Washington Headquarters Services, Directorate for Information Operations and Reports (0704-0188), 1215 Jefferson Davis Highway, Suite 1204, Arlington, VA 22202-4302. Respondents should be aware that notwithstanding any other provision of law, no person shall be subject to any penalty for failing to comply with a collection of information if it does not display a currently valid OMB control number.</p> <p>PLEASE DO NOT RETURN YOUR FORM TO THE ABOVE ADDRESS.</p>				
1. REPORT DATE (DD-MM-YYYY) 01-10-2010		2. REPORT TYPE Technical Memorandum		3. DATES COVERED (From - To)
4. TITLE AND SUBTITLE Development and Demonstration of a Computational Tool for the Analysis of Particle Vitiation Effects in Hypersonic Propulsion Test Facilities				5a. CONTRACT NUMBER
				5b. GRANT NUMBER
				5c. PROGRAM ELEMENT NUMBER
6. AUTHOR(S) Perkins, Hugh, Douglas				5d. PROJECT NUMBER
				5e. TASK NUMBER
				5f. WORK UNIT NUMBER WBS 599489.02.07.03.03.03.03
7. PERFORMING ORGANIZATION NAME(S) AND ADDRESS(ES) National Aeronautics and Space Administration John H. Glenn Research Center at Lewis Field Cleveland, Ohio 44135-3191				8. PERFORMING ORGANIZATION REPORT NUMBER E-17390
9. SPONSORING/MONITORING AGENCY NAME(S) AND ADDRESS(ES) National Aeronautics and Space Administration Washington, DC 20546-0001				10. SPONSORING/MONITOR'S ACRONYM(S) NASA
				11. SPONSORING/MONITORING REPORT NUMBER NASA/TM-2010-216765
12. DISTRIBUTION/AVAILABILITY STATEMENT Unclassified-Unlimited Subject Categories: 09, 34, and 07 Available electronically at http://gltrs.grc.nasa.gov This publication is available from the NASA Center for AeroSpace Information, 443-757-5802				
13. SUPPLEMENTARY NOTES				
14. ABSTRACT In order to improve the understanding of particle vitiation effects in hypersonic propulsion test facilities, a quasi-one dimensional numerical tool was developed to efficiently model reacting particle-gas flows over a wide range of conditions. Features of this code include gas-phase finite-rate kinetics, a global porous-particle combustion model, mass, momentum and energy interactions between phases, and subsonic and supersonic particle drag and heat transfer models. The basic capabilities of this tool were validated against available data or other validated codes. To demonstrate the capabilities of the code a series of computations were performed for a model hypersonic propulsion test facility and scramjet. Parameters studied were simulated flight Mach number, particle size, particle mass fraction and particle material.				
15. SUBJECT TERMS Combustion; Particulates; Hypersonic wind tunnels; Supersonic combustion ramjet				
16. SECURITY CLASSIFICATION OF:		17. LIMITATION OF ABSTRACT UU	18. NUMBER OF PAGES 102	19a. NAME OF RESPONSIBLE PERSON STI Help Desk (email:help@sti.nasa.gov)
a. REPORT U	b. ABSTRACT U			c. THIS PAGE U

Standard Form 298 (Rev. 8-98)
Prescribed by ANSI Std. Z39-18

